A novel Apparatus for Quantum Gas Microscopy of Lithium Atoms

DISSERTATION

zur Erlangung des Doktorgrades
an der Fakultät für Mathematik, Informatik und Naturwissenschaften
im Fachbereich Physik
der Universität Hamburg

vorgelegt von

Andreas KERKMANN

geboren in

Hilden

Hamburg

2019

Gutachter

Gutachter der Dissertation:	Prof. Dr. Klaus Sengstock Prof. Dr. Henning Moritz
Gutachter der Disputation:	Prof. Dr. Klaus Sengstock Prof. Dr. Henning Moritz Prof. Dr. Roman Schnabel Prof. Dr. Ludwig Mathey Prof. Dr. Andreas Hemmerich
Vorsitzender der Prüfungskommission:	Prof. Dr. Roman Schnabel
Datum der Disputation:	03.12.2019
Vorsitzender des Promotionsausschusses:	Prof. Dr. Günter Hans Walter Sigl
Leiter des Fachbereichs Physik:	Prof. Dr. Wolfgang Hansen
Dekan der Fakultät für Mathematik, Informatik und Naturwissenschaften:	Prof. Dr. Heinrich Graener

Abstract

The behavior of quantum many-body systems in nature is often an issue of great complexity. Hence, instead of describing those systems entirely, we tend to extract particular phenomena of interest and to simulate them in accessible simplified quantum mechanical model systems.
Fortunately, the total availability of such model systems is not only restricted to numerical models but there are many artificially prepared quantum systems. In the field of ultracold quantum gases, experimentalists provide powerful tools for preparing, manipulating and detecting quantum many-body systems.
A new scientific project in the group of Klaus Sengstock is setting up a modern and versatile ultracold quantum gas experiment. It aims to prepare model systems for simulating effects that play a role in attosecond science as well as to engineer quantum states with anyonic excitation that are e.g. relevant in studies of the fractional quantum Hall effect.
Within the course of this first PhD thesis of the project, we built a novel apparatus that is explicitly geared to allow quantum gas microscopy in the future as it will be a powerful tool to analyze interesting correlations on a single particle level.
Our built apparatus includes a 2D-/3D-MOT loading scheme that we verify to work for both stable isotopes of lithium. Due to this unconventional but compact way of loading the atoms from a hot gas streaming out of an oven, we are able to omit any transfer of the atoms after the trapping in a 3D-MOT. Thus, the 3D-MOT is already situated in a relatively small glass cell at the focus of an objective providing sub-micron resolution that we characterize numerically and in a test setup to suit for quantum gas microscopy.
As further manipulation steps, we implement gray molasses cooling that cools the gas to sub-Doppler temperatures. It permits the loading of a far-detuned optical dipole trap where we routinely perform all-optical evaporative cooling and reach quantum degeneracy by realizing a Bose-Einstein condensate of weakly-bound ^{6}Li molecules.
As we require two-dimensional samples for our studies, we additionally implement a red-detuned one-dimensional optical accordion for the dynamical and preferably adiabatic squeezing of our gas within a single slice of that vertical lattice.
In order to image the atoms in that slice with single-particle resolution on a sub-micron level, we not only rely on an objective with high numerical aperture but also on an additional optical lattice for pinning the atoms within the two-dimensional plane during the emission of fluorescence photons. Here, we decided for a horizontal triangular lattice that is designed, characterized and adjusted onto the atomic sample during the present thesis.

Zusammenfassung

Das Verhalten von Quantenvielteilchensystemen in der Natur ist oftmals sehr komplex. Anstatt diese Systeme vollständig zu beschreiben, versuchen wir daher interessante Phänomene zu extrahieren und sie in zugänglichen, vereinfachten quantenmechanischen Modellsystemen zu simulieren.
Glücklicherweise beschränkt sich die Verfügbarkeit solcher Modellsysteme nicht nur auf numerische Rechenmodelle, sondern es gibt viele künstlich herstellbare Quantensysteme. Auf dem Gebiet der ultrakalten Quantengase haben Experimentatoren leistungsstarke Werkzeuge zur Herstellung, Manipulation und Detektion von künstlichen Quantenvielteilchensystemen zur Hand.
In einem neuen Projekt wird in der Forschungsgruppe von Klaus Sengstock ein modernes und vielseitiges Experiment mit ultrakalten Quantengasen aufgebaut, das darauf abzielt, eine neue Sicht auf quantenmechanische Modelle zu richten, die in der Ultrakurzzeitphysik eine Rolle spielen, und ferner auch Quantenzustände mit anyonischen Anregungen zu präparieren, die beispielsweise in Studien zum fraktionierten Quanten-Hall-Effekt relevant sind.
Im Rahmen dieser ersten Doktorarbeit an dem Projekt haben wir eine neuartige Maschine gebaut, die speziell darauf ausgerichtet ist zukünftig Quantengasmikroskopie an Modellsystemen zu ermöglichen. Diese Technik zur Detektion wird für uns ein leistungsfähiges Werkzeug sein, mit dem interessante Korrelationen auf der Basis einzelner Konsituenten des Quantensystems analysiert werden können.
Die gebaute Maschine enthält ein 2D-/3D-MOT-Ladeschema, das für die beiden stabilen Lithiumisotope funktioniert. Hierbei werden die Atome aus einem heißen Gas, das aus einem Ofen strömt, über eine 2D-MOT in eine 3D-MOT geladen. Diese Methode macht es möglich, einen weiteren Transport der Atome nach dem Einfangen in einer 3D-MOT zu vermeiden. So befindet sich letztere bereits in einer relativ kleinen Glaszelle im Fokus eines Objektivs, das eine Submikrometer-Auflösung ermöglicht. Diese charakterisierten wir numerisch und in einem dafür geeigneten Versuchsaufbau hinsichtlich der Tauglichkeit zur Quantengasmikroskopie.
Nach der MOT führen wir in einem weiteren Manipulationsschritt eine Graue-Melasse-Kühlung durch, die das Gas auf Sub-Doppler-Temperaturen bringt. Dabei erhöht sich die Phasenraumdichte, sodass das Laden einer weit verstimmten optischen Dipolfalle möglich ist. Hier führen wir routinemäßig eine rein optische Verdampfungskühlung durch und erreichen Quantenentartung, indem wir ein Bose-Einstein-Kondensat aus ^{6}Li Molekülen realisieren.
Da wir ein zweidimensionales Gas für unsere Studien benötigen, implementieren wir ein rot-verstimmtes eindimensionales optisches Akkordeon, mit dem Ziel unser Gas innerhalb einer einzelnen Schicht dieses vertikalen Gitters dynamisch und dennoch möglichst adiabatisch zu komprimieren.
Um die Atome in dieser Schicht mit Einzelteilchenauflösung im Submikrometerbereich abzubilden, setzen wir nicht nur auf ein Objektiv mit hoher numerischer Apertur, sondern auch auf ein zusätzliches optisches Gitter, das die Atome in der zweidimensionalen Ebene während der Emission von Fluoreszenzphotonen festhält. Hier haben wir uns für ein horizontales Dreiecksgitter entschieden, das in der vorliegenden Arbeit entworfen, charakterisiert und auf die Atome justiert wurde.

Contents

Chapter 1

Introduction

... it's a wonderful problem because it doesn't look so easy.
– R. Feynman [1]

The availability of digital computers and their exponentially increasing growth of power since the late 1950s [2], led to numerical solutions of more and more sophisticated tasks that are e.g. investigated in the field of computational physics [3]. Investigating quantum mechanics however turns out to be challenging for digital computers, since the dimensionality of a quantum system grows exponentially with the number of constituents.
For this reason people formulated the idea of making use of quantum mechanics to gain more inside into its own beauty [1, 4]. We can interpret this idea in two ways[1]:

- Quantum computation: We may think about building another type of computer that behaves quantum mechanically and solves a larger class of computational problems with algorithms like e.g. the Deutsch-Josza algorithm [7], the Grover algorithm [8] or the Shor algorithm [9].
- Quantum simulation: We may think about preparing artificial but well controlled quantum systems to address questions that arise from a theoretical thesis or from an observation of a more complex system that exists in nature but is hardly accessible.

Ultracold quantum gases for quantum simulation

In the field of ultracold quantum gases, people realize artificial states of matter by cooling and trapping dilute atomic gases. Since they can be cooled to a temperature of a few nanokelvin the atoms reveal their quantum behavior in the gas and become a quantum degenerate system that has been realized since 1995 [10–12]. From then on and already before, many physicists have contributed with unresting creativity and lots of efforts to a great multi-purpose-toolkit for controlling and tuning those state-of-the-art systems. Within the last decades, they have started to engineer many fundamentally and technologically interesting quantum states as it is reviewed e.g. in [13–17].

[1] In a deeper look both ways have a certain intellectual and technological overlap and should not be seen as completely separate. The overlap also causes the terminology of analog quantum computation for quantum simulation because of its continuous evolution rather than gating qubits [5, 6].

Detection method – quantum gas microscopy

A very powerful tool to detect the microscopic correlations of artificial quantum systems is a "quantum gas microscope". It has been realized since 2009 for bosonic rubidium [18, 19] and since 2015 for fermionic lithium [20, 21], fermionic potassium [22–24] and bosonic ytterbium [25, 26].
In the last decade, quantum gas microscopes mostly concentrated on many-body phenomena where the periodicity of a lattice is included in the quantum system under simulation. The most treated systems are described by Hubbard Hamiltonians for bosons or fermions [27, 28]. To name only some achievements with quantum gas microscopes, people investigated microscopically the superfluid to Mott insulator transition for bosons [19, 29, 30] as well as the metal to band insulator to Mott insulator transition for fermions [21, 31, 32], spin correlations and phenomena of quantum magnetism [33–47] and moreover many further quantum dynamical properties [48–60].

And this thesis...

During the course of this PhD thesis, we constructed a new experimental apparatus for cooling and trapping lithium atoms. Even though this thesis mainly concentrates on the fermionic isotope ^{6}Li, the experimental setup is explicitly constructed in a way that allows easy switching to the stable bosonic isotope ^{7}Li. Per se, this alkali metal is a prominent choice in the community with well-known properties and well-explored cooling strategies. Moreover, both stable isotopes are often advantageous regarding their light mass in terms of large kinetic engery scales and their tunable interactions in terms of Feshbach resonances [61, 62].
Essentially, the novel machine is precisely geared to examine the trapped atoms as a quantum gas microscope. Compared to the already existing microscopes for fermionic lithium [20, 21, 63], we will be initially interested in smaller quantum ensembles as further discussed in the outlook of this thesis (see Chapter 7).

Synopsis

The following chapters of this thesis:

- **Chapter 2** gives an overview on the design and the construction of a compact experimental apparatus for quantum gas microscopy that avoids any transport after trapping the atoms in a 3D-MOT inside a small glass cell.
- **Chapter 3** introduces the molasses laser system and shows data from the unconventional 2D-/3D-MOT trapping technique for lithium atoms that we successfully implemented for ^{6}Li and ^{7}Li. Moreover, it presents gray molasses cooling as a sub-Doppler cooling mechanism for lithium atoms that enhances phase space density for a better loading into an all-optical far-detuned dipole trap.
- **Chapter 4** traces our road to a quantum degenerate Bose-Einstein condensate of molecules by implementing forced evaporation of a ^{6}Li gas with strong repulsive scattering length via depth reduction of the all-optical trap by motorized waveplate rotation.
- **Chapter 5** introduces our optical lattice configuration for spatial pinning of the atoms. First, it reports on a vertical one-dimensional optical accordion where

we can load a gas completely into a single slice and are able to tune dynamically the trap frequency along the lattice direction via a reduction of the lattice constant. Second, it informs about a horizontal two-dimensional triangular lattice that is aligned onto the atoms. Here, we especially measured the phase noise between the lattice beams as it is one crucial point for a quantum gas microscope.

- **Chapter 6** shows the alignment optomechanics design for the the high-NA objective and demonstrates its suitability for quantum gas microscopy. We further explain how we perform a 3D-MOT at the focus position of that objective. Moreover, the chapter contains a short recap on the usage of an offset lock for hitting a transition frequency for lithium in high magnetic fields and an overview on the auxiliary absorption imaging axes of the experiment.

- **Chapter 7** concludes with a summary about the studies and efforts during this PhD thesis and outlines future technical goals as well as future research topics that will be investigated based on the work of this thesis.

Chapter 2

Construction of the experimental apparatus

The design and the construction of the experimental apparatus is the starting point for every novel quantum gas machine. This chapter gives an overview on the design and the construction of a compact experimental apparatus for quantum gas microscopy that avoids any transport after trapping the atoms in a 3D-MOT inside a small glass cell.
Basic design decisions had been made before the author started his PhD. He elaborated further details and managed the construction together Michael Hagemann and B. S. Rem.

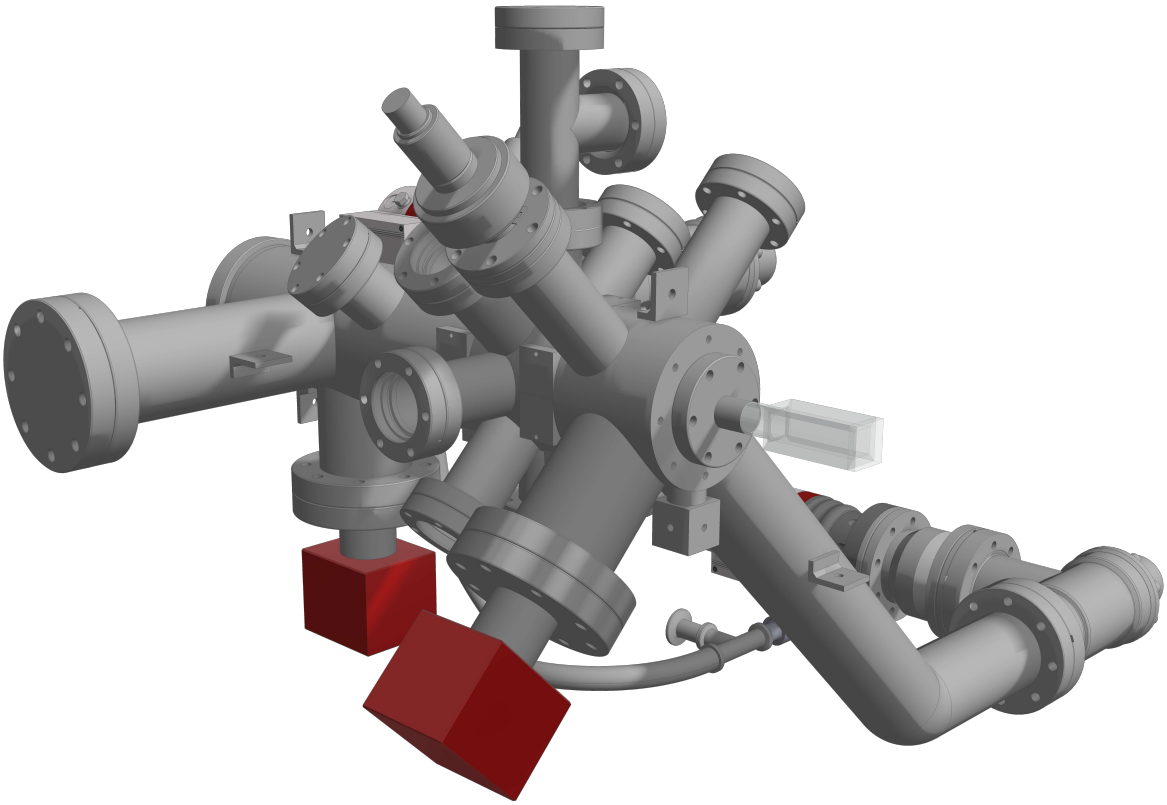

FIGURE 2.1: View on the vacuum chamber – The glass cell is flanged in front onto the steel chamber.

2.1 Motivation of the design

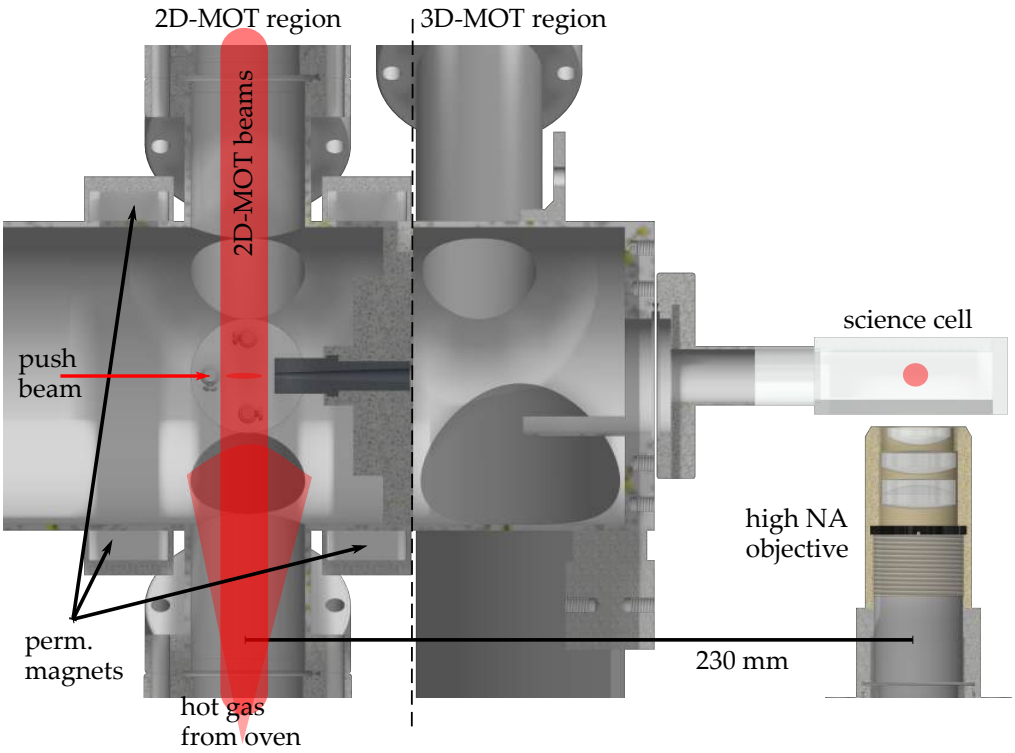

FIGURE 2.2: Vertical cut along the push beam axis through some of the main parts of the experiment – A hot gas of lithium atoms (red cone) exits from an effusive oven into the cross section of two retro-reflected 2D-MOT beams. A red-detuned push beam supports the loading of radially slowed atoms through a differential pumping tube into a 3D-MOT sitting above the high resolution objective.

For the purpose of quantum simulation we need a high repetition rate in our experiments such that statistics become significant. Therefore, we realize a compact setup for a quantum gas microscope with a short experimental cycle time.
In order to keep our setup as compact as possible, the designed vacuum chamber (see Figure 2.1, 2.2 and detailed in [64]) allows us to omit any transfer stage. Thus, we perform a 3D-MOT in a glass cell (science cell) that is already at the position of our high resolution imaging system (see Chapter 6.1).
Since lithium sticks irreversibly on glass surfaces [65], we need to protect the science cell from a macroscopic contamination with lithium when loading the 3D-MOT. Furthermore, for a high readout fidelity in a quantum gas microscope we need to keep the background vacuum pressure in the science cell as low as possible.
We therefore load the 3D-MOT through a differential pumping tube via a 2D-MOT in the style of [66]. This technique of precooling lithium atoms in two dimensions allows to place the axis of an effusive oven perpendicular to the loading axis of the 3D-MOT (see Figure 2.2). If then the 2D-MOT laser beams as well as the push beam are switched off, no atoms will directly travel through the differential pumping tube. The tube itself has a length of 45.5 mm and a conical hole. It has a radius of 1.0 mm at the 2D-MOT side and 2.5 mm on the science cell side. The material is graphite that especially getters alkaline metals [67]. In the ultra high vacuum regime the tube helps to keep the pressure in the science cell at 10^{-11} mbar even if the pressure on the 2D-MOT side is at 10^{-9} mbar.

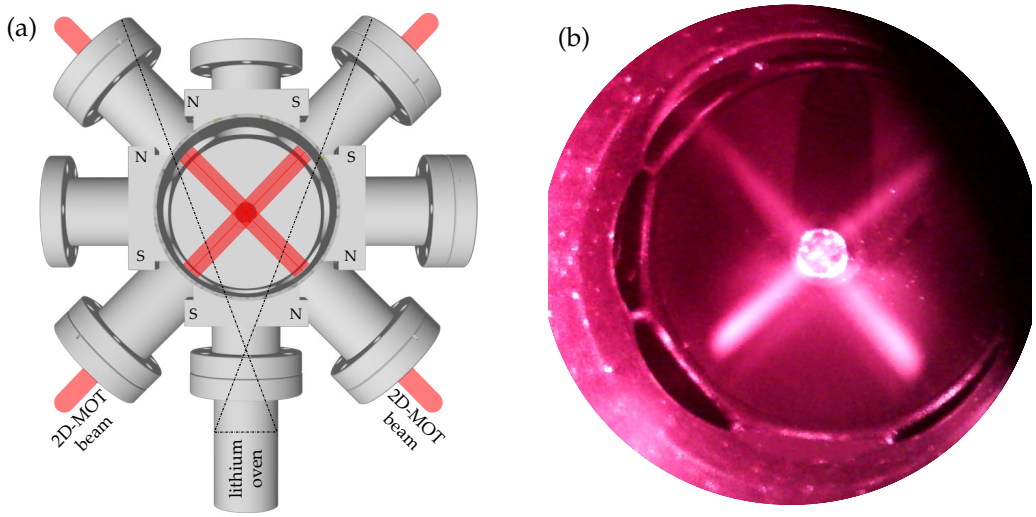

FIGURE 2.3: 2D-MOT view from the backside of the chamber – (a) A CAD drawing shows the 8-way cross including the entrance of the 2D-MOT beams, the orientation of the permanent magnets and the lithium oven that is flanged from below on the steel chamber. A dotted black line indicates the the maximum reasonable filling limit of the oven considering the contamination with lithium at the upper 2D-MOT view ports. (b) A camera allows the view on the fluorescence of hot lithium gas inside the 2D-MOT beams. The higher density in the gas near the oven gives a higher fluorescence signal below the 2D-MOT.

2.2 2D-MOT chamber

Since the loading rate of a 2D-MOT is inversely proportional to its distance to the 3D-MOT position we designed the distance as short as possible that is in our case $\sim$ 230 mm [64] (see Figure 2.2). The main part of the chamber itself is a radial DN CF 40 8-way cross with a DN CF 100 body along the loading axis (see Figure 2.3a). The retroreflected 2D-MOT beams are shone in through view ports being at $\pm 45^\circ$ to the vertical axis. The beams are shaped elliptically (see Table 3.2 and [68]) with the semi-major axis being adjusted along the loading axis. At this axis, the push beam enhances the number of atoms moving towards the 3D-MOT. The beam is propagating horizontally from the center of a DN CF 100 view port through the differential pumping tube.
A compact solution for reaching the required magnetic field gradient of $\sim 50\,\mathrm{G/cm}$ that points along the 2D-MOT beam axes is a double quadrupole field that is realized by bolting stacks of permanent magnets[1] on the vacuum chamber [69].

2.2.1 Lithium oven

The effusive oven providing a flux of gaseous hot lithium atoms is flanged from the bottom to the 8-way cross. In our case the oven design is a fairly simple cup with a length of 83 mm from its flange and a diameter of 40 mm. The design idea of the oven is to have a large area of emittance A_e in order to get a higher total flux Φ_{tot} of atoms at a constant temperature T as one finds from the HERTZ-KNUDSEN equation [70]

[1] Eclipse Magnetics Ltd: N750-RB, max. temperature 100 °C

$$\Phi_{\text{tot}} \propto A_e \frac{p_{\text{vap}}}{\sqrt{2\pi m k_B T}}, \tag{2.1}$$

with p_{vap} being the vapor pressure.
However, the choice of temperature is very important for the atomic flux. Like a derivation from [71] reveals the flux $\phi_c = \phi_{\text{tot}}(v < v_c)$ of trappable atoms having a velocity v that is below the capture velocity of the 2D-MOT v_c shows the following relation

$$\Phi_c \propto A_e \, v_c^4 \, T^{-2.5} \exp(-T_L/T). \tag{2.2}$$

Here, the exponential part of the temperature dependence is coming from the vapor pressure. For the case of lithium $p_{\text{vap}} \propto \exp(-T_L/T)$ with $T_L = 18\,474\,\text{K}$ being the latent heat temperature for vaporization [72]. Thus, we find that around 400 °C the flux doubles every $\sim 20\,^\circ\text{C}$.
In our setup, we measure the temperature at the oven with two thermistors[2] and a data logger[3] for the readout. The heat is applied via heating wires[4] that are doubly isolated with glass wool[5]. One heating wire heats the region directly below the flange, the other one heats the lower part of the cup. They are supplied by a stable but tunable power supply[6].
The performance of the 2D-MOT is monitored indirectly by the fluorescence from the 3D-MOT during loading (see Figure 3.3), but also by a camera[7] that images the fluorescence of the atoms inside the 2D-MOT beams (see Figure 2.3b). The oven temperature that allows a sufficient 3D-MOT loading rate for many hours per day depends on the actual status of the oven. Due to heat transfer to e.g. the permanent magnets, a reasonable maximum temperature of the oven is $\sim 470\,^\circ\text{C}$. At the moment we are working at $\sim 410\,^\circ\text{C}$.
As well as the temperature the amount of lithium that is placed inside the oven is an important parameter. The more lithium the nearer is the desorption surface of the lithium to the viewports for the 2D-MOT beams, meaning that the danger for the glass being contaminated with lithium in direct line of sight raises. If we put less lithium inside the chamber we need to refill the oven earlier in time. A calculation for the time until the oven needs to be refilled is not very reliable because melting of lithium in a ultra-high vacuum (UHV) chamber has complex dynamics:

- Lithium that was heated once but did not exit the oven can be heated for another time from another position.
- Lithium has a relatively high surface tension meaning that wetting inside the oven is slow [73] and the surface of emittance A_e of the initially block shaped lithium inside the oven is unknown.
- There is not only pure lithium inside the chamber. Already a few minutes of exposure to air lead to reactions with nitrogen and water. As a result, the surface of a lithium block is mainly covered with Li_3N and LiOH [73]. When

[2] Omega: 5SC-GG-KI-30-2M
[3] Picotech: TC-08
[4] Horst: HS 42. These low voltage DC-wires are wound around the oven in a way that minimizes arising magnetic fields and are fixed by using hose clips.
[5] Horst: BCTEX Vlies 13 mm
[6] Hameg: HMP4040
[7] ednet: HD Web Cam 2.0 MP, factory number: 87211

heating power is applied to the block, this layer[8] partly remains and covers the hot lithium since it has a higher melting point than the metal itself. So the heating power needs to be reduced after breaking this layer. If not, macroscopic splashes of lithium from the oven will make the flux uncontrollable and reduce its lifetime.

Though, a first empirical value for the lifetime of our oven can be set. When filling the oven for the first time in March 2016 with $\sim 3\,\mathrm{g}$ of lithium[9] it lasted for 3 years. The refilling that was performed before writing this thesis with $\sim 20\,\mathrm{g}$ is slightly below the maximum possible value in terms of viewport contamination and should be sufficient for a longer period.

2.3 Properties of the science cell

The science cell is at the core of the experiment and needs to be precisely evaluated. Without any transport of the atoms, the requirements for all stages from the 3D-MOT to the realization of a quantum gas microscope need to be fulfilled at one point in the center of the science cell. Some of these requirements are contradictory so that we need to compromise.

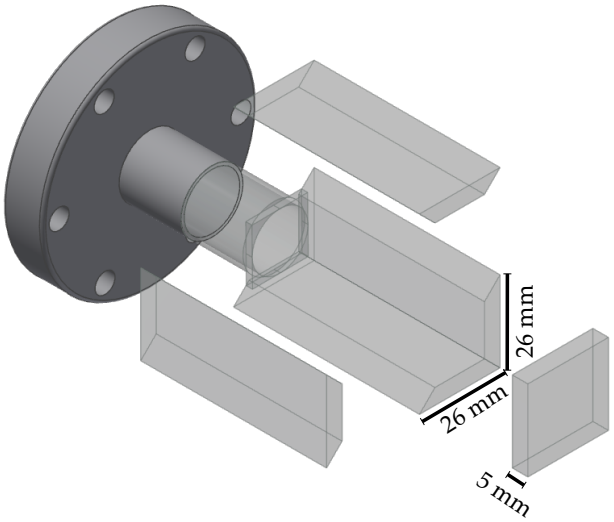

FIGURE 2.4: 3D explosion plot of the science cell – The four main walls are prisms with trapezoidal base area. The parallel planes have a temperature resistant anti-reflection (AR) coating. The other two planes are used for connecting the walls via anodic bonding. The walls are 5 mm thick. The head end wall covers a $26 \times 26\,\mathrm{mm}^2$ square.

Our prior goal is to image fluorescing atoms placed in an optical lattice that is realized in the center of the science cell. In order to reach this goal we take the following design deciscions:

- Including the optical path through the cell wall, the predesigned objective we use in our experiment has a working distance of $\sim 19\,\mathrm{mm}$ (see Chapter 6.1). This restricts the maximum outer dimensions of the cell. In our case, we leave

[8] A good description on how the disturbing layer can be kept to a minimum when refilling the oven can be found in [65].

[9] Half of the lithium is 95 % enriched ^{6}Li and the other half is with natural abundance. In this way we have a fairly well 50 : 50 mixture of both isotopes.

a protection distance of $\sim 6\,\mathrm{mm}$ to the cell wall and get its side length of 26 mm that is the maximum standard length for the manufacturer. Having a cell that is even smaller and allows higher NA with an objective of the same diameter is unfavorable. First, the divergence of focused far-detuned high power laser beams needs to be kept in mind because high intensities on the cell walls go along with thermal lensing issues (see Chapter 4). Second, for the performance of a 3D-MOT a smaller cell is not favorable. In the case of lithium, the standard waist of a MOT beam is around $\sim 10\,\mathrm{mm}$. Since such a large beam would already significantly clip on our cell, we accept a decreased MOT volume but do not want to be even smaller in size (see Chapter 3).

- As we know from earlier quantum gas microscopes, e.g. [20, 29, 74], complexity decreases when the atoms are trapped in a clean interference pattern. For this reason we ordered a science cell[10] where the cell walls have an AR coating from both sides[11]. This means that the coating needs to be applied before the cell assembly (see Figure 2.4). Hence, the chosen coating requires a temperature stability that allows anodic bonding as it is the required assembly technique. Nevertheless, this advanced technique limited us to chose a borosilicate glass named SCHOTT BOROFLOAT 33. In terms of thermal lensing issues when using intense laser radiation this glass is not optimal[12] (see Chapter 4).

- A rule of thumb in optical engineering sets the surface flatness of the cell walls to $< \lambda/4$ for having a diffraction limited image [76]. Hence, we further decided to have 5 mm thick cell walls in order to be sure that bending due to the evacuation is negligible. Cell walls that are even thicker are unfavorable because of issues due to thermal lensing when using intense laser radiation (see Chapter 4). Moreover, for a different thickness of a cell wall, a microscopy with diffraction limited resolution can only be realized with a revised objective design.

2.4 Vacuum

Having the right vacuum conditions inside the chamber is one essential building requirement of a quantum gas experiment. This section contains an explanation of the design for pumping and venting the chamber and highlights the route to our working conditions.

2.4.1 Pumping

As already seen in Figure 2.2 our chamber consists of a 2D-MOT region and a 3D-MOT region that are separated by a differential pumping stage. It is reasonable that for pumping purposes both regions have separated pumps. Since both regions have a comparable volume[13] they are equipped with similar pumps. On each side an ion-getter pump[14] (NEG) is installed (see Figure 2.5). Even if the chamber is fully

[10] ColdQuanta: Custom coating design, see [69]

[11] For the quadratic head end wall the inside coating is only applied on a $13 \times 13\,\mathrm{mm}^2$ centered square.

[12] As mentioned e.g. in [75] fused silica (SiO_2) would be preferably considering thermal lensing effects.

[13] 2D: $\sim 5.0\,\ell$; 3D: $\sim 3.5\,\ell$

[14] SAES Getters: NEXTORR D500-5

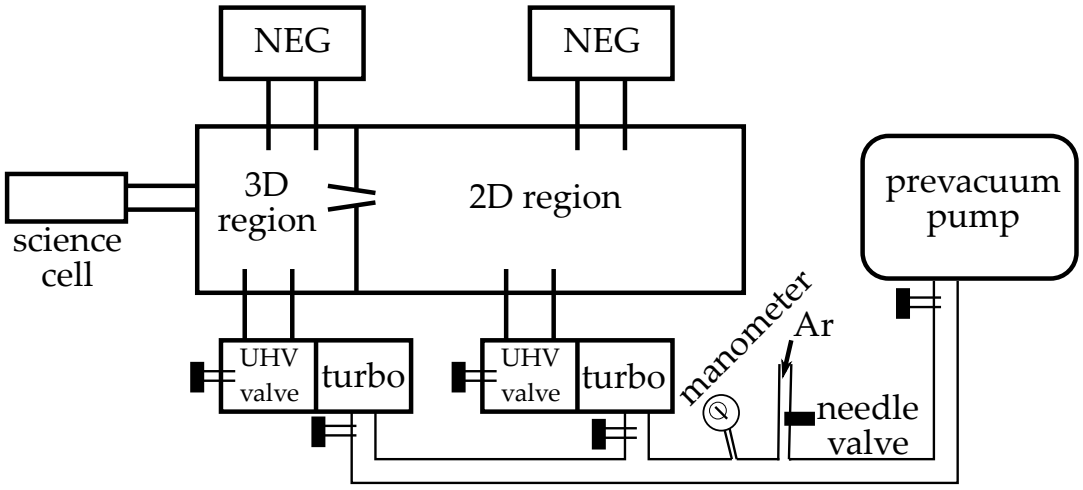

FIGURE 2.5: Sketch of the installed pumping system – We use two ion-getter pumps (NEG) for continuous pumping, two UHV valves in front of two HiPace80 turbo pumps for each region. Behind the manually actuated valves connected at the backside of the turbo pumps the regions are again connected via bellows and tee connectors. A manometer and a needle valve are installed for venting. A valved prevacuum pump finalizes the pumping system.

closed by the UHV valves[15], these pumps are always running. The turbo pumps[16] are flanged directly behind the UHV valves. The backside of both turbo pumps is also valved[17] and then connected to a small needle valve[18] and a manometer[19] that are used for venting. Behind this small venting station the hose can be again closed by a valve[20] before finally the prevacuum pump[21] is connected.

2.4.2 Venting

When there is the need of opening the chamber there are some aspects to be considered in order to keep humidity away from the baked steel walls:

- The chamber should be vented best with argon. In a lithium quantum gas experiment care must be taken by using other venting gases like nitrogen because they may undergo chemical reactions with the lithium.
- Before venting, the region behind the UHV valves should be pumped at least once by the prevacuum pump. It is better to pump twice: At first pumping all air out of the prevacuum system, then venting this region with the venting gas and then pumping the venting gas.
- Before opening the UHV valves, the valve in front of the prevacuum pump should be closed. Do not switch off the prevacuum pump before the valve is closed again.

[15] VAT: 54136-GE02
[16] Pfeiffer Vacuum: HiPace 80
[17] Pfeiffer Vacuum: DVC 016SX and AVC 016 SA
[18] Balzers: EVN 010 H1
[19] Pfeiffer Vacuum: 120C-MAN016-Int
[20] Pfeiffer Vacuum: DVC 016SX
[21] Agilent: Varian TriScroll 600

- When the UHV valves are opened, the pressure at the input of the needle valve should be increased to an excess pressure[22] of the venting gas that is $\sim$ 10 mbar. The excess pressure is maintained until the prevacuum pump is running again.
- When opening the needle valve slowly, the needle on the manometer should rise slowly (ca. 10 min) to the final pressure.

2.4.3 The route to our working conditions

A successful pumping procedure is not only a question of knowledge, experience and accuracy but also of patience and confidence. Figure 2.6 shows the measured pressure[23] inside the chamber during the first pumping scenarios from March until August 2016 and may help as an orientation in the future. The following steps are highlighted:

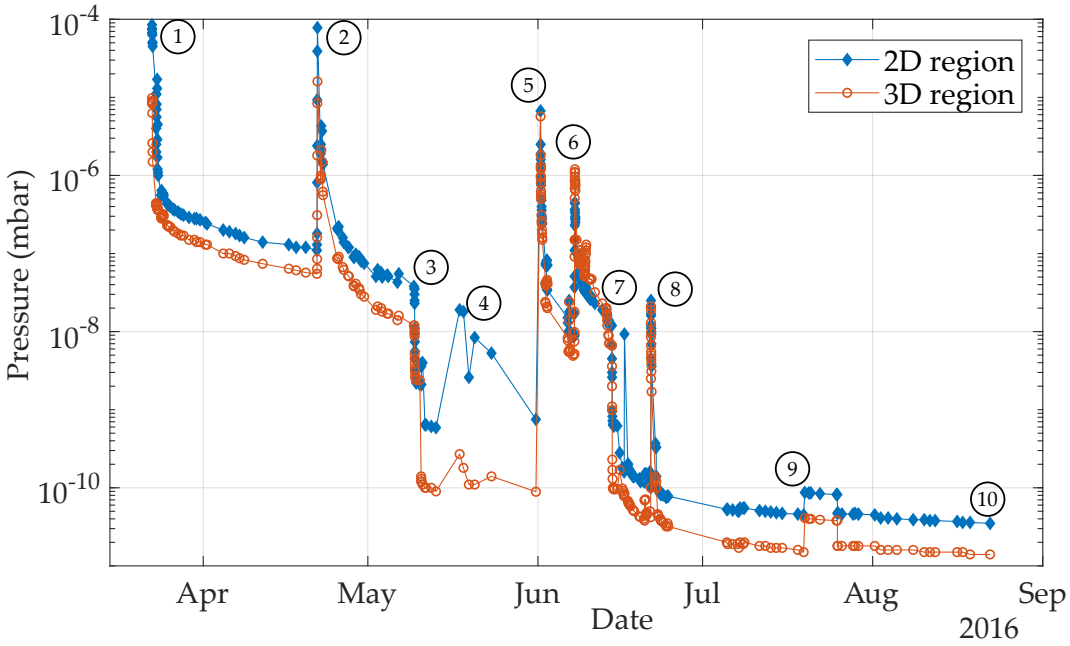

FIGURE 2.6: Measured pressure during the pumping procedure in 2016 – The data points for the 2D region (filled diamonds) and the 3D region (red circles) are respectively connected by lines for guiding the eye. The encircled numbers correspond to the events that are further explained in this subsection.

(1) **March 22:** $\sim$ 15 min after starting the water-cooled turbo pumps to 90 000 rpm we switch on the measurement gauges. The chamber is assembled without flanging the science cell but a blind flange instead in order to have an easier bake out procedure.

(2) **April 21:** After performing many acetone leak tests, installing all heating wires, tapes and thermistors, shielding all viewports with special aluminum disks and using a lot of aluminum foil for shielding and insulation we start the bake out at 150 °C as uniformly as possible.

[22] As a pressure relief valve we use a glove with a small cut in a finger tip.
[23] Pfeiffer Vacuum: IKR070 cold cathode gauge, order no. PT R20 501

(3) **May 9:** We cool back to room temperature and free the chamber from aluminum foil and glass wool that was mainly coming from the heating tapes. Because glass wool is very sticky, the best cleaning method was reached by cleaning every centimeter of steel with adhesive tape.

(4) **May 13:** We heat the oven to $\sim$ 420 °C. By shining a laser beam through a viewport we can see fluorescence of the gaseous lithium inside the chamber. Additionally, we test the performance of the differential pumping tube and observe a maximum possible pressure gradient of two orders of magnitude in the UHV regime.

(5) **June 1:** After cooling the oven back to room temperature we reopen the chamber to flange the science cell. We adjust the orientation of the cell walls with a tubular spirit level placed on top of the cell.

(6) **June 7:** We release the magnetic cover from the ion-getter pumps and heat them to 200 °C. The oven is heated to 100 °C. The science cell is covered by a hollow aluminum cylinder that is wound with a heating wire. The front sides of the cylinder are closed with a special aluminum disk and KAPTON tape[24]. The insulation is again done by wrapping the cylinder with aluminum foil. Care is taken that no cold air can travel through the insulation layers and crack the cell. In order to control the homogeneity of the heating, two thermistors are attached to the glass cell by using tiny strips of KAPTON tape. One is placed on the tube of the science cell, the other is fixed on a small unpolished side of the quadratic head wall. The temperature is slowly increased with a maximum speed of 5 °C/hour. The final temperature of 100 °C for the science cell is reached after 2 days and we stay there for 4 days.

(7) **June 15:** We reach room temperature and remove the heating wires from the ion-getter pumps. We install their magnetic covers and activate the getter material inside the pump by heating it for 1 hour to 550 °C. We then switch on the ion pump units and after a few hours we close the UHV valves. We tightened the valve screws to 6 Nm. The only way to know whether the valves are closed or not is to shut down the turbo pumps.

(8) **June 21:** After releasing their magnets, we start to heat the cold cathode gauges to 200 °C for one day. During that day we note the pressure measured with the ion pump.

(9) **July 19:** We change the ion pump voltage from 6 kV to 3 kV and back to 5 kV and keep this value for $\sim$ 3 years.

(10) **August 22:** Over time the pressure in the chamber decreases. At 1.3×10^{-10}mbar in the 2D-MOT region and 1.3×10^{-11} mbar in the 3D-MOT region, we declare the pumping procedure to be successfully finished.

[24]Conrad: 541860-62, product 926 from 3M

2.5 Coils

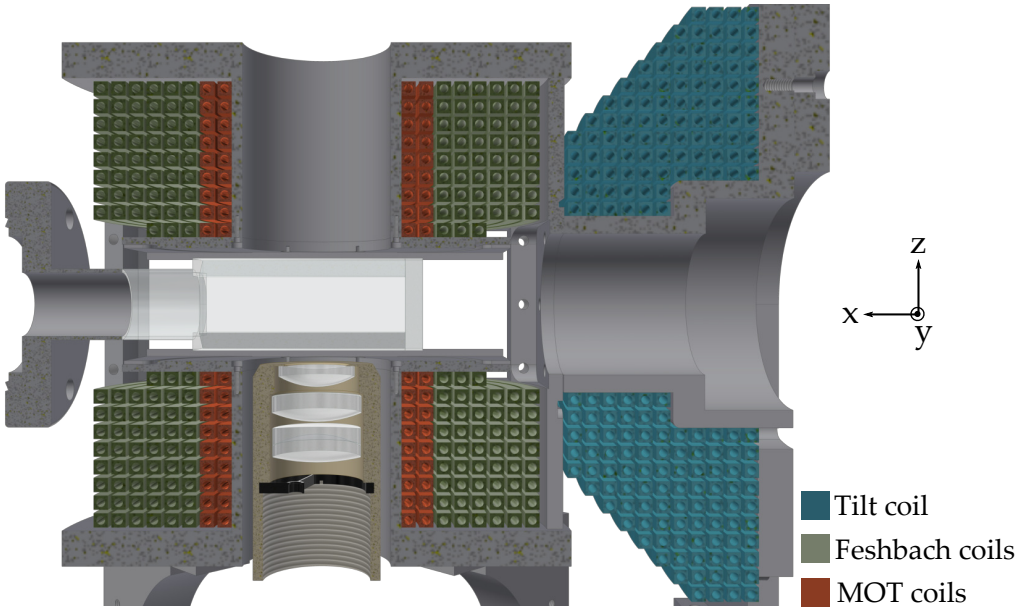

FIGURE 2.7: Vertical cut through the water-cooled hollow-core conductor coils placed around the science cell and the high resolution objective – All coils are wound out of the same copper conductor that has a cross-sectional area of a $4 \times 4\,\mathrm{mm}^2$ square with a 2.5 mm diameter hollow core. The color code gives information about which winding belongs to which coil.

For many different stages in a quantum gas machine, magnetic fields are required, e.g. for a MOT (see Chapter 3) or for tunable scattering properties of the atoms (see Chapter 4). During his Master's thesis [76] Michael Hagemann designed water-cooled hollow-core conductor coils that were used during this thesis and shall be shortly introduced[25] here.
The magnetic field on the atoms is mainly provided by one single coil and two concentric pairs of coils (see Figure 2.7). The inner pair is supplied in anti-HELMHOLTZ configuration and provides the gradient field for the 3D-MOT (MOT coils). The outer pair (Feshbach coils) is supplied in HELMOLTZ configuration and provides a homogeneous offset field that is needed to adjust the s-wave scattering length of lithium atoms along their Feshbach resonances (see Figure C.1 and [62]). The single coil (Tilt coil) has its winding axis perpendicular to the pairs. Supplying that coil breaks the radial symmetry of the magnetic field provided by the Feshbach coils. It thus allows to turn the field vector e.g. towards an axis of weaker trap confinement. This helps to evaporatively cool a two-dimensional gas placed in one layer of a 1D-lattice without populating other layers [77]. Moreover, the Tilt coil also provides the possibility to investigate other scenarios as e.g. described in [78, 79].
In our setup all coils can be supplied with a maxmimum current of $I_{\mathrm{max}} = 200\,\mathrm{A}$. The factors for the coil pairs that convert a current to a magnetic offset field or a magnetic gradient field are given in Table 2.1. Supplying only the Tilt coil with I_{max} results in an offset of 226 G and a gradient of 54.5 G/cm along its winding axis at the position of the atoms. For the case of supplying combinations of different coils, the

[25] More information about e.g. the cooling of the coils and our IGBT switching circuit will be found in the future PhD thesis of Michael Hagemann.

resulting total magnetic field can be estimated with the help of a simulation maintained by Michael Hagemann [76].

TABLE 2.1: Calculated conversion factors from [76] for a HELMHOLTZ (HH) and a anti-HELMHOLTZ (AH) configuration of the MOT coil pair and Feshbach coil pair.

	AH (G cm^{-1}A^{-1})	**HH (G A^{-1})**
MOT coils	0.9	1.8
Feshbach coils	1.7	5.9

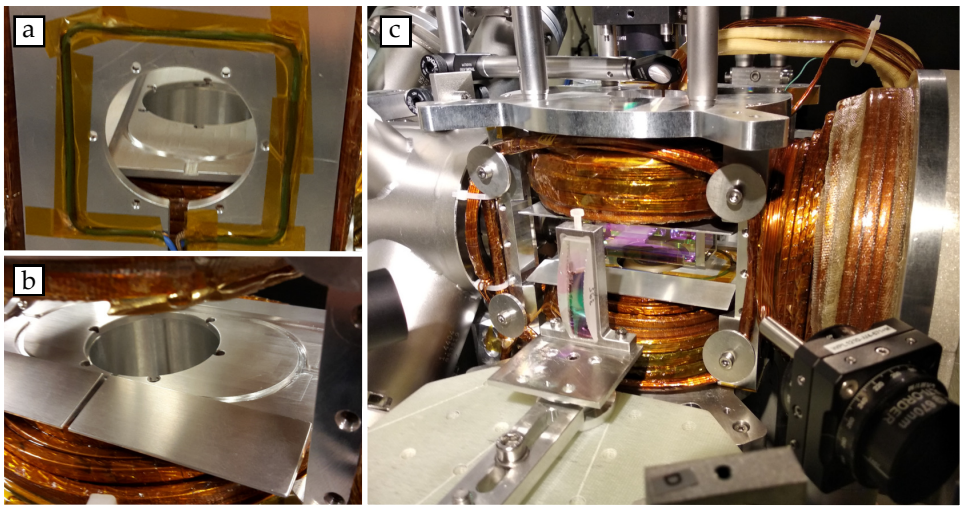

FIGURE 2.8: Photographs of the coils assembly – (a) The conductor loop inside the cover plate of the Tilt coil is a $55 \times 55\,\mathrm{mm}^2$ square. (b) The cover plate of the coil pairs has a $19 \times 110\,\mathrm{mm}^2$ angled surface on each side for gluing mirrors and a premilled racetrack path for conductor loops that were attached during the assembly. (c) A photograph shows the assembly of all coils.

The aluminum winding bodies and holders that mechanically fix the MOT coils, Feshbach coils and the Tilt coil to a common origin of a coordinate system that is placed at the position of the atoms, are designed by the author and realized in the mechanical workshop. They have the following design highlights (see also Figure 2.8):

- **Avoiding eddy currents:** In order to allow short switching times[26] we carefully designed slits in the holder geometry. For the winding bodies we fill the slits with an organic thermoplastic polymer[27] in order to avoid body deformation when stress is applied.

- **Positioning without reducing accessibility:** The distance holders between the upper and the lower Feshbach and MOT coils need to fulfill the requirement that MOT beams at $\pm 45^\circ$ can propagate freely without clipping but safely hold $\sim 3\,\mathrm{kg}$ of copper, epoxy resin, aluminum and water. On account of these two considerations three spacers hold the upper part of the MOT- and Feshbach coils. There are two tiny distance holders on the side of the vacuum chamber

[26] We measure a switching time $< 100\,\mu\mathrm{s}$ for switching a maximum field of $\sim 1180\,\mathrm{G}$ to zero.
[27] PEEK: PolyEther Ether Ketone

and a larger one at the side of the Tilt coil. All have additional M4 tapped holes for future attachment possibilities. Likewise, the larger distance holder for the Feshbach coils serves as a cover plate of the Tilt coil. Hence, the Tilt coil is automatically positioned correctly with respect to the coil pairs.

- **Utilization of free space:** The cover plate of the Tilt coil as well as the cover plates of the two parts of the coil pairs have premilled tracks. We filled these tracks with conductor loops that shall be used for driving RF transitions between different Paschen-Back states at $\sim 80\,\mathrm{MHz}$ that is e.g. done in [80].
  Additionally, the long edges of the two cover plates of the coil pairs are cut to a rectangular surface at an angle of 12.5° such that flat mirrors[28] can be glued whenever space gets limited.

A magnetic background field coming e.g. from the Earth, from the permanent magnets for the 2D-MOT, from the ion pumps or from the vacuum gauges can disturb the realization of a quantum gas. In order to compensate the background field we wind and install three pairs of coils in each spatial direction.
These so-called compensation coils are wound by the author and made of an insulated copper wire[29] that has a diameter of 1 mm. A noticeable increase of temperature $> 30\,^{\circ}\mathrm{C}$ is found at currents $> 5\,\mathrm{A}$. For fixing and stabilizing each coil we used KAPTON tape[30]. In all three spatial directions the pairs of coils have colored connectors that indicate the intra-pair distance between the coils. They go from black to red to yellow.

- The offset coils in z-direction have 11 windings each. They are concentrically imposed on the Feshbach coils and additionally fixed in shape with QUIKSTEEL epoxy paste[31]. Their radius is $\sim 60\,\mathrm{mm}$ and the distance between the coils depends on their color code[32].
- The offset coils in x-direction have 5 windings each and a $\sim 50\,\mathrm{mm}$ radius. Their distance is $\sim 138\,\mathrm{mm}$. At one side, the coils are wound along the tip of the Tilt coil. At the other side, the coils are concentrically fixed around the science cell tube.
- The offset coils in y-direction have 5 windings each and a curved rectangular shape. The small side of the rectangle along z-direction measures $\sim 100\,\mathrm{mm}$, the long side is a circular arc around the Feshbach coils measuring $\sim 110\,^{\circ}$ on a diameter of $\sim 130\,\mathrm{mm}$. They are fixed to the distance holders between the Feshbach coils. The distance of a compensation coil is $\sim 84\,\mathrm{mm}$ within each pair.

For all coil pairs Table 2.2 shows the measured conversion factors for the center of the coil assembly.

[28] e.g. Thorlabs: PFR10-P01
[29] Conrad: 605660-62, max. temperature 155 °C
[30] Conrad: 541860-62, product 926 from 3M, max. temperature 180 °C
[31] Conrad: 479062-62, max. temperature 260 °C
[32] yellow: $\sim 118\,\mathrm{mm}$, red: $\sim 100\,\mathrm{mm}$, black: $\sim 82\,\mathrm{mm}$

TABLE 2.2: Measured conversion factors for a HELMHOLTZ (HH) and a anti-HELMHOLTZ (AH) configuration of the offset coil pairs. The measurement is performed by stepping through the center of the coil geometry with a 3-axis Hall effect magnetometer. The estimated measurement error is $\pm 5\,\%$. (The data is measured by Michael Hagemann and Malte Hagemann and further analyzed and evaluated by the author.)

	AH (mG cm^{-1}A^{-1})	**HH (mG A^{-1})**
x-dir.		
yellow	76	260
red	72	206
black	74	292
y-dir.		
yellow	98	488
red	100	496
black	108	494
z-dir.		
yellow	260	840
red	300	1040
black	320	1300

2.6 Overview on trapping laser beams

Without any transport after the 3D-MOT all laser beams need to coincide at the focal point of the high-NA objective that collects the photons for quantum gas microscopy. Figure 2.9 shows design sketches of all important laser beams intersecting on that point that are prepared and aligned within the course of this thesis.
The horizontal molasses beams are entering at an angle of $\pm 45^\circ$ in the xy-plane. Together with the vertical molasses beams where one is propagating through the objective (see Chapter 6.1.2) they serve for the 3D-MOT as well as for the gray molasses described in Chapter 3.
At an angle of $\pm 10^\circ$ the beams for a 100 W far red-detuned optical dipole trap enter horizontally (xy-plane). They are shone in for an all-optical evaporation. Their intensity control is realized via a combination of a half-wave plate on a motorized rotation mount and Glan-Laser polarizers (see Chapter 4).
Our lattice configuration (see Chapter 5) consists of a vertical 1D-lattice with dynamically tunable spacing via a so-called optical accordion [81, 82] and a horizontal triangular lattice. For the accordion two red-detuned beams are focused to a waist of 48 μm and interfere vertically (yz-plane) at a full opening angle between $\sim 2^\circ$ and $\sim 30^\circ$. The three beams of the triangular lattice are red-detuned as well and shaped to a waist of $\sim 40\,\mu$m. One beam is shone through the quadratic front wall of the glass cell. The other two beams hit the atoms at a horizontal angle of $\pm 120^\circ$ with respect to the first one.

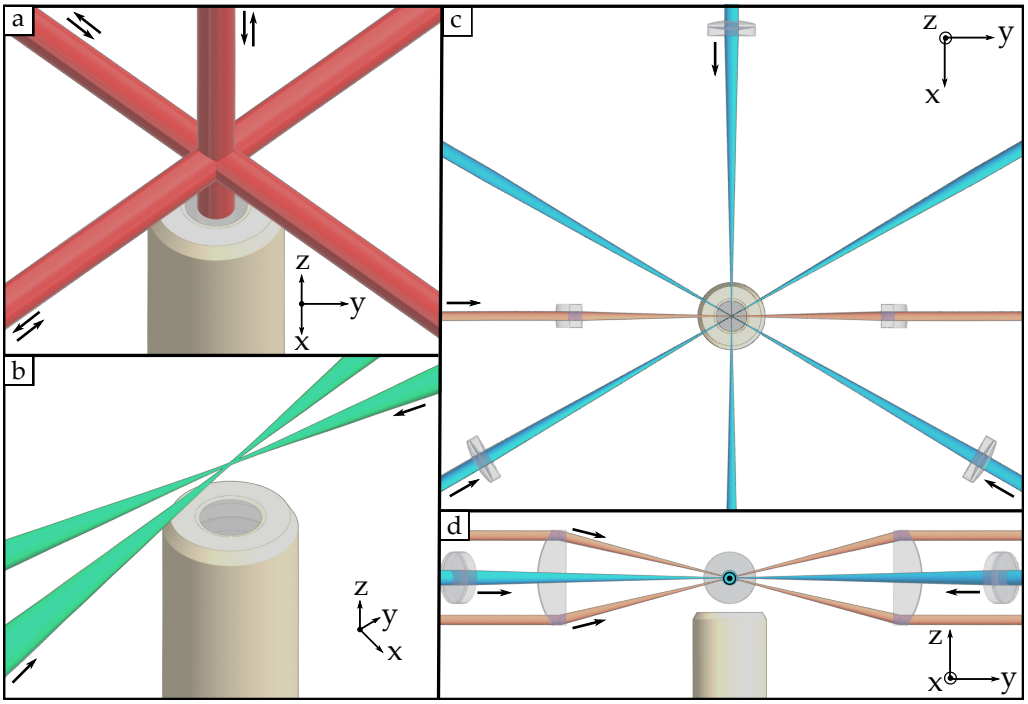

FIGURE 2.9: Design sketches of the laser beams above the high-NA objective – For simplicity the science cell is blanked out. The arrows next to the beams indicate their propagation direction. (a) The 3D-MOT beams at 671 nm are already intersecting above the objective. (b) The beams of the optical dipole trap at 1070(3) nm intersect horizontally at the focus position. (c) A horizontal sketch of all pinning beams at 1069.8 nm: The beams for the triangular 2D-lattice (blue) are focussed by achromatic lenses and intersect at 120°. (d) A vertical sketch of all pinning beams: The beams (orange) of the accordion lattice in z-direction are focused to the intersection point by an aspheric lens. A second lens behind the intersection recollimates them.

2.7 Experimental control

An important building element for a quantum gas experiment is a versatile experimental control software where all timings, ramps and commands needed for a sequence can be designed and planned in detail.
As illustrated in Figure 2.10, the experimental control of the lithium experiment is based on a adapted version of *Cicero Word Generator* [83] and differs on its basis from the group intern LabVIEW solution since it is written in a much more flexible programming language, named C#. Essentially, the software is separated into two parts:

- **Cicero** is the client program where a user designs an experimental cycle on a PC.
- **Atticus** is the server program that manages the output of the designed experimental cycle.

With its graphical user interface (GUI) *Cicero* is the central building element of the experimental control software. The sequence is sent via TCP/IP to a server computer in our network that runs *Atticus*. This software converts[33] the sequence description

[33]This conversion did not exist in [83] but is crucial for us to be compatible with the group internal eletronics.

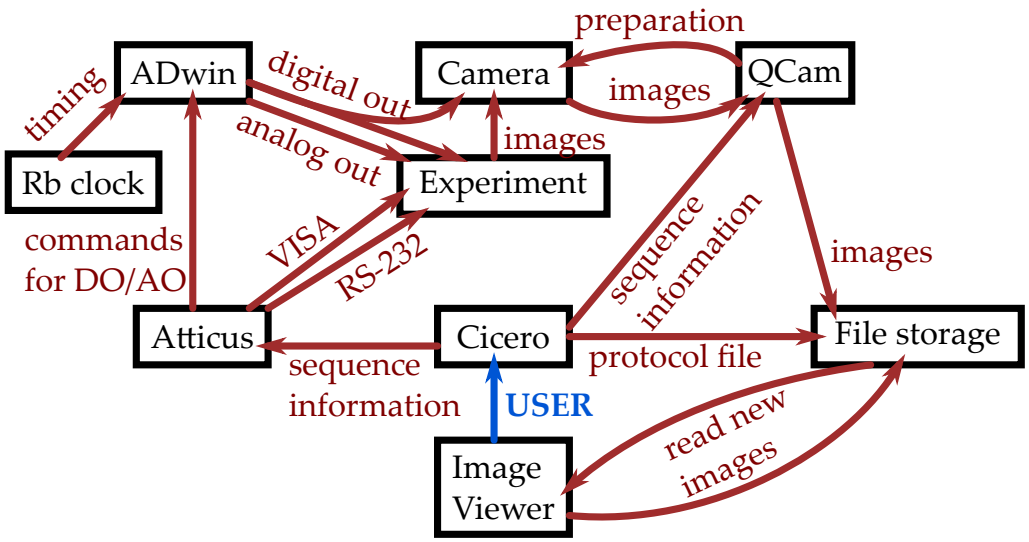

FIGURE 2.10: Overview of the experimental control – In the software program *Cicero* the user designs an experimental cycle. It can be run on any PC in the network. We install a server that runs *Atticus* in our laboratory. It manages the communication with all devices needed for the execution of a sequence, especially with the *ADwin* processor that outputs all digital and analog voltage signals. It is timed via a Rb frequency standard. For the camera control we use another PC on which we run the *QCam* software and the *ImageViewer* software. The protocol file and the images of a sequence are stored on a separate file storage.

for the *ADwin Pro II* system[34] that controls our experiment on the hardware side. Its output can be either a digital TTL signal[35] or a ± 10 V analog signal[36]. All text-based commands are sent directly from the server computer via a RS-232 connection or (and much more preferably) as VISA commands via TCP/IP into our network. All timings during the experiment are additionally clocked via a rubidium frequency standard[37].
Simultaneously, *Cicero* stores a protocol file to a file storage and sends commands to a camera PC where a Camera Software, named *QCam*, is running. It is developed on the basis of [84] and sends preparatory commands to our cameras for imaging and manages their storage.
A live preview of the images after each experimental run with a few fitting algorithms on top is available via the *ImageViewer* software based on Matlab. The software is kindly provided by the BFM team of our group and further revised and developed to work for our purposes.

[34] Jäger Messtechnik with Pro-CPU-T11-ENET
[35] Jäger Messstechnik: Pro II-DIO-32, 32 channels
[36] Jäger Messstechnik: Pro II-AOut-8/16, 16-bit resolution, 8 channels
[37] SRS: FS725/3

Chapter 3

Laser cooling – From a 2D-MOT to gray molasses

Laser cooling is a powerful strategy to slow down the velocity of the atoms in a gas by many orders of magnitude. As a first step in the experimental sequence, this method is essential to load a sufficient number of atoms into far-detuned dipole traps for further potential shaping and manipulation.
This chapter deals with the laser cooling (and trapping) stages that are installed and implemented in the experiment before dipole traps come into play. Here, the author introduces the molasses laser system and shows data from the unconventional 2D-/3D-MOT trapping technique for lithium atoms that we successfully implemented for ^{6}Li and ^{7}Li. Moreover, he reports on gray molasses cooling as a sub-Doppler cooling mechanism for lithium atoms that enhances phase space density for a better loading into an all-optical far-detuned dipole trap. The author elaborated the presented results of this chapter in consultations with B. S. Rem and with the support of Michael Hagemann.

3.1 Molasses laser system

The molasses laser system (see Figure 3.1) is constructed during the author's Master's thesis [69] and further developed by the author as PhD student upon two design principals:

- **Preparation of light on the D2 line for MOT purposes and on the D1 line for gray molasses cooling:**
  For providing laser light on both lines, we lock two separate preamplified ECDL master lasers[1] via saturated absorption spectroscopy. The laser outputs are fibered achieving a clean beam shape and higher exchangeability in terms of repair issues. Furthermore, a clean beam shape helps to overlap the laser light e.g. to couple into the same fiber or to seed the same tapered amplifier at different laser frequencies.

- **Easy applicability to both stable isotopes:**
  For implementing an easy switch betweeen bosonic ^{7}Li and fermionic ^{6}Li, the main part of the laser system that distributes the light to different fibers is maintained in a way that allows isotope-independent functionality without optics replacement. Basically, the switch is implemented via AOMs in the spectroscopy part for each laser and different EOMs that modulate a repumping sideband.

[1] External Cavity Diode Lasers from TOPTICA PHOTONICS

3.1.1 Main system – Distributing the light

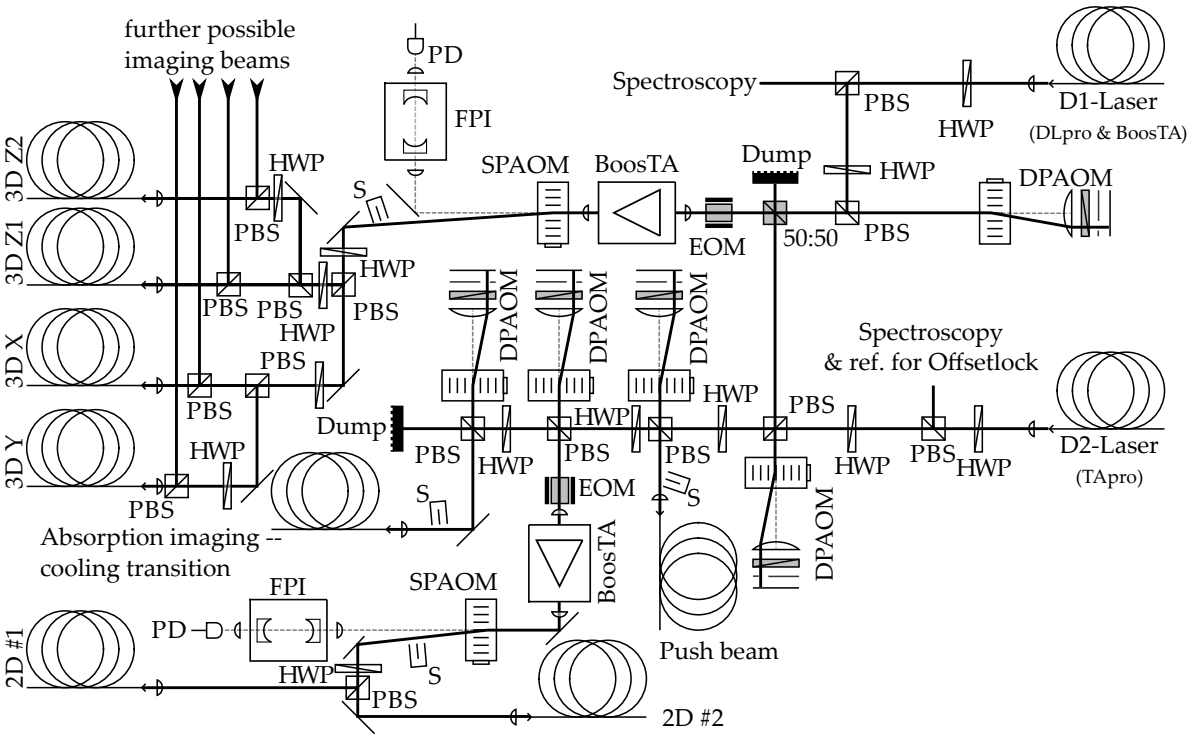

FIGURE 3.1: A simplified overview on the main parts of the molasses laser system – The D2 laser seeds two tapered amplifiers (BoosTA). One is used for the 2D-MOT, the second for the 3D-MOT. The latter can also be seeded by the D1 laser for gray molasses cooling. Additionally, the D2 laser also provides the light for the push beam of the 2D-MOT and a light beam for absorption imaging. For other imaging beams along the MOT axes, we place PBSs in front of the 3D fibers. As a design library for drawing optics components the author used [85].

At the main part of the molasses laser system (see Figure 3.1) the light of the D2 Laser is distributed to different polarization-maintaining single mode fibers[2]. They assure a guided propagation of light from one optical table where the laser system is constructed to the table where the vacuum chamber (see Chapter 2) is situated.
For the 2D-MOT each retro-reflected beam has its own fiber. In front of these fibers, the light is travelling through different optical elements:

- A double-pass AOM (DPAOM) is required for a fine adjustment of the laser's detuning with respect to the atomic transition.
- A phase-modulating EOM is required for closing the cooling cycle via a sideband on the repumping transition (see Figure B.1) and a Fabry-Perot interferometer (FPI) is required to monitor that sideband. In order to be able to maintain the capability of switching between ^{6}Li and ^{7}Li the EOMs have a resonance at the ground state hyperfine splitting frequency of both isotopes.
- A tapered amplifier (BoosTA) is required in order to reach the needed power.
- A single-pass AOM (SPAOM) is required for a fine adjustment and fast switching of the light intensity.

[2]Thorlabs: P3-630PM-FC-10

- A mechanical shutter (S) is needed as an insurance that the light is turned off completely during further manipulation of the ultracold gas.

When cooling and trapping the atoms we recognize that no repumping transition for the 2D-MOT push beam is required.
The light for the 3D-MOT and gray molasses cooling is not needed simultaneously. For that reason both master lasers are overlapped on a 50:50 beam splitter[3]. By separately propagating through DPAOMs before being overlapped, the beams from the two locked lasers are tunable in frequency and the seed of the following BoosTA can be switched. The elements behind the beam splitter have an equivalent purpose as in the case of the 2D-MOT beams.
Finally, the D2 light that is neither distributed to the 3D-MOT nor to the 2D-MOT is needed to perform absorption imaging on the MOT's cooling transition (see Figure B.1). For further purposes the PBSs in front of the 3D fibers (3DX, 3DY, 3DZ1, 3DZ2) allow access in orthogonal polarization.

3.1.2 Spectroscopy – Switching between bosons and fermions

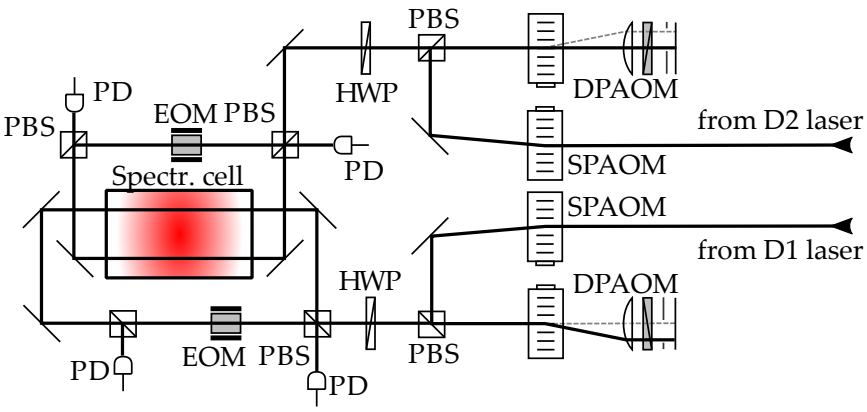

FIGURE 3.2: A simplified overview on the spectroscopy parts of the laser system – For both lasers the setup design is identical. Each have two photodiodes that allwo easy switching between FMS (Frequency Modulation Spectroscopy) and MTS (Modulation Transfer Spectroscopy) as further studied e.g. in [69, 86]. The drawn light path is for trapping and cooling of ^{6}Li. The light path for ^{7}Li is mostly equivalent, only the DPAOMs are switched inversely as indicated with a dashed gray line. As a design library for drawing optics components the author used [85].

Figure 3.2 sketches the spectroscopy part of the laser system. For performing the 2D-MOT and the 3D-MOT the first master is locked to the D2 cross-over resonance of the saturated absorption spectroscopy signal between the two hyperfine transitions. For the second master the locking point is in the vicinity of the respective D1 line in order to install gray molasses cooling. A detailed description of the locking can be found in [69].
When the lasers are unlocked the user can switch the DPAOMs[4] in the spectroscopy part of the laser system respectively for both masters and relock to the right position. Additionally, for the repumping transition the EOMs in front of the BoosTAs in the

[3]For the moment only one output port of the beam splitter is used. Whenever more intensity in the moalsses beams is needed or the vertical and horizontal molasses beams shall be switched separately by different SPAOMs the second output can be seeded into another BoosTA.

[4]For ^{7}Li the DPAOM in the D1 spectroscopy is turned off and the DPAOM in the D2 spectroscopy is turned on. For ^{6}Li the switching logic is inverted.

main part of the laser system (see Figure 3.1) need to be supplied with the correct RF frequency. The frequency as well as the sideband to carrier ratio that is used for the different isotopes is listed in Table 3.1.
When realizing our first 3D-MOT of ^{6}Li in December 12, 2016 at 9:20 pm, we directly tested the functionality of the isotope switch and found our first 3D-MOT of ^{7}Li at 9:45 pm. Within the following years, we concentrated on constructing the experimental apparatus by using ^{6}Li that is studied more extensively in the ultracold atom community. Nevertheless, we carefully considered that changing to ^{7}Li is granted for future purposes.

TABLE 3.1: Settings for the phase-modulating EOMs – When switching the isotope the EOM settings need to be updated.

	2D-MOT	**3D-MOT**
^{6}Li		
RF frequency (MHz)	252.0	231.6
sideband : carrier	0.71	0.67
^{7}Li		
RF frequency (MHz)	857.0	812.7
sideband : carrier	0.25	0.33

TABLE 3.2: Experimentally optimized values of the 2D-/3D-MOT setup for ^{6}Li with respect to the loading rate – The value of $I_{\mathrm{cool,rep}}$ per beam is given in $I_{\mathrm{sat}} = 2.54\,\mathrm{mW/cm^2}$. The power in the wrong EOM sideband is subtracted like described in [69]. All detunings are referenced to the linewidth $\Gamma = 2\pi \times 5.87\,\mathrm{MHz}$.

	2D-MOT	**3D-MOT**
$I_{\mathrm{cool}}/I_{\mathrm{sat}}$	28	12
$I_{\mathrm{rep}}/I_{\mathrm{sat}}$	20	8
beam waist (cm)	0.3/0.6	0.5
sideband : carrier	0.71	0.67
detuning cool. (Γ)	-7.3	-8.7
detuning rep. (Γ)	-3.4	-8.3
detuning push (Γ)	-3.9	-
$I_{\mathrm{push}}/I_{\mathrm{sat}}$	4.7	-
field gradient (G/cm)	56	41
loading rate (atoms/s)		$3 \cdot 10^7$

3.2 Cooling and trapping in a 2D-/3D-MOT setup

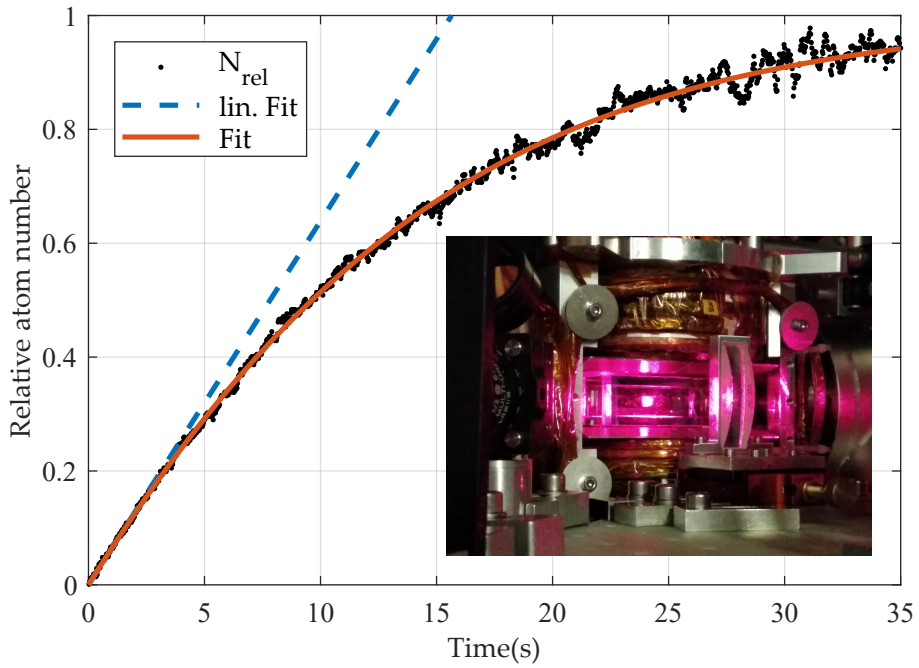

FIGURE 3.3: Loading curve of the 3D-MOT measured via fluorescence photons on a photodiode over the first 35 s – The black dots show the measured data normalized to a relative atom number. The red line is a fit using Equation 3.2. The dashed blue line is a guide to the eye for a constant loading rate of $\sim 3 \cdot 10^7$ atom/s. The inlet shows a smartphone photo of the 3D-MOT in the glass cell.

When running the experimental apparatus, the first step in our sequence is to load a 3D-MOT. The detunings as well as the intensities in our beams are listed in Table 3.2. Further details can be found in [68]. The standard D-line level diagram for ^{6}Li can be found in Appendix B.
As mentioned in Chapter 2 our 2D-/3D-MOT loading scheme permits the 3D-MOT to be at the position of our atom-resolved microscope. In this unconventional setup, we realize a loading rate that is $\sim 3 \cdot 10^7$ atom/s. It is most sensitive to the oven performance (see Chapter 2.2) and to the adjustment of the slightly converging push beam. When not pushing the 2D-MOT, we loose one order of magnitude in the loading rate. For our usual experiments we stop loading after 8 s and work with $\sim 10^8$ atoms.
A deeper analysis of the MOT loading can be performed via a rate equation from [87] that reads

$$\dot{N} = R - \Gamma N - \beta \int n^2(r) d^3r, \tag{3.1}$$

where R is the capture rate, Γ accounts for linear losses and β serves as a coefficient for binary collisions in a Gaussian density distribution $n(r)$. An analytic solution for the relative atom number N_{rel} described by this equation is

$$N_{\mathrm{rel}}(t) = 1 - \frac{\mathrm{e}^{-\gamma t}}{\frac{1}{1+\xi} + \frac{\xi}{1+\xi}\mathrm{e}^{-\gamma t}} \quad \text{with} \tag{3.2}$$

$$\xi = \frac{\beta n_0}{\sqrt{8}\Gamma + \beta n_0}, \tag{3.3}$$

$$\gamma = \frac{1+\xi}{1-\xi} \cdot \Gamma, \tag{3.4}$$

n_0 as the steady state density and ξ as the fraction of binary loss relative to the total loss. We fit this model to our data measured via a photodiode[5] that captures fluorescence photons of the MOT (see Figure 3.3) and get $\xi = 0.37(4)$ and $\Gamma = 0.041(4)\,\mathrm{s}^{-1}$.

To summarize our analysis, we state:

- Our 3D-MOT is well saturated at $\sim 5 \cdot 10^8$ atoms[6]. This value is mainly limited by the relatively small size of the MOT beams that is chosen regarding the size of the glass cell.
- In the steady state regime more than every third lost atom left the trap because of a binary collision and the characteristic time for linear losses is below $1/\Gamma \sim 24\,\mathrm{s}$. Due to a vacuum pressure behind the differential pumping tube of ($1.3 \cdot 10^{-11}$ mbar), we think that background collisions are a minor effect during the loading procedure.

3.3 Compressing the MOT

Just before switching to gray molasses cooling (see Chapter 3.4), we increase the phase space density by compressing the MOT (cMOT) via an immediate jump to a detuning of $\delta_{\mathrm{cool}} = -5.5\,\Gamma$ for the cooling transition and $\delta_{\mathrm{rep}} = -5.0\,\Gamma$ for the repumping transition. Going closer to the theoretical temperature minimum[7] at $-\Gamma/2$ and zero intensity, we also reduce the power in our beams. Therefore, we simultaneously start a linear ramp of 10 ms to 2.5 % of the full MOT intensity given in Table 3.2. We do not change any magnetic fields during the cMOT. Finally we end up at a temperature around 650 μK.

3.4 Gray molasses cooling

As described in Chapter 3.1 we reuse the MOT setup for gray molasses cooling on the D1 line with the same polarization and beam size. While the idea of gray molasses cooling was already developped in the mid-90's [88–91] for rubidium, sodium and cesium, it is recently revised to cool lithium and potassium to sub-Doppler temperatures [92–94].
Gray molasses cooling requires blue-detuned light frequencies ($\delta > 0$), such that the light shift of the dressed ground state energy increases to

$$\Delta_L(\Omega) = \hbar\delta \cdot \sqrt{1 + \left(\frac{\Omega}{\delta}\right)^2} \tag{3.5}$$

[5] Thorlabs: PDA36A
[6] An atom number calibration is performed via absorption imaging.
[7] Doppler temperature: 140 μK

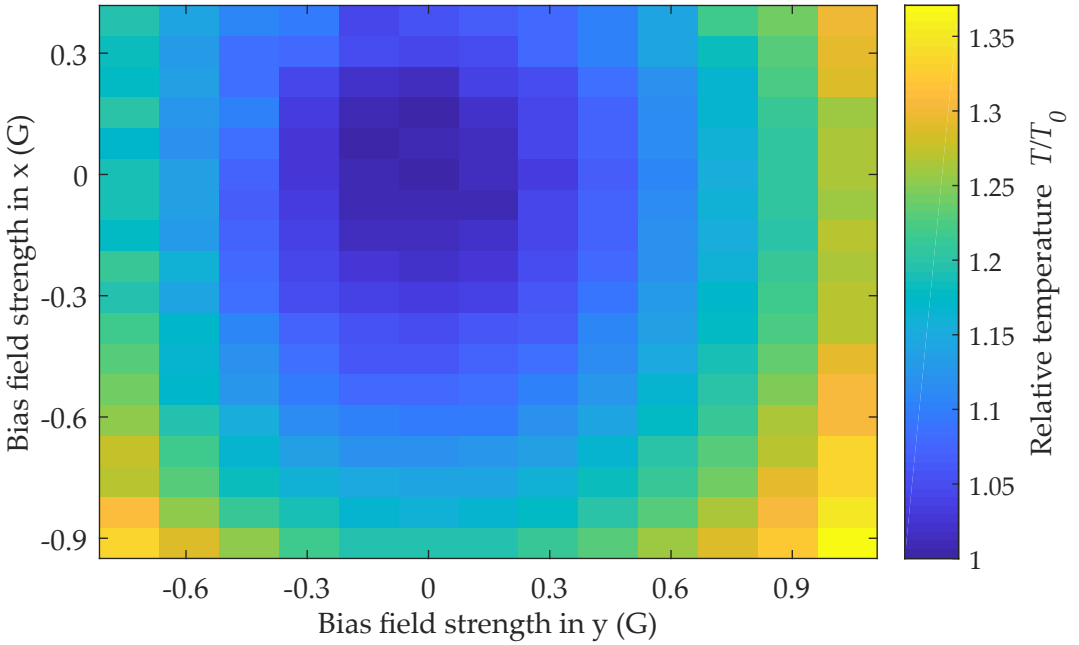

FIGURE 3.4: Relative temperature dependence of gray molasses in the vicinity of zero magnetic field – For the data points we measured the width of the cloud in the linear time-of-flight (ToF) regime where $\sigma(t_{\mathrm{ToF}}) \propto T$. The current in the compensation coils for the x- and y-direction is changed before each experimental run. The optimum magnetic field compensation $B_x = 1.14(3)\,\mathrm{G}$ and $B_y = 1.18(6)\,\mathrm{G}$ is subtracted from the axes. $B_z = 0.48(2)\,\mathrm{G}$ is kept at optimum.

with Ω being Rabi frequency. Considering the m_F-subspace of a hyperfine state in the polarization landscape of the molasses at zero magnetic field, one can see that each substate is described via its Rabi frequency $\Omega_{m_F}(\vec{r})$ that depends on the local polarization. Furthermore for every local polarization of light one can find so-called dark states for the D1 transitions that are defined to have a vanishing Rabi frequency $\Omega = 0$ [95]. A detailed description of the dark states in the polarization landscape of a gray molasses for ^{6}Li can be found in [93, 96].
If the molasses cooling is performed at non-zero magnetic field, the degeneracy of the bare m_F-subspace is repealed and the detuning between different substates reduces the cooling efficiency. In order to quantify this effect we can define a relative temperature T/T_0, where T is the temperature for the non-zero magnetic field strength B and T_0 is the minimum temperature. We then find experimentally that in the vicinity of T_0, the relative temperature rises quadratically as

$$\frac{T}{T_0} = 1 + \kappa B^2 \tag{3.6}$$

with $\kappa \sim 0.25\,\mathrm{G}^{-2}$ (see Figure 3.4).
As well as for the standard MOT that is performed red-detuned to the D2 line, gray molasses cooling on the D1 line needs a cooling and a repumping transition[8]. This is where another feature of the gray molasses can be exploited. A so-called Λ-enhancement of the cooling is observed when the cooling cycle is closed and both hyperfine ground states are involved.
Considering that we are working with D1 light that is blue-detuned to the cooling

[8]For ^{6}Li the cooling tansition is starting from $F = 3/2$ and the repumping from $F = 1/2$ respectively (see Appendix B).

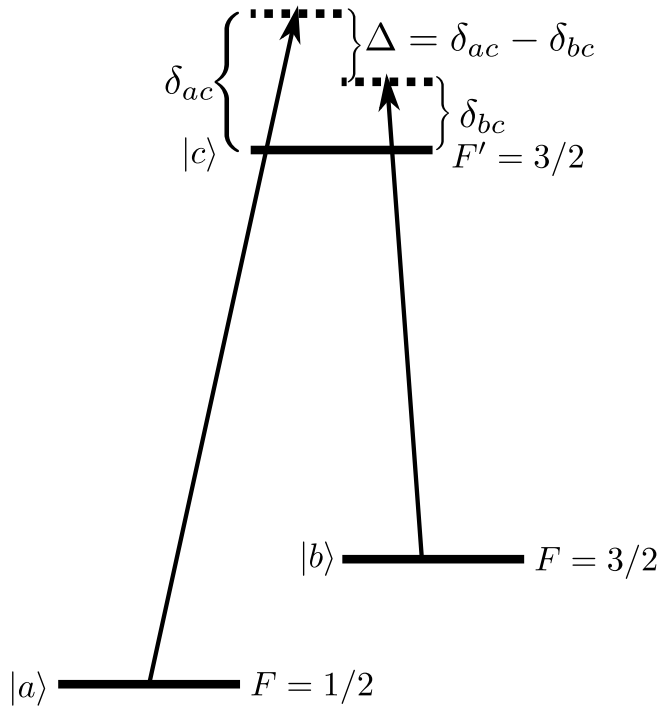

FIGURE 3.5: Nomenclature of the Λ-system applied to describe Λ-enhancement in gray molasses cooling for ^{6}Li – The two hyperfine ground states $|a\rangle = F = 1/2$ and $|b\rangle = F = 3/2$ couple to the $|c\rangle = F' = 3/2$ excited state on the D1 transition. Both laser frequencies are blue-detuned $\delta_{ac,bc} > 0$. The detuning difference is called two-photon detuning Δ.

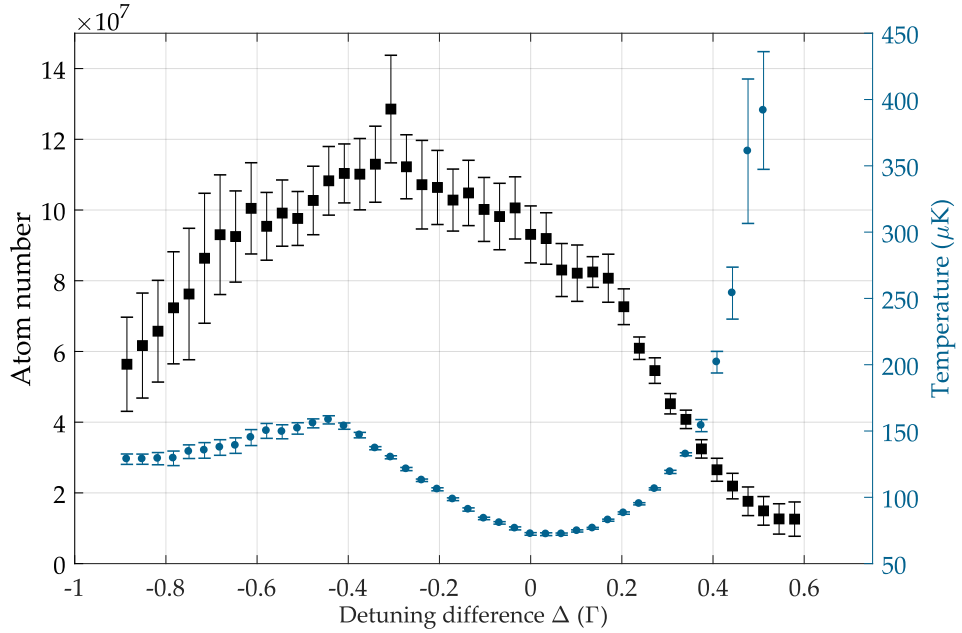

FIGURE 3.6: Δ dependence of the temperature and the atom number – At the Raman resonance $\Delta \sim 0$ the temperature (blue dots) drops to $T_o = 72(1)\,\mu$K which is considerably lower than the Doppler temperature $T_D = 141\,\mu$K. At this point the molasses contains $\sim 80\,\%$ of the initial atoms (black squares). The data are extracted from time of flight measurements. The errorbars show a weighted standard deviation error of single fit values.

and the repumping transition respectively (see Figure 3.5), an additional cooling effect can be well explained via a Λ-system where $|c\rangle$ corresponds to the excited state

and $|a, b\rangle$ to the ground states.
Here, the two-photon detuning $\Delta = \delta_{ac} - \delta_{bc}$ plays an important role. For small repumping, i.e. $\Omega_{ac} \ll \Omega_{bc} = \Gamma\sqrt{I/2I_{\text{sat}}}$, one can dress the states $|b\rangle$ and $|c\rangle$ as an Autler-Townes doublet [93]. The analysis then shows:

- In the case of $\Delta > 0$ and $|\Delta| \lesssim \Omega_{bc}$ the atoms are heated.
- In the case of $\Delta \leq 0$ and $|\Delta| \lesssim \Omega_{bc}$ there is an enhanced cooling effect.
- In the case of $|\Delta| \gg \Omega_{bc}$ there is a remaining cooling effect coming from the dark states in the m_F-subspace.

By tuning the RF frequency supplied to a phase modulating EOM [97] we experimentally change Δ within a region where $|\Delta| < \Omega_{bc}$ (see Figure 3.6). Optimal cooling conditions are achieved when $\Delta \sim 0$ with a capture efficiency of $\sim 80\,\%$. Around this Raman resonance point we reach a minimum temperature of $72(1)\,\mu$K and the atoms are transferred into a coherent dark state

$$|\text{NC}\rangle \propto |\Omega_{ac}|\,|b\rangle + e^{i\phi}|\Omega_{bc}|\,|a\rangle\,, \tag{3.7}$$

where $\phi = \phi_{bc} - \phi_{ac}$ is given by the relative phase between the two complex Rabi frequencies $\Omega_{ac/bc}\, e^{i\phi_{ac/bc}}$ [98].
The dark state $|\text{NC}\rangle$ is our starting point to prepare the atoms for evaporative cooling (see Chapter 4). In the case of ^{6}Li we want the atoms to be in state $|a\rangle = |F = 1/2\rangle$. Hence, after applying our usual gray molasses for 1.75 ms at optimized parameters (see Table 3.3), we set the repumping Ω_{ac} to zero via the phase modulating EOM and lower the intensity on the cooling transition to $6.0(2)\,\%$ of the initial value (see Table 3.3) for $25\,\mu$s. In order to be sure that there are no remaining atoms in state $|b\rangle = |F = 3/2\rangle$ we shine in resonant light for $50\,\mu$s with an intensity of $0.11(5)\,I_{\text{sat}}$ per beam. After all manipulation steps, we end up with typically 10^8 atoms purely being in the $|F = 1/2\rangle$-state at a slightly higher temperature of $\sim 84\,\mu$K and a phase space density around $4 \cdot 10^{-6}$.
We think that in our case the minimum temperature after gray molasses cooling is mainly limited by the permanent magnets producing the double quadrupole field for the 2D-MOT which is 230 mm away (see Figure 2.2). Hence, without any gradient compensation[9] the field in the glass cell is still at $\sim 0.2\,$G/cm. Since the repumping light is provided by phase modulation in an EOM, another source of heating might be off-resonant scattering that is induced by the unused red sidbeand.
All in all, the purpose of gray molasses cooling for our experiments is to load a sufficient number of atoms into the optical dipole trap for evaporation (see Chapter 4). Within the reached parameter range we find $\sim 3\,\%$ of the atoms in the dipole trap before starting the evaporation. This ratio is comparable with other experiments, e.g. [99], and satisfactory for our purposes.

[9] A detailed analysis as well as possible compensation ideas are to be found in [69].

TABLE 3.3: Optimized values of gray molasses cooling with respect to the phase space density – The value of $I_{\text{cool,rep}}$ per beam is given in $I_{\text{sat}} = 2.54\,\text{mW/cm}^2$. The power in the wrong EOM sideband is substracted like described in [69]. T_0 is the minimum temperature. As well as the given phase space density this value is reached before the repumping procedure starts.

$I_{\text{cool}} / I_{\text{sat}}$	23
$I_{\text{rep}} / I_{\text{sat}}$	3
beam waist (cm)	0.5
sideband : carrier	0.13
detuning cool. (Γ)	$+7.2$
detuning rep. (Γ)	$+7.2$
comp. current I_x (A)	1.50
comp. current I_y (A)	0.80
comp. current I_z (A)	0.15
comp. field B_x (G)	1.14(3)
comp. field B_y (G)	1.18(6)
comp. field B_z (G)	0.48(2)
T_0 (μK)	72(1)
phase space density	$5 \cdot 10^{-6}$

Chapter 4

Evaporation in an optical dipole trap

The scattering properties of a fermionic gas of ^{6}Li atoms [62] can be exploited such that evaporative cooling at high magnetic offset fields in an initially deep optical dipole potential leads to a Bose-Einstein condensation of weakly bound but strongly interacting molecular dimers (mBEC) [100–102].
Such a Bose-Einstein condensate with its properties is well-suited for the adjustment of optical lattices (see Chapter 5). In our experimental setup, we are able to provide homogeneous magnetic fields of up to $\sim 1180\,\mathrm{G}$ using the Feshbach coils (see Chapter 2 and [76]). The deep dipole potential is given by a focused 100 W laser beam at $1070(3)\,\mathrm{nm}$.
This chapter traces our road to a mBEC by implementing forced evaporation of a ^{6}Li gas with strong repulsive scattering length via depth reduction of the all-optical trap by motorized waveplate rotation. It further reports on possible experimental sequences for trap frequency measurements.
In main responsibility of the author the presented results were elaborated. Contributions were mainly given by Michael Hagemann and B. S. Rem and by the Master student M. S. Fischer [103].

4.1 Forced evaporation via waveplate rotation

An all-optical evaporation of a gas can be forced by reducing the potential depth of its trap and so the laser[1] power. Internally the laser power can be controlled from $P_{\mathrm{max}} = 100\,\mathrm{W}$ to $\sim 4\,\mathrm{W} \mathrel{\hat{=}} 4\,\%$. Since this is not sufficient for the purpose of producing a BEC, we need to build an external power ramping unit.
During this PhD thesis we realized that when dealing with near infrared laser intensities of $\gtrsim 10\,\mathrm{MW/m^2}$ it turns out to be essential to minimize the amount of optical elements the light is traveling through. The reasons are lengthy beam paths, issues on dust burning on glass, unwanted but considerable reflections and thermal lensing effects. Therefore and because of the thermal instabilities due to RF power, we circumvent acousto-optic modulators for evaporation and decide to make use of a combination of Glan-Laser polarizers[2] and a half-wave plate[3] instead (see Figure 4.1).
In our setup, a first polarizer cleans the output polarization of the laser and is essential to reach an extinction ratio of $\lesssim 10^{-5}$ (see Figure 4.3 and [103]). The following

[1] IPG Photonics – YLR-100-LP-AC
[2] Thorlabs – GL15-C26
[3] Thorlabs – WPH10M-1064

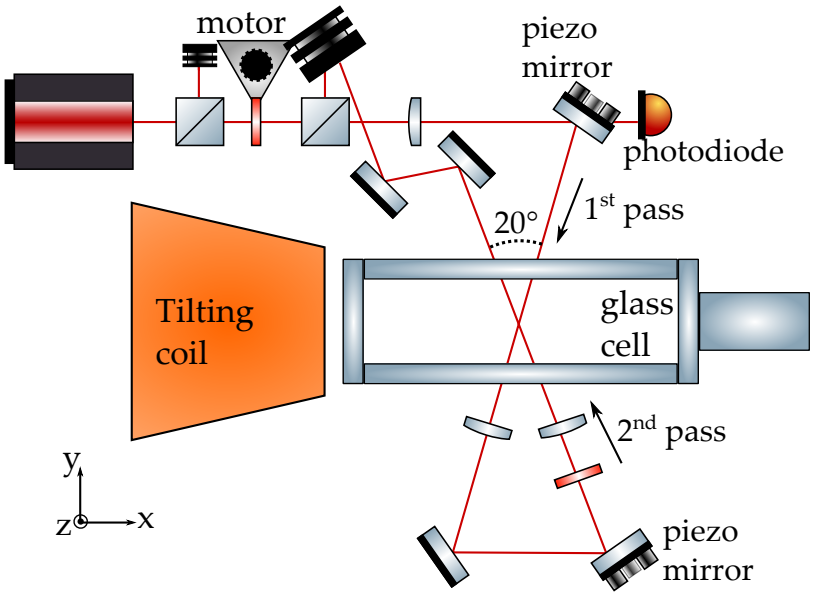

FIGURE 4.1: Sketch of the dipole trap setup – Behind a polarization cleaning of the laser output, a half waveplate in a motorized rotation mount and a polarizer act as a continously adjustable track switch for the laser power and so the trap depth. A photodiode can be used for monitoring and calibration purposes. The piezo mirrors are appropriate for the precise adjustment between the first and the second pass through the cell. As a design library for drawing optics components the author used [104].

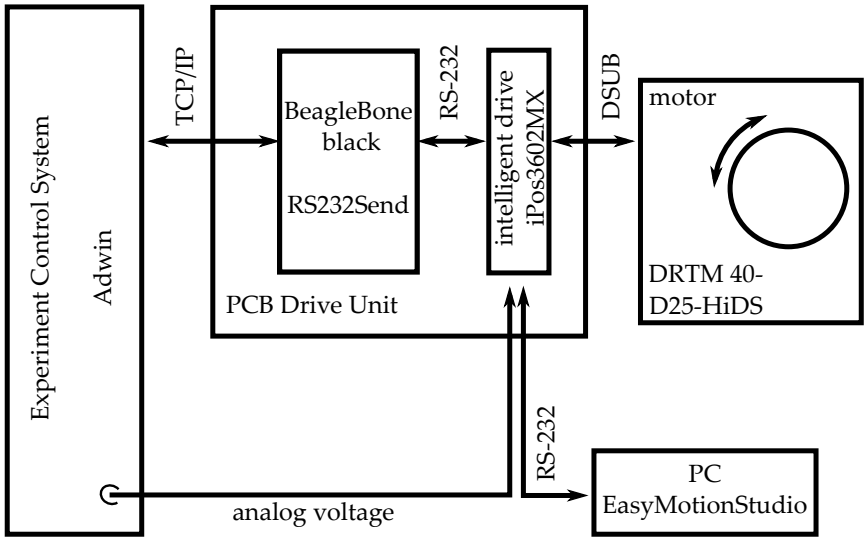

FIGURE 4.2: Connection scheme for the rotation mount – The motor is connected via a DSUB cable to the drive. It can be accessed via an RS-232 connection. For calibration purposes we can connect a PC. During an experimental sequence the BeagleBone black is interposed and can be directly addressed from the experimental control system via TCP/IP. For driving arbitrary power ramps the drive compares the angle position of the motor with an analog voltage coming directly from the experimental control system (see Chapter 2.7). This comparison needs to be calibrated on different levels in order to fulfill our needs as explained in the text.

waveplate placed in a motorized rotation mount[4] and another polarizer are used to adjust the trap depth. Here, the motor of the rotation mount needs a drive unit that

[4]OWIS – DRTM 40-D25-HiDS

links it to our experimental control system (see Figure 4.2).
Such a drive unit has to fulfill the requirement of a small jitter[5] and a high reproducibility of an exponential ramp as it is our approach for forced evaporation (see Chapter 4.2). Since the included drive of the motor did not meet these requirements [105], we realized a self-built interface based on the iPOS3602 MX intelligent drive from TECHNOSOFT in combination with a BeagleBone black (see Figure 4.2). In this way, we minimze the jitter to $\sigma_\tau = 360\,\mu$s [106].
For performing smooth ramps, the PID parameters of the drive's position controller need to be adjusted correctly to the characteristic timescales of the user defined ramps. Therefore a direct RS-232 interface to a PC is established. Here, the included software EASYMOTION STUDIO communicates with the drive. We further use this interface to program that the drive changes the orientation angle of the waveplate proportional to an analog voltage of the experimental control system ADwin (see Chapter 2.7). The conversion from a voltage to a specific laser power is calibrated via a photodiode in transmission of a high reflective mirror and the obtained data are fed into the experimental protocol. Once this is done the angle of the waveplate can be changed smoothly.
Though, the incremental encoder of the drive is relative and so the optimal reproducibility of a ramp is granted if the drive finds the absolute motor position in each experimental run. For this finding procedure called "homing" the drive stops listening to the analog voltage. In order to start "homing" or to tell the drive to listen to the analog voltage we send commands via a TCP/IP connection to the BeagleBone black in every experimental cycle. On this small single-board computer we run a program that converts our commands and sends them via RS-232 to the drive. All in all, an analysis of the used exponential power ramp [103] reveals a relative standard deviation of $\sigma = 0.86\,\%$ for the final trap depth.
With the described technique we routinely produce a molecular BEC (see Chapter 4.2) and minimize thermal lensing up to an inevitable effect that is induced by the glass cell walls. It concerns an instantaneous shift of the waist position along the propagation axis. Since the geometry of the cell is optimized for high-NA imaging and minimum wall binding, the distance of the wall to the atoms is around half of the Rayleigh length of the foscused dipole trap beam and the wall thickness of 5 mm enhances this issue. Nevertheless, by a careful adjustment of the focusing lens for the second pass and by using the two piezo mirrors[6] (see Figure 4.1), we can find a reproducible evaporation procedure and final trap geometry for the mBEC.

[5] We define the jitter to be the standard deviation of a delay time τ.
[6] Radiant-Dyes – MDI-HS-2-3025-M6

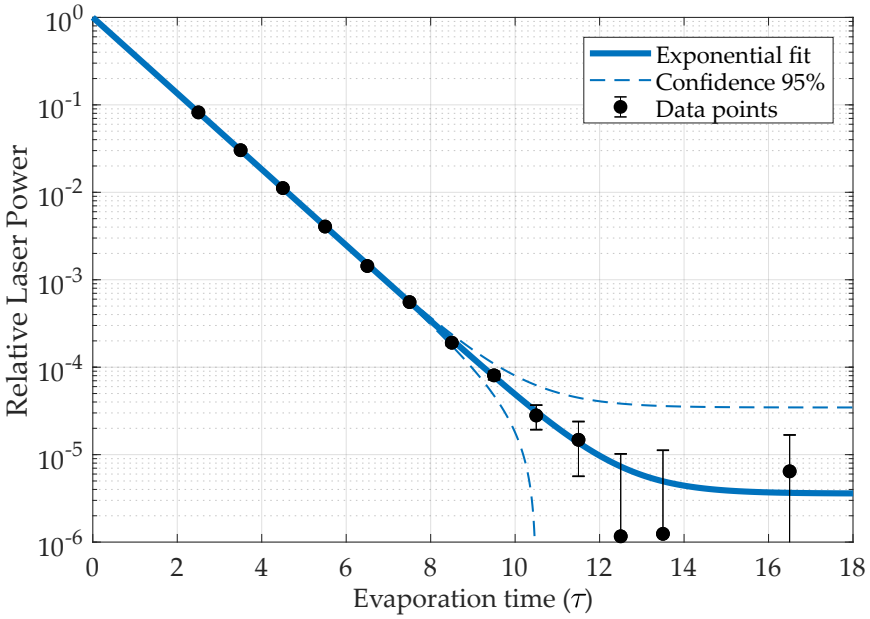

FIGURE 4.3: Characterization of the extinction ratio for the dipole trap – For testing the minimum possible power we can reach, we program an exponential ramp $\propto \exp(-t/\tau)$ for our waveplate in a motorized rotation mount and measure the voltage on a photodiode behind a PBS for different values of t. We then fit (blue line) an exponential $\exp(-t/\tau) + \epsilon$ to the data of relative laser power (black data points) and call $\epsilon = (0.4 \pm 3.0) \cdot 10^{-5}$ the extinction ratio. Here, the error is the 95 % fit confidence error that is also indicated by the dashed blue lines. It mainly originates from the signal-to-noise ratio of the photodiode.

4.2 The route to the mBEC

In the following the author reports on an experimental sequence for an all-optical evaporative cooling of fermionic ^{6}Li atoms that finally evokes a phase transition of the gas to a molecular BEC as it had been observed e.g. by [100–102].
For loading the atoms into the deep optical potential of the dipole trap, we switch on the 100 W by using the fast TTL modulation input[7] of the laser 0.5 s before the MOT loading is completed. We rotate the waveplate linearly within 200 ms by 45 ° to shine the full power onto the atoms and then perform the steps of MOT compression and gray molasses cooling.
In order to image the ultracold gas during its time-of-flight (ToF) at high magnetic fields, the optical dipole trap is adjusted to the center of the residual curvature of the homogeneous magnetic field produced by the outer Feshbach coils. Since this position does not coincide with the center of the MOT, we need to slightly shift the atoms to the dipole trap. Therefore, an additional magnetic field is applied along the push beam axis during the MOT compression by switching on the Tilt coil (see Chapter 2). For gray molasses cooling the current through all coils except the compensation coils' current is switched off again. Other parameters described in Chapter 3 remain valid for optimal loading into the dipole trap. This is reasonable because the laser wavelength is in a magic[8] regime for the used transitions [107].
As mentioned in Chapter 3, when completing gray molasses cooling $\sim$ 3 % of the atoms are trapped in the dipole potential which is then kept on at maximum depth

[7] The fast modulation input of the IPG Photonics YLR-100-LP-AC switches the laser on and off within $\sim 8\,\mu$s [103].

[8] Magic means in this context that the polarizability of the atom in a laser field of the given wavelength is the same for the ground state as well as for the excited state of a transition.

for another 10 ms. During the last 5 ms of this plain evaporation we ramp up the homogeneous magnetic field linearly to 810 G. This value is chosen for exploiting the large value of the scattering length $a > 6\,000\,a_0$ close to the broad Feshbach resonance (see Figure C.1) at 832.18(8) G between the Paschen-Back states[9] $|1\rangle$ and $|2\rangle$ into which the atoms of the $|F = 1/2\rangle$ ground state are adiabatically loaded [108, 109].
In order to force the evaporation, the trap depth is lowered by ramping down the laser intensity $I \propto \exp(-t/\tau)$ (see Chapter 4.1), i.e. the duration t in units of τ fixes the relative trap depth. A change of τ changes the ramping speed. It is therefore a measure for the thermalization time of the gas. The large absolute value of the scattering length a at 810 G reduces this thermalization time. For our experiments τ is minimized to $\tau = 0.7$ s in order to have a short experimental sequence.
In the specific case of a fermionic $|1\rangle$ – $|2\rangle$ mixture on the repulsive side of the Feshbach resonance, the atoms can undergo a transition from an unbound to a bound state and become bosonic molecules [100–102, 110]. Having an equal distribution of states in the mixture, the number of molecules N_{mol} may reach a temperature dependent equilibrium with

$$N_{\mathrm{mol}} = \frac{N_{\mathrm{at}}}{2} \cdot \left[1 + \frac{1}{\Phi_{\mathrm{at}}}\, e^{E_b/k_B T}\right]^{-1} \tag{4.1}$$

with N_{at} being the total number of atoms, Φ_{at} their phase space density and the binding energy [62, 111]

$$E_b = -\frac{\hbar^2\, a}{m_{\mathrm{Li}}\, |a|^3}. \tag{4.2}$$

After an evaporation time $t = 4.2$ s we reach a temperature of ~ 150 nK and an atomic phase space density of

$$\Phi_{\mathrm{at}} = \frac{N_{\mathrm{at}}}{V} \cdot \Lambda^3 = \frac{N_{\mathrm{at}}}{\sigma_z \sigma_r^2} \cdot \left[\frac{2\hbar^2}{m_{\mathrm{Li}}\, k_B\, T}\right]^{3/2} \sim 4.8 \tag{4.3}$$

with $N_{\mathrm{at}} \sim 1.2 \times 10^5$, $\sigma_z \sigma_r^2 \sim 2.8 \times 10^{-14}\,\mathrm{m}^3$, $V = (\pi)^{3/2}\, \sigma_z \sigma_r^2$ being the cloud volume and Λ being the thermal de Broglie wavelength. For this case almost all atoms should be bound to molecules and their phase space density can be approximated by $\Phi_{\mathrm{mol}} \approx 2^{-\frac{5}{2}}\, \Phi_{\mathrm{at}} \sim 0.8$.
When the particles are further evaporatively cooled, we observe the emergence of a molecular BEC (see Figure 4.4). The purity of the mBEC can be analyzed by its condensed fraction. Therefore, like in [112], we assume a Bose-enhanced Gaussian distribution for all thermal particles and add a strongly interacting BEC in the Thomas-Fermi limit. We integrate along the imaging axis and obtain our 2D-fit function[10]

$$\tilde{n}\,(x,y) = \tilde{n}_{\mathrm{th}}\,(x,y) + \tilde{n}_{\mathrm{c}}\,(x,y) \tag{4.4}$$

$$= \frac{\tilde{n}_{\mathrm{o,th}}}{g_2\,(1)}\, g_2\left[e^{-x^2/x_{\mathrm{o,th}}^2 - y^2/y_{\mathrm{o,th}}^2}\right] + \tilde{n}_{\mathrm{o,c}}\, \mathfrak{Re}\left[\left(1 - \frac{x^2}{x_{\mathrm{o,c}}^2} - \frac{y^2}{y_{\mathrm{o,c}}^2}\right)^{3/2}\right] \tag{4.5}$$

[9] A level diagram showing the level splitting in magnetic offset fields for ^{6}Li can be found in Figure B.2.
[10] We fit this function to absorption images.

for the column density $\tilde{n}(x,y)$ with the peak column densities $\tilde{n}_{\mathrm{o,th}}$ and $\tilde{n}_{\mathrm{o,c}}$. The condensed fraction is given by

$$r_{\mathrm{c}} = \iint \frac{\tilde{n}_{\mathrm{c}}(x,y)}{\tilde{n}(x,y)} \quad d(x,y) \tag{4.6}$$

$$= \left(1 + \frac{5\,\zeta(3)}{2\,g_2(1)} \frac{x_{\mathrm{o,th}}\, y_{\mathrm{o,th}}\, \tilde{n}_{\mathrm{o,th}}}{x_{\mathrm{o,c}}\, y_{\mathrm{o,c}}\, \tilde{n}_{\mathrm{o,c}}}\right)^{-1}, \tag{4.7}$$

where $\zeta(s)$ calls the Riemann function and $g_2(s)$ is the dilogarithm.

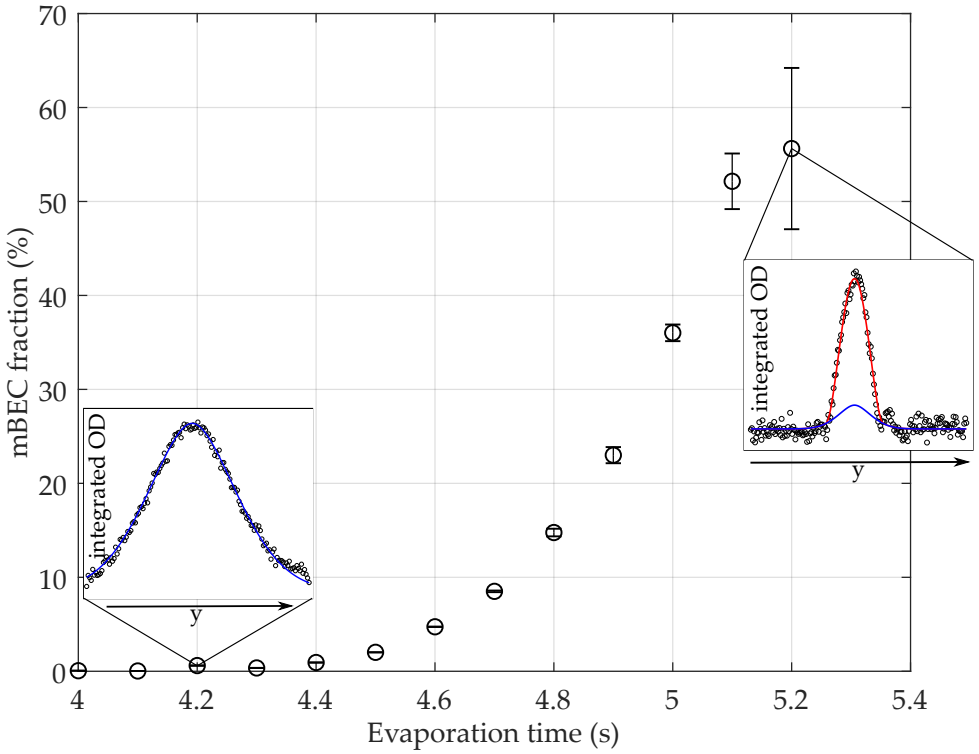

FIGURE 4.4: Emergence of the molecular BEC – the condensed fraction r_c of the molecular BEC is plotted versus the evaporation time t meaning that the laser power is reduced $\propto \exp(-t/\tau)$. The inlets show examples of column sums on analyzed absorption images. Here, the integrated OD for each column is given in black circles. The red line plot $\int \tilde{n}(x,y)\,dx$ and the blue line $\int \tilde{n}_{\mathrm{th}}(x,y)\,dx$ indicate the quality of the 2D-fit.

At an evaporation time $t = 5.2\,\mathrm{s}$ the final condensate fraction is fitted to $55(9)\,\%$. A Monte-Carlo simulation for a molecular BEC on resonance predicts a condensate fraction of $57(2)\,\%$ [113, 114]. The strong interactions in the cloud lead to a decreasing occupation of the zero momentum state and higher states are populated. Thus, we may claim that our condensate fraction is mainly limited by those interactions. When the particles are held in the remaining trap at the end of our evaporation the characteristic lifetime is on the order of 1 minute [103]. This confirms again, like in Chapter 3, that future experiments will not be limited due to collisions with hot residual background atoms.

4.3 Measuring trap frequencies

The measurement of trap frequencies is an important tool when dealing with ultracold gases in dipole traps. It reveals insights about the possible losses due to parametric heating and about the adjustment of the beams including their waist and power when comparing the frequencies to a calculation of a derived trapping potential. Like stated e.g. in [115] the atoms that are weakly bound to molecules have in good approximation the same ground state polarizability α given in [107]. So in principle the trapping potential $V_o(\vec{r})$ can be calculated from the intensity distribution $I(\vec{r})$ via

$$V_o(\vec{r}) = -\kappa \cdot I(\vec{r}) \tag{4.8}$$

with $\kappa = 6.06 \cdot 10^{-8}\,\mu\mathrm{K\,m^2/W}$ for the atomic ground state at a laser wavelength of 1070 nm.
Experimentally, we observe however that the focus positions of the two dipole trap beams is changing as a function of laser power during forced evaporation. We interpret such a dynamical effect as coming from thermal lenses on the glass cell walls as stated in Chapter 4.1. It makes it unfavorable to compare the trap geometry with a calculation of a usual static case with fixed focus position.
Nevertheless, by taking absorption images at different steps during evaporation, we can reveal the dynamics that are present during forced evaporation. For our specific case, we tune our dipole trap geometry such that the beam that first passes the atoms (first pass) has a slightly larger waist $\omega_1 = 110(2)\,\mu$m than the recycled beam (second pass) $\omega_1 = 92(1)\,\mu$m. Hence, because of its larger trap volume the first pass plays a major role when loading the atoms from a gray molasses into the dipole trap. On the other hand, the second pass provides a slightly deeper trap. When now the focus positions of both beams start to move during forced evaporation, we observe for a given adjustment that all atoms move to the slightly deeper trap of the second pass. The data of a radial and longitudinal trap frequency measurement for such a scenario is shown in Figure 4.5. The experimental sequences for that measurements are explained in the following.
They both start with producing a mBEC like in Chapter 4.2. When evaporation is completed, we ramp the magnetic field from 810 G to 690 G to lower the scattering rate inside the ultracold cloud. Simultaneously, the laser power is ramped back to $\sim$ 1 W in 50 ms. For this power value no effects of thermal lensing are expected. The radial excitation is then realized by shortly switching on the MOT coils in anti-Helmholtz configuration with the same gradient as for the MOT (see Chapter 3). The longitudinal excitation can be created via an amplitude modulation of the trap. Here, we modulate near to the trap frequency from 1 W down to 0.04 W for 5 periods by using the analog input of the laser source[11]. For both types of excitation, we further hold the atoms in the trap for a certain time before we perform 2 ms ToF and image the cloud at an offset field of 690 G (see Chapter 6.2). When stepping adequately through the holding time the gas is found at different vertical or respectively horizontal positions. By plotting the positions versus the holding time we can find a sinusoidal dependance that reveals the trap frequency.

[11] The analog input of the YLR-100-LP-AC has a bandwidth of $\sim$ 10 kHz. In the usual experimental runs it is better not used because it adds extra noise to the laser [103].

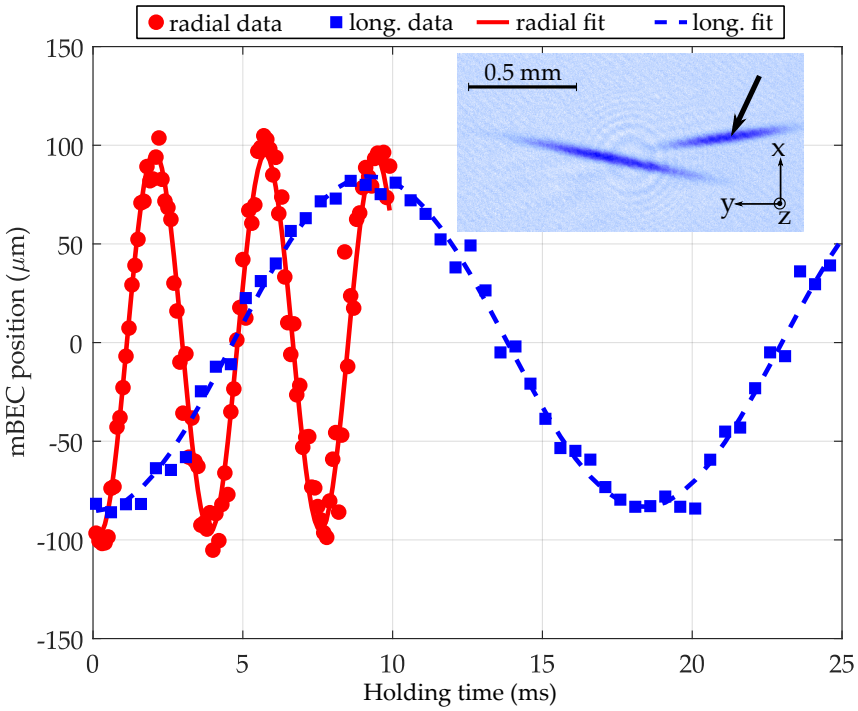

FIGURE 4.5: Measurement of trap frequencies of the optical dipole trap geometry at 1 W – The inlet shows an absorption image at an intermediate time step of forced evaporation closely before the clouds in the two trapping beams merge. The black arrow points on the atoms in the second pass optical dipole trap. This trap is slightly deeper. The measured data points are for the case where all atoms are mainly trapped by the second pass laser beam. They are taken from another imaging direction than the inlet and show the position along the z-direction (red) and along the y-direction (blue) of the mBEC after 2 ms ToF for different holding times after excitation. In the case of the radial oscillation (red circles) we switch on the MOT coils for 200 μs. For a longitudinal oscillation (blue squares) we perform an amplitude modulation at 45 Hz. The fits (red continuous line and resp. blue dashed line) lead to a radial frequency $\omega_r = 2\pi \times 271(3)$ Hz and a longitudinal frequency $\omega_l = 2\pi \times 54.6(3)$ Hz. The radial frequency fits well to a calculation of a static second pass dipole trap where $\omega_r = 2\pi \times 275(10)$ Hz. The measured value of the longitudinal frequency can be interpreted as coming from a combined trap that consists of a magnetic confinement by the residual curvature field of the Feshbach coils and a dipole trap confinement.

Chapter 5

Optical lattices

An essential part of a quantum gas microscope is its optical lattice configuration for the spatial pinning of the atoms during fluorescence imaging.
After motivating our laser source system, this chapter reports on a vertical one-dimensional optical accordion for the creation of a two-dimensional atomic gas. Here, we show that we are able to tune dynamically the trap frequency along the lattice direction via a reduction of the lattice constant. Furthermore we report on how we can load a gas completely into a single slice and compress it. In addition, this chapter informs about a horizontal two-dimensional triangular lattice that is aligned onto the atoms. Here, we especially measured the phase noise between the lattice beams as it is one crucial point for a quantum gas microscope.
In main responsibility of the author the presented results were elaborated. Contributions were mainly given by Michael Hagemann and B. S. Rem and by the Master student M. S. Fischer [103].

5.1 The lattice laser source system

The seeder light that is amplified for all lattice beams is provided by a low noise DFB fiber laser[1] with 10 mW output power and a spectral width < 10 kHz. Its wavelength of 1069.8 nm can be temperature-adjusted within a range of 0.7 nm to be magic[2] for the $2s$–$3p_{1/2}$ transition that has its resonance at 323.36 nm [107]. Considering possibilities for cooling the atoms in the optical lattice, we chose that transition for the following reasons:

- At this wavelength there is only a slight shift between the magic wavelengths for ^{6}Li and ^{7}Li that is within the errorbars of [107].
- For the $2s$–$3p_{3/2}$ transition, used for a UV-MOT [74, 116], the magic wavelength depends on the value $|m_j|$ and splits into two wavelengths that are $\sim \pm 1$ nm away from the chosen wavelength [107].
- We do not expect any significant change concerning Raman sideband cooling with detuning to the standard D lines [20, 21, 63] when going from 1064 nm to the chosen wavelength.
- The $2s$–$3p_{1/2}$ transition is the candidate transition to test a UV gray molasses cooling in a lattice.

[1] NKT photonics: Koheras ADJUSTIK POWER Y10
[2] Magic means in this context that the polarizability of the atom in a laser field of the given wavelength is the same for the ground state as well as for the excited state of a transition.

As an amplification system for the laser we decide for a two stage amplification from AZUR LIGHT SYSTEMS. A first preamplifier stage has an output of 250 mW. Its power is split into 4 different fibers for further amplification purposes. For this thesis, only two output fibers are used in separate high power amplification stages that output each ~ 40 W.

5.2 1D optical accordion for z-confinement

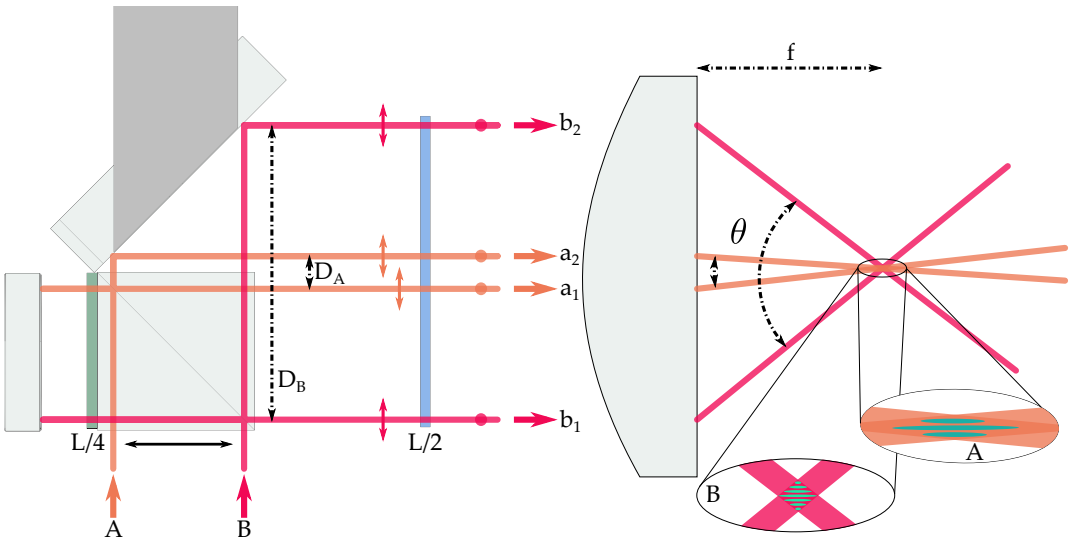

FIGURE 5.1: Sketch of the principle for the optical accordion – The sketch shows a beam path for small θ (A: orange) and a large θ (B: purple). Between both paths the input position of the beam on the PBS is translated. With the given geometry this results in a change of the lattice spacing a_{latt} and so the trapping frequency $\omega_z \propto a_{\text{latt}}^{-1}$. In order to make sure that we have a full modulation depth of the interference for every angle θ we added a rectangular $L/2$ waveplate to the splitting optics on the left side of the sketch. Additionally, we can separately and precisely tilt the two mirrors behind the PBS for a fine tuning of the beam angles.

Our experimental apparatus aims for quantum gas microscopy (see Chapter 1). With this technique we resolve clear images when all fluorescing atoms are confined to $\lesssim 2.7\,\mu$m (see Table 6.1) and become a two-dimensional gas. In matters of ultracold gases, reduced dimensionality is reached when all intrinsic energy scales of the gas are $\ll \hbar\omega_z$ where ω_z is the trap frequency in the squeezed direction.
In our case ω_z is the trap frequency of a pancake-shaped single slice of a 1D lattice in the direction of the lattice vector. The lattice is a so-called optical accordion [81, 82, 117] as it is formed by two laser beams crossing at a dynamically tunable full intersection angle θ. Thus, it is not only possible to tune ω_z by changing the laser power P with $\omega_z \propto \sqrt{P}$ but also by tuning θ as $\omega_z \propto \sin(\theta/2) \sim \theta/2$.
A reasonable approach to load all atoms into a single lattice slice is to first chose θ as small as possible while ramping up the laser power P. For this case the lattice spacing

$$a_{\text{latt}} = \frac{\lambda}{2\,\sin(\theta/2)}, \tag{5.1}$$

with λ being the laser wavelength, is large such that the trapping volume for a single slice has a large overlap with the optical dipole trap (see Chapter 4.1). In a second

step θ is dynamically increased and the optical accordion is compressed. This leads especially to an increase of ω_z such that in the adiabatic limit the motion along the lattice vector is frozen out.

5.2.1 Technical implementation

Technically we realize our optical lattice by shining two laser beams on a single lens with a focal length f (see Figure 5.1). In front of that lens the laser beams are collimated and propagate equidistantly above and below the central lens axis. By changing the distance D between the two beams their intersection angle is changed as

$$\tan(\theta/2) = \frac{D}{2f}. \tag{5.2}$$

For a stable interference and so a stable trap position along the z-axis the optical path difference between the two intersecting beams of the accordion must be as constant as possible. Therefore, we split the laser beam directly in front of the aspheric lens via a PBS[3].
The translation of the input beam is realized by a motorized translation stage[4] that is implemented in the laser setup below the PBS (see Figure 5.2). It can be interfaced like the rotation mount in Chapter 4 via the RS232Send program on a BeagleBone black that is connected to the experimental control system. An advantage in the case of the translation stage is its commercial motor controller[5] with a timing jitter of $\sim 400\,\mu$s [103]. This value is similar to the one of the IPOS3602 MX such that we do not need to implement and calibrate it for the stage.
The intensity control of the optical accordion is similar to the case of the optical dipole trap a combination of a motorized rotation mount and a Glan-Laser polarizer (see Chapter 4.1).

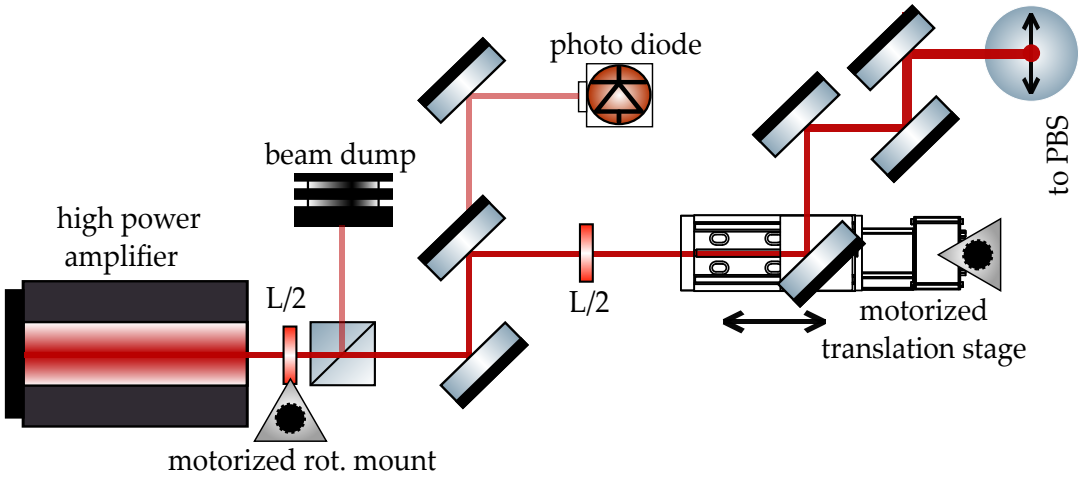

FIGURE 5.2: Sketch of the setup below the splitting cube – The intensity control unit consists of a $L/2$ waveplate in a motorized rotation mount, a Glan-Laser polarizer and a photodiode behind an HR mirror. Another $L/2$ waveplate is used to adjust the power in the separated intersecting beams. The motorized translation stage is used to shift the beam position on the PBS.

[3] B. Halle: BHN 2016.0077.0003, the PBS is coated with a $L/4$ waveplate at one side.
[4] Zaber: ZAB-LSQ075D-E01T3-MC03
[5] Zaber: ZAB-X-MCB1-KX13B

In order to keep the atoms at a fixed position while squeezing the trap, it is important to minimize spherical aberrations for the intersecting beams. On account of this we followed the recommendation of [81] and bought a fused silica aspheric lens AFL50-80-S-C from ASPHERICON and placed it on a small XYZ translation stage[6] for adjustment purposes (see Figure 5.3). Its effective focal length for 1068.9 nm is calculated to be 87.6 mm by using OPTICSTUDIO from ZEMAX and measured to be 87.5(4) mm [103]. The size of the lens is shaped at the institute via a milling machine that is kindly provided and operated by O.Hellmig. For our needs we decide for a rectangular form:

- Along the horizontal direction the width is shaped to 12.4 mm. As we can better separate the beams at larger distances we do not want the optical dipole trap beams to propagate through the lens.
- Along the vertical direction the width is shaped to 46.7 mm since we want the tuning range for θ to be as large as possible. Experimentally we reach $\theta_{\text{max}} \sim 30\,^\circ$ that is in good agreement with Equation 5.2.

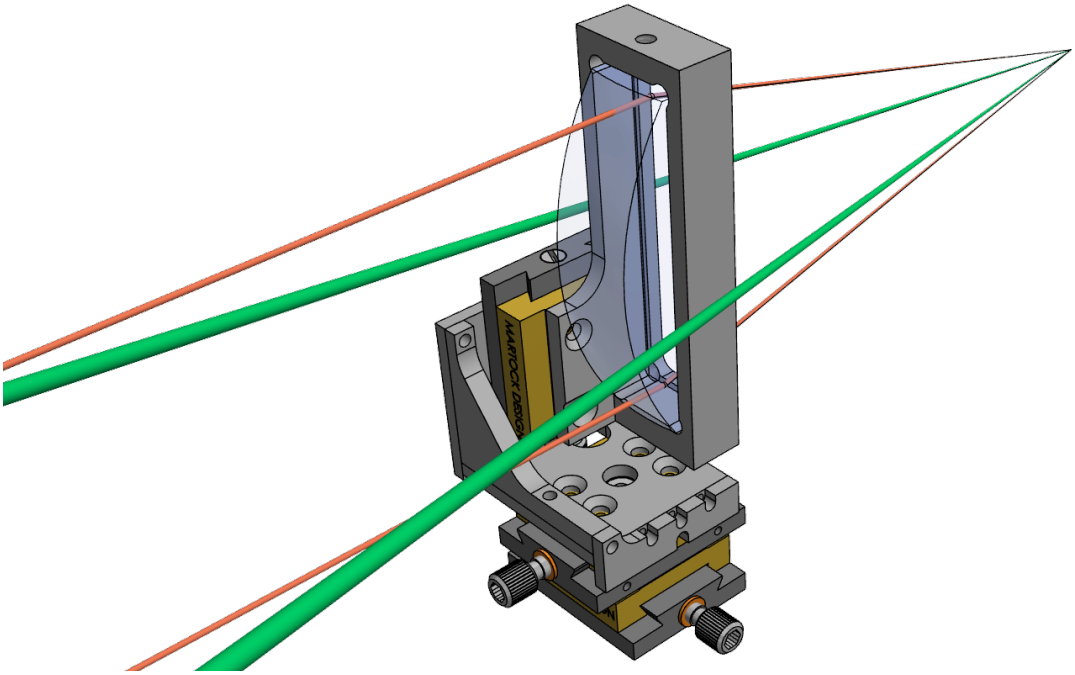

FIGURE 5.3: Sketch of the aspheric lens for the optical accordion and its adjustment stage – The beams of the optical dipole trap (large green beams) pass horizontally by the lens at $\pm 10\,^\circ$. The beams for the accordion (smaller orange beams) propagate through the lens on different vertical positions. All beams need to be adjusted on the same point where the atoms are manipulated.

[6] Elliot Scientific: MDE261 and MDE262

5.2.2 Adjusting the optical accordion

The maximum trap depth at full power[7] for a single beam of the optical accordion is at $\sim 340\,\mu$K. Since that depth is a factor of ~ 4 larger than the final temperature of our gray molasses cooling (see Chapter 3), we observe an increase of atomic density in the beams of the accordion lattice when they are loaded like the optical dipole trap (see Chapter 4 and Figure 5.5 (a)). As a consequence this loading can be used for measuring their intersection angle θ as it is described in the next subsection, but also for a fine adjustment. Here, the goal is to adjust the intersection of the two lattice beams to the focal plane of the aspheric lens.
By stepping through the translation of the PBS input beam (see Figure 5.1 and 5.2), we can identify separately for both beams a point in the atomic cloud that is always hit by a lattice beam, meaning that the lattice beam rotates around this point. This so-called "pivot point" has the property to be fixed on the focal plane of the aspheric lens (see Figure 5.4). Within the plane its position is tunable by carefully tilting the mirrors behind the PBS (see Figure 5.1). In this way, we adjust the beams onto each other such that they intersect at their "pivot points" in the focal plane of the aspheric lens.
Since the used absorption imaging setup is overlapped with a 3D-MOT beam (see Chapter 6.2 and Figure 3.1), we see a 45°-projection of the focal plane that needs to be taken into account when measuring the intersection angle θ. We further check that the angle bisector of θ is aligned horizontally.
In a further step, we perform absorption imaging of the mBEC via the same imaging path and overlap the position of the mBEC with the intersection of the lattice beams via an iterative adjustment of the XYZ stage of the lens holder and the mirrors behind the PBS (see Figure 5.3 and 5.1).

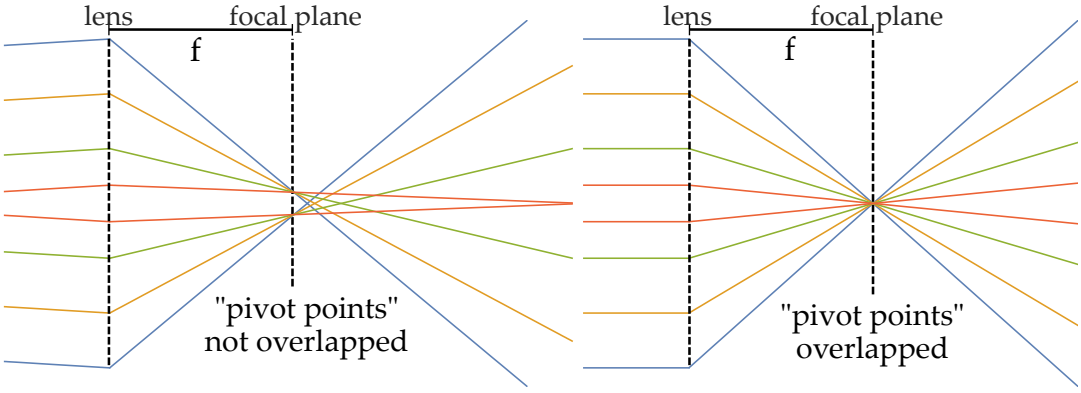

FIGURE 5.4: Sketch of the lattice beams refracted by the aspheric lens – The path of the beams is shown for different distances between them at the lens position and is color-coded. The left sketch shows a case where the "pivot points" are not overlapped and the intersection is not spatially fixed when the distance between the beams at the lens is changed. The right sketch shows the ideal alignment. For simplicity the sketched plane is chosen perpendicular to the focal plane.

[7] $P_{\max} \sim 20\,\mathrm{W/beam}$

5.2.3 Measuring the lattice spacing

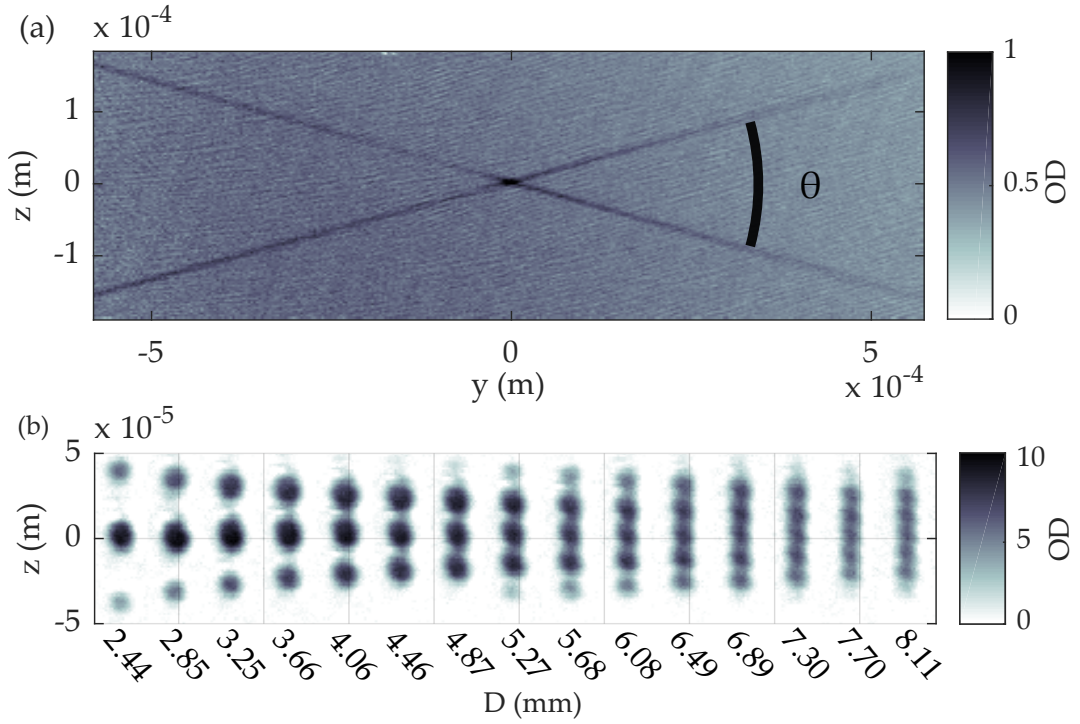

FIGURE 5.5: (a) Absorption image 10 ms after switching off gray molasses cooling when the lattice beams of the accordion are each at $\sim$ 20 W – The path of the beams is clearly visible due to an increase of optical density, meaning that atoms are loaded into the beams. As the image is taken under 45 °, the horizontal axis of the image needs to be stretched by $1/\cos(\pi/4)$ before the intersection angle θ between the beams can be extracted. In the example shown here, $\theta = \theta_{\text{max}} \sim 30\,^\circ$. (b) In situ absorption images of an ultracold gas trapped in the accordion lattice – The images are taken in the x-z plane. From left to right, the distance D of the accordion beams on the aspheric lens is increased. This results in a smaller lattice spacing a_{latt}. Considering the overlap with the optical dipole trap, the smaller the spacing the more slices of the lattice are filled. For the data shown here the read out error of D is estimated to 60 μm and the magnification of the image is known up to 2 %.

Like in [81], we characterize the tunability of the accordion lattice by measuring the lattice spacing a_{latt} versus the distance D between the lattice beams in front of the aspheric lens. From the Equations 5.1 and 5.2, we get

$$a_{\text{latt}} = \frac{\lambda}{2}\sqrt{1+4\left(\frac{f}{D}\right)^2}, \tag{5.3}$$

with $\lambda = 1069.8\,\text{nm}$ and $f = 87.6\,\text{mm}$.
Since we have no optical element in our laser setup that can switch off the laser beams quickly enough (see Figure 5.2), we are not able to perform ToF measurements where atoms from different lattice slices can interfere nor to use Kapitza-Dirac diffraction like in [118]. However, after calibrating the position of the translation stage to the values of D, we find ways to measure the lattice spacing a_{latt} with our cold gas:

1. We can use a loading from a gray molasses as it is described in the last subsection in order to measure the intersection angle θ (see Figure 5.5 (a)) and extract a_{latt} indirectly by using Equation 5.1.

2. We evaporate like it is explained in Chapter 4, but in addition to the optical dipole trap we perform the same power ramp for the accordion lattice beams. For the absorption images shown in Figure 5.5 (b) the evaporation time is $8.5\,\tau = 5.95\,\mathrm{s}$. The imaging is performed along the y-axis that is the common propagation axis of the accordion lattice beams (see Figure 2.9 and Figure 6.6b).

3. We can image the ultracold gas along the push beam axis (x-axis, see Figure 6.6b) where we could[8] reach a higher resolution. In this case we use again a different experimental sequence. We first produce a mBEC like in Chapter 4 and then recompress it by slightly increasing again the power in the beams of the optical dipole trap before ramping up the accordion lattice. In this way, we have more control over the number of slices we want to load and it is possible to even load a single lattice slice (see Figure 5.7).

All measurement data for a_{latt} measured via the different approaches are combined in Figure 5.6. They especially show that we can realize lattice spacings from $45(1)\ \mu$m to $2.07(3)\ \mu$m.
Considering the measured range of the lattice spacing and the single beam waist at the focus position that is $w_o = 47.8(5)\ \mu$m [103], we can derive from Equation 4.8 the potential created by the lattice. The main properties are summarized in Table 5.1.

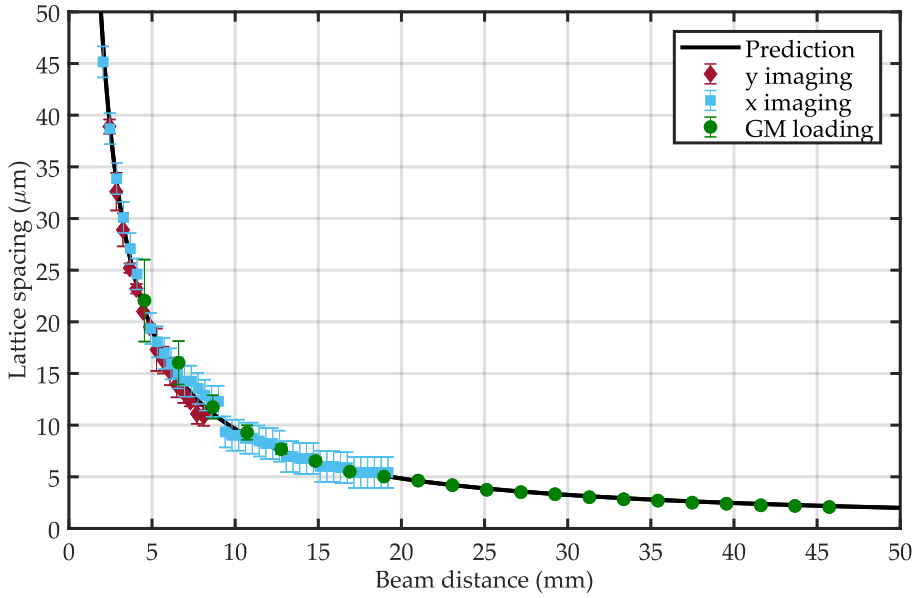

FIGURE 5.6: Measuring the lattice spacing – Three different data sets are compared to the predicted relation (black line) between the beam distance on the lens and the lattice spacing on the atoms that is given by Equation 5.3. For gray molasses loading (green circles) the intersection angle θ is measured and converted into a lattice spacing giving small error bars for small spacings. For large spacings direct absorption imaging is possible from two directions: along the common propagation axis of the lattice beams (red diamonds) and in the direction that is orthogonal to the propagation axis and the lattice vector (blue squares).

TABLE 5.1: Main properties of the accordion lattice – D is the distance between the lattice beams at the lens, a_{latt} is the lattice spacing in the intersection region of the beams, θ is the full intersection angle between the lattice beams, ω_{xyz} are the trap frequencies for a single slice at the intersection center, V_o is the maximum trap depth of the lattice. ω_{xyz} and V_o are estimated for the case of a maximum laser power of 20 W per beam.

	decompressed	**compressed**
D (mm)	2.05(6)	45.73(6)
a_{latt} (μm)	45(1)	2.07(3)
θ (°)	1.36(3)	29.9(5)
$\omega_x/2\pi$ (kHz)	9	9
$\omega_y/2\pi$ (kHz)	0.13	2.4
$\omega_z/2\pi$ (kHz)	23	460
V_o (mK)	−1.36	−1.36

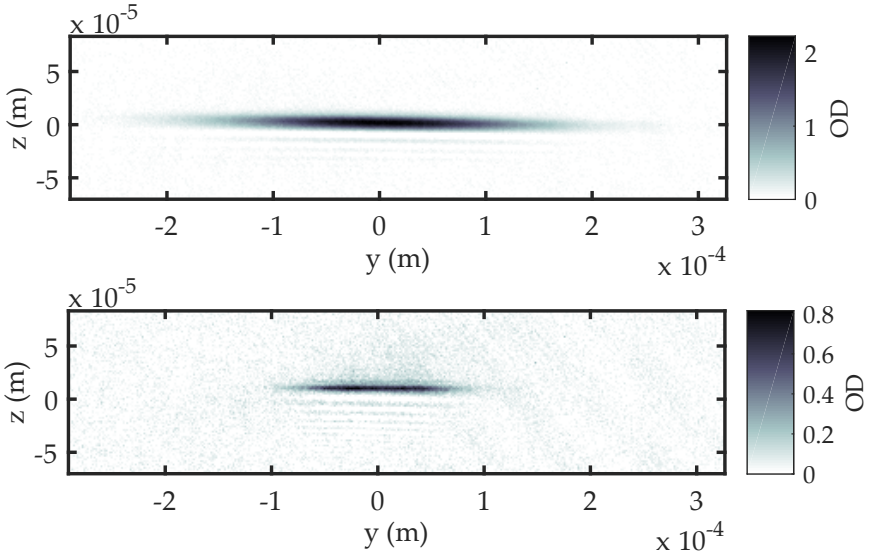

FIGURE 5.7: Absorption images of atoms in the accordion lattice potential for the uncompressed and the compressed case along the x-axis – (a) In an uncompressed lattice the spacing is 45(1) μm and we can load our gas into a single slice. (b) In the compressed lattice the spacing is 2.07(3) μm that is below the resolution limit of the imaging setup. The shift of the cloud in z-direction during compression is $\sim 8\,\mu$m that is $\sim 15\,\%$ of the beam waists. The visible fringes in both images are diffraction effects since the laser frequency is not exactly on the absorption maximum of the atomic transition.

5.2.4 Dynamic squeezing of a single lattice slice

Experimentally we realize a dynamic compression of a single lattice slice after aligning the two lattice beams precisely to the aspheric lens and to the position of mBEC. After an evaporation of the cloud that takes $t = 7.2\,\tau$ in the optical dipole trap (see Chapter 4), we squeeze the mBEC within 50 ms by increasing again the laser power of the dipole trap beams to $\sim$ 1 W. Thereafter, we load the atoms into the accordion lattice by increasing the power in the lattice beams to 75 mW/beam. During the loading process that takes 250 ms the lattice spacing is kept at its maximum such that all of the atoms are loaded into the central single slice. Afterwards, the optical

[8] After the installation of the triangular lattice the resolution is reduced now.

dipole trap is switched off and we wait for 100 ms to let the cloud equilibrate before the accordion is compressed by tuning the lattice spacing to its minimum within 112 ms. Before imaging, the lattice depth is further held constant for 388 ms.
Figure 5.7 allows a comparison between the uncompressed and the compressed state of the lattice. The experimental sequence for the two images that is described above differs only by the fact that for the uncompressed case the translation stage remains fixed at a maximum lattice spacing.
As we cannot resolve single slices of the compressed lattice via absorption images along the x-axis ($\lambda/\mathrm{NA} \sim 4\,\mu$m) and due to the fact that ToF measurements are not compatible with the current setup, we cannot be completely sure that all atoms remain in a single slice after compression. Nevertheless, we can perform an additional decompression after compression. Here, we do not observe a measurable amount of atoms that are moved to other lattice slices. Finally, if any atoms tunnel to other slices there will be a clear signature when performing single site fluorescence imaging [119].

5.3 Triangular 2D lattice for pinning

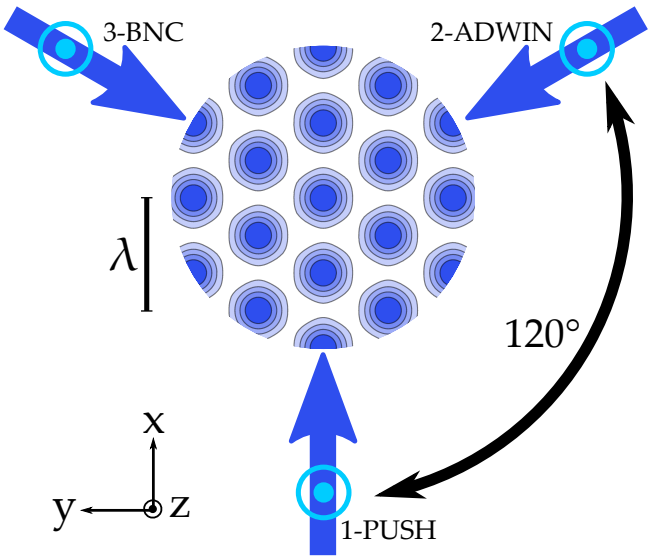

FIGURE 5.8: Horizontal cut through the 2D interference potential of the triangular pinning lattice – The direction of the three laser beams forming the interference is indicated by the blue arrows. They are pairwise separated by 120 °. All three beams are in s-polarization, indicated in light blue. The atoms are trapped in the minima (blue) of the lattice potential. It has a spacing of $a_\Delta = 2\lambda/3$. The beams have "lab names": 1-PUSH, 2-ADWIN, 3-BNC.

Our experiment is designed for pinning the atoms within a horizontal slice in a triangular 2D lattice.
Such a lattice belongs to the family of hexagonal lattices that had been realized experimentally with ultracold atoms in [120]. Since then, they became a powerful playground for state-of-the-art experiments. A similar triangular lattice was e.g. implemented to adress questions of classical [121, 122] and quantum magnetism [123] or to implement gauge fields for neutral atoms via time-periodic lattice shaking [124, 125]. Moreover, a triangular lattice with a two-site basis, called honeycomb lattice, with highly tunable state-dependent energy offset between the sublattices was realized [126–129]. In the special case of zero energy offset, artificial graphenelike

lattices were studied [130, 131]. Again, via periodic shaking, one applied Floquet theory for engineering topological quantum matter [128, 129, 132–140] and especially created the famous Haldane model with non-trivial Chern numbers [128, 129]. In the future, these lattices are of further interest, e.g. for the realization of artifical quantum magnets with frustated order [141]. While our choice of a triangular lattice is largely motivated by technical reasons that will be explained below, it also allows us to merge the described research on triangular lattice physics with the technical advantages of using lithium atoms, see e.g. [74, 142].
In our experimental setup the triangular lattice is formed by three red-detuned laser beams at $\lambda = 1069.8\,\mathrm{nm}$ that are equiangular separated within the horizontal plane (see Figure 5.8). In the case of out of plane polarization (s-polarization) the interference part of the lattice potential $V_\Delta(\vec{r})$ can be described by [143]

$$V_\Delta(\vec{r}) \propto -3 - 2\left(\cos\left[\left(\vec{b_{13}} - \vec{b_{23}}\right)\vec{r} + \phi_{12}\right] + \cos\left[\vec{b_{13}}\vec{r} + \phi_{13}\right] + \cos\left[\vec{b_{23}}\vec{r} + \phi_{23}\right]\right), \tag{5.4}$$

where

$$\vec{b_{13}} = \vec{k_1} - \vec{k_3} = \frac{2\pi}{\lambda}\begin{pmatrix}1\\0\\0\end{pmatrix} + \frac{2\pi}{\lambda}\begin{pmatrix}1/2\\\sqrt{3}/2\\0\end{pmatrix} = \frac{\pi}{\lambda}\begin{pmatrix}3\\\sqrt{3}\\0\end{pmatrix} \tag{5.5}$$

and

$$\vec{b_{23}} = \vec{k_2} - \vec{k_3} = \frac{2\pi}{\lambda}\begin{pmatrix}-1/2\\\sqrt{3}/2\\0\end{pmatrix} + \frac{2\pi}{\lambda}\begin{pmatrix}1/2\\\sqrt{3}/2\\0\end{pmatrix} = \frac{2\pi}{\lambda}\begin{pmatrix}0\\\sqrt{3}\\0\end{pmatrix} \tag{5.6}$$

are primitive reciprocal lattice vectors and $\phi_{jm} = \phi_j - \phi_m$ are the relative phases for two lattice beams.
Compared to a standard square lattice with $a_\square = \lambda/2$, our lattice has a larger spacing of $a_\Delta = 2\lambda/3$ that is comparable with the spacing formed in a 4-fold interference lattice with $a_\diamondsuit = \lambda/\sqrt{2}$ used in [63]. On the one hand, an upper limit for the lattice spacing is given by the necessity that the lattice geometry should offer the possibility that atoms significantly tunnel to other sites at low lattice depths when simulating a lattice Hamiltonian or by the required spatial resolution when studying continuous systems. On the other hand, a larger spacing always reduces the requirements for quantum gas microscopy, i.e. imaging with single-site resolution. A larger spacing might further be helpful for implementing free space cooling mechanisms in combination with single site fluorescence imaging at accessible laser power like it is the case for Rb atoms [18, 19].
Moreover, similar to the lattice geometries used in [77, 80] the modulation depth of the interference in next neighbor direction for a triangular lattice is at $8/9$ instead of $1/2$ that would be the case for a standard cubic lattice, meaning that tunneling in a deep lattice is better suppressed.
A triangular lattice is further advantageous since there is no need for retroreflection of the lattice beams, meaning that no additional optical isolator is needed to protect the laser source. This yields less wavefront distortion and less thermal lensing issues that is often attended with optical isolators.
In general a minimum of wavefront distortion is crucial for the lattice structure formed by interference. Thus, we couple each beam through the same kind of a single mode fiber[9]. This currently limits the maximum laser power per beam to

[9] NKT photonics: Photonic crystal fiber, aeroGUIDE POWER-15-PM, length: 5 m

8.5(5) W.

5.3.1 Laser system in front of the fibers

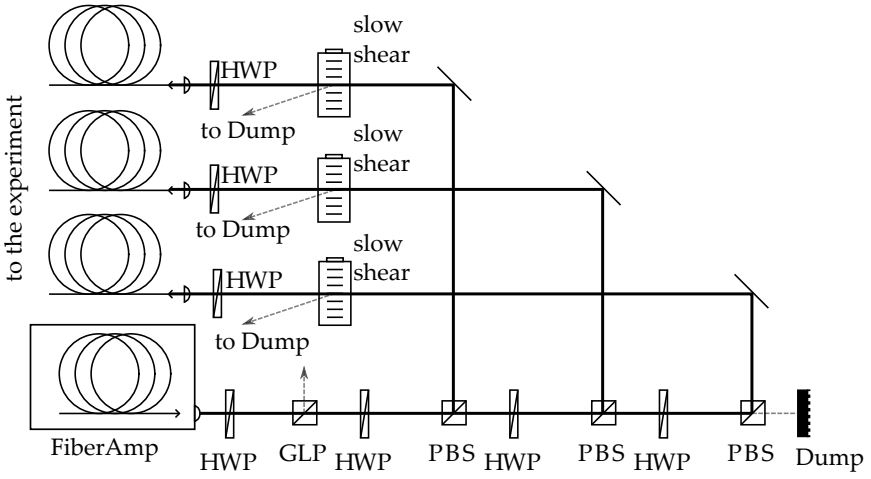

FIGURE 5.9: Sketch of the laser system distributing the light for the triangular pinning lattice – The light from a 40 W fiber amplifier is diffracted by three slow shear AOMs and coupled into fibers. The sketch does not include all adjustment mirrors and beam shaping optics. As a design library for drawing optics components the author used [85].

In order to distribute the laser light for all three lattice beams we build a laser system that suites to that purpose and couples the light in three fibers (see Figure 5.9).
First, the laser light coming from a 40 W fiber amplifier can be manually gated via a half waveplate and a Glan-Laser polarizer into a water cooled beam dump[10] or into use. During the alignment, we usually do not work with more than 0.1 W in front of each fiber.
Second, additional gates that are formed by half waveplates and PBSs distribute the light to three slow shear AOMs[11] that control the light of one lattice beam each in amplitude, frequency and phase (see Appendix A). The shear mode driven AOM especially offers very good thermal properties since it has a large aperture of 3 mm and the RF power requirement is < 1.0 W for diffraction efficiencies ~ 90 %.
Third, the light is coupled three times into a fiber via a commercial fiber collimator[12]. The collimator consists mainly of an achromatic lens ($f = 25$ mm). Within the optomechanical unit the position of the lens can be fine tuned for reaching coupling efficiencies of ~ 80 %. To reach those values for all three lattice beams, the laser system is designed in a way that all three beam paths that are in front of the fibers have nearly the same length and the same beam shaping lenses.
The polarization axes of the fibers are aligned to a PBS inside the outcoupling telescope optics with an accuracy of $\sim 0.5^\circ$ via a polarimeter[13]. This implies that the

[10] Altechna: 6-10BDWC01-2

[11] Gooch & Housego: I-M080-3S2G-3-LV11; The shear mode driven AOM has some non-standard properties that might be noted here for future issues: First, the 0^{th} order output goes under an angle of 6.45° with respect to the input beam. Second, the 1^{st} order output goes parallel ($\pm 0.2^\circ$) with the input beam and is orthogonally polarized with respect to the input beam. Third, the acoustic velocity of the shear mode in TeO_2 is only at 617 m/s, i.e. seven times slower compared to the standard longitudinal mode [144]. Nevertheless, for now we are not limited by the AOM timescales that are $< 1\,\mu$s.

[12] Schäfter + Kirchhoff: 60FC-SMA-T-23-M25-03

[13] Schäfter + Kirchhoff: SK 9780 - NIR; kindly provided by O.Hellmig

half waveplates that are placed directly in front of the fiber collimators should always maximize the power going onto the atoms.

5.3.2 Lattice telescopes and alignment

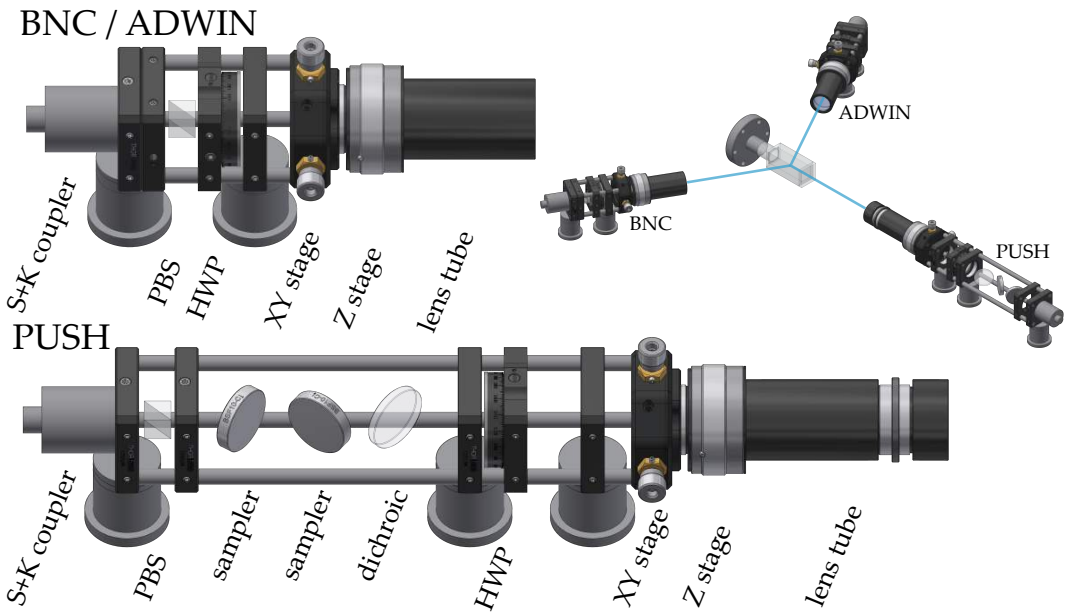

FIGURE 5.10: Sketch of the telescopes for the lattice beams – After the coupler the light propagates collimated through a PBS for polarization cleaning, a halfwave plate for polarization adjustment and in the case of the PUSH telescope through sampling optics and a dichroic mirror. Finally, XYZ stages provide a fine adjustment of the focus position onto the atoms by moving the focusing lens in the lens tube. In the upper right corner a small sketch shows the arrangement of the telescopes around the glass cell.

A sketch of the lattice telescopes is shown in Figure 5.10. For each telescope we start with the kind of fiber collimator that we already used for coupling the light into the fiber. For an optimal performance, we need to make sure that the 5° tilt axis of the collimator is aligned to the 5° facet angle of the fiber. The best way to do it, is to observe the collimated beam shape in far field with a CCD camera and to carefully turn the unscrewed SMA fiber tip until the shape changes from elliptical to round.
Behind each collimator we place a PBS to clean the polarization. As described in the last section, the axes of the polarization-maintaining (PM) fiber are aligned to this PBS. In the case of the ADWIN beam and the BNC beam a half waveplate for the choice of beam polarization and the achromatic focus lens[14] finalize the telescope. In the third lattice beam direction (PUSH), the outcoupled laser beam additionally has to propagate through two beam samplers[15] and a dichroic long pass mirror[16]. The dichroic mirror serves for absorption imaging purposes along the push beam direction (see Chapter 6.2). The beam samplers serve as pick-ups for intensity and phase control of the lattice beam that will be explained in the following subsections. Here, they need to be placed between the atoms and the fiber because after propagating through the ultracold cloud the beam is completely dumped inside the vacuum

[14]Thorlabs: AC254-150-C, $f = 150\,\mathrm{mm}$
[15]Thorlabs: BSF10-C
[16]Thorlabs: DMLP900

chamber[17] such that sampling the beam behind the atoms is impossible.
For the alignment, marked lines on the breadboards assure a coarse adjustment for the lattice angles. The couplers are placed on that lines at $\sim 150\,\mathrm{mm}$ distance to the atomic cloud without any additional adjustment mirror. The further alignment of the lattice beams can be done in two steps. A coarse adjustment for the BNC and ADWIN can be performed by overlapping the lattice beam and the fluorescence of a MOT on a CCD camera that is placed behind the recollimation lens for the lattice beam behind the atoms[18]. For further adjustment, we shortly switch on a lattice beam after producing a molecular BEC (see Chapter 4) and observe the influence of the dipole force created by the lattice beam. The position of the beam is then tuned by moving the focussing lens in the telescope via a combined XYZ stage[19].
When all beams are aligned carefully onto the mBEC and when we switch on the beams for a few μs, we can observe[20] generalized Kapitza-Dirac diffraction [145] when performing a ToF expansion (see Figure 5.11). For future experiments, Kapitza-Dirac diffraction is a suitable method to study relevant lattice paramters, like e.g. in [80, 118, 146–148].
In order to proof the suitability of the lattice potential, we measured the caustic of all three lattice beams and estimated important properties that are relevant for a pinning lattice. The results are summarized in Table 5.2. The listed lattice depth and the on-site trap frequency are comparable to other pinning lattices implemented in existing quantum gas microscopes for ^{6}Li [74, 77, 80].

TABLE 5.2: Main properties of the triangular lattice – For the beam waist, its quality factor and the beam power the error is given by combining the measurement uncertainty and the corrected sample standard deviation. For all further calculated values a standard error propagation is used.

lattice spacing (nm)	713
beam waist (μm)	41(3)
beam quality factor M^2	1.05(2)
power per beam (W)	8.5(5)
lattice depth (mK)	1.6(1)
on-site trap frequency (MHz)	1.3(1)

5.3.3 Analysis of optical phase noise

For this subsection we want to focus on the relative phases ϕ_{jm} from Equation 5.4. When these phases change in time, the lattice potential shows the same pattern but the positions of the lattice sites move inside the 2D slice [143].

[17] During the alignment onto the ultracold gas we tried to let the beam partially travel through the differential pumping tube but since it is out of black graphite it quickly heats up due to the clipping laser power and we observe that the pressure in the glass cell increases by up to 3 orders of magnitude. When instead shining the laser light with an intensity of $\sim 10^6\,\mathrm{W/m^2}$ onto the stainless steel wall next to the pumping tube by slightly changing the angle of the beam within the horizontal plane, we observe only a small increase in pressure for the first experimental cycles. We interpret this observation as a forced local "bake out" via laser induced heating.

[18] Here, care must be taken to not damage the camera by turning to much power into the lattice beam!

[19] Thorlabs: CXY1 and SM1ZM

[20] This first observation is taken just before we needed to refill the lithium oven. More details on Kapitza-Dirac diffraction will surely follow in future theses.

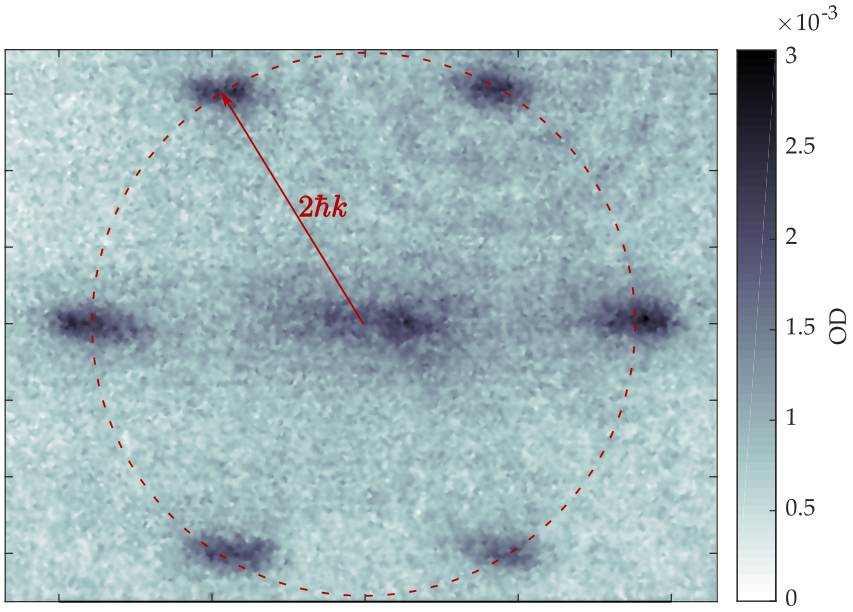

FIGURE 5.11: First order Kapitza-Dirac diffraction peaks – Molecules in the 6 first order peaks carry a net momentum of $2\hbar k$ with $k = 2\pi/\lambda$ with $\lambda = 1069.8\,\text{nm}$. With the given ToF $\tau = 3.25\,\text{ms}$ and by fitting the radius of the dashed red circle to our camera image ($r = 1.76(2)\,\text{mm}$), we can calibrate the magnification $M = r\,m_{\text{Li}}/\hbar k\tau = 8.7(1)$ to our image. The imaging lenses are the high resolution objective ($f_{\text{eff}} = 25\,\text{mm}$) and a plano-convex lens with $f \sim 250\,\text{mm}$.

In order to quantify the effects of noise in the relative phases ϕ_{jm}, we analyze the time dependent intensity $I_{\text{int}}(t)$ of two interfering lattice beams that is given by

$$I_{\text{int}}(t) = I_j(t) + I_m(t) + 2\,|E_j(t)E_m(t)|\,\cos\left(\omega_{jm}t + \phi_{jm} + \delta\phi(t)\right), \tag{5.7}$$

with $I_{j,m}(t) = |E_{j,m}(t)|^2$ and $E_{j,m}(t)$ being the electric field amplitudes for the single lattice beams j, m and $\delta\phi(t)$ being the relative optical phase noise. The frequency difference of the lattice beams at the photodiode is given by $\omega_{jm} = \omega_j - \omega_m$.
For our measurement[21] we place the photodiode at the overlap of the first diffraction order of lattice beam j and the zeroth diffraction order of the lattice beam m behind an AOM[22]. Thus, the AOM provides $\omega_{jm} = 2\pi \times 85\,\text{MHz}$ even though the lattice beams have the same frequency when they propagate through the ultracold cloud. By measuring the phase at 85 MHz and by using a high passed photodiode[23], we suppress intensity noise that is dominant at low frequencies. Furthermore, we make sure that no other frequency sources couple into our signal by blocking each beam separately and observing the 85 MHz peak vanishing on a spectrum analyzer[24]. For a clean interference signal, we also make sure that the beam shapes of the two lattice beams are similar at the position of the photodiode. Finally, we can state for the photodiode current that

$$i_{\text{PD}} \propto \cos\left(\omega_{jm}t + \phi_{jm} + \delta\phi(t)\right). \tag{5.8}$$

[21] The test setup is sketched in Figure A.7.
[22] Gooch & Housego: AOM 3080-197
[23] Hamamatsu: G8370-03 & Mini-Circuits: Bias-Tee ZFBT-6G+
[24] Rhode & Schwarz: FSV7

Now in the frequency domain, the photodiode signal is broadened by phase noise. Via a binning of the phase noise in sufficiently small frequency steps, we can write that[25]

$$\begin{aligned} i_{\mathrm{PD}} \propto \cos\left(\omega_{jm}t + \delta\phi(t)\right) \approx \sum_{\ell}\Big\{ & J_o\left(\delta\phi_\ell\right)\,\cos\left[\omega_{jm}t\right] \\ & + J_1\left(\delta\phi_\ell\right)\,\cos\left[\left(\omega_{jm}+\omega_\ell\right)t\right] \\ & - J_{-1}\left(\delta\phi_\ell\right)\,\cos\left[\left(\omega_{jm}-\omega_\ell\right)t\right]\Big\} \\ \approx \sum_{\ell}\Big\{ & \cos\left[\omega_{jm}t\right] \\ & + \delta\phi_\ell/2\,\cos\left[\left(\omega_{jm}+\omega_\ell\right)t\right] \\ & - \delta\phi_\ell/2\,\cos\left[\left(\omega_{jm}-\omega_\ell\right)t\right]\Big\}, \end{aligned} \tag{5.9}$$

with J_p being the p^{th} order Bessel function of the first kind, ω_ℓ being the frequency of the binning interval and $\delta\phi_\ell \ll 1$ being the deposited phase noise amplitude. The electric RF power in a single sideband (SSB) at $\omega_{jm}+\omega_\ell$ is then

$$P_{\mathrm{SSB}}(\omega_\ell) \approx \left(\delta\phi_\ell/2\right)^2 \tag{5.10}$$

and can be measured and analyzed via our spectrum analyzer such that we can extract the frequency dependence of the phase noise between two lattice beams. As shown in Figure 5.12, we did not only measure the phase noise of the setup with fiber coupled lattice beams but also without fibers. We can therefore state that the additional phase noise from the fibers is located at frequencies below $\sim 300\,\mathrm{Hz}$. Nevertheless, during our measurements we could clearly observe increased phase noise when touching the fibers or by increasing the acoustic noise in the laboratory. Via our self-assembled and self-programmed low noise AOM driver (see Appendix A) we can realize an active feedback loop that reduces the measured phase noise for frequencies up to $\sim 2\,\mathrm{kHz}$ and shows a servo bump peaked at $\sim 10\,\mathrm{kHz}$. Anyhow, even if an active feedback shows remarkable results, it increases the amount of technical complexity[26] and may not be required in our setup as we observed during our measurements that are explained in the following.

Considering optical lattices for atom trapping, the frequency dependence of phase noise always needs to be related to the frequency response of the trapped atoms inside the lattice. Depending on the on-site trap frequency ω_{ost} or just more general on the bandstructure of the lattice, phase noise may induce parametric heating and additional loss terms.

In the case of our triangular pinning lattice $\omega_{\mathrm{ost}} = 2\pi \times 1.3(1)\,\mathrm{MHz}$ such that regarding the frequency dependence of the measured phase noise (see Figure 5.12), we are in a regime where the atoms on the lattice sites mainly perform a motion that depends on the current phase noise values. When collecting their fluorescence for $\sim 1\,\mathrm{s}$, the motion will blur the image even if every atom remains cooled on its site.

We can now estimate how severe this blurring effect may disturb the image quality by, in a first step, calculating the phase noise induced overall rms fluctuation

[25] In this equation we chose a time shift that sets $\phi_{jm} = 0$ without loss of generality.

[26] One technical issue that we are currently discussing (see Appendix A.5) is e.g. the start of the lock. Here, usually the phase shortly oscillates because the lock controller needs to find the setpoint of the signal.

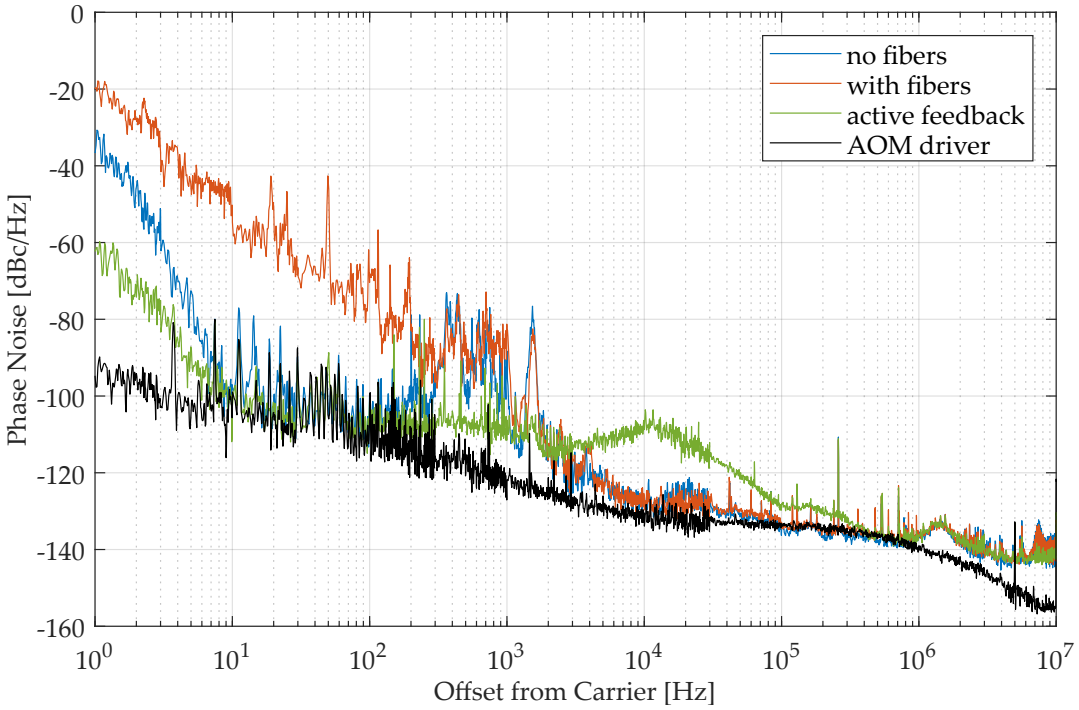

FIGURE 5.12: Measurements on the relative optical phase noise between two beams of the optical lattice – Here the deposited RF power in a single sideband P_{SSB} relative to the RF power in the carrier at 85 MHz is plotted in dBc/Hz. The curves show the phase noise of a setup with and without fiber coupled lattice beams (red, blue) as well as the case where the AOM of one fiber coupled lattice beam gets an active feedback to lower the relative phase noise (green). The line in black shows the phase noise present in the signal coming from the AOM driver. It serves for comparing the signals to their background noise limit.

$$\Delta\phi_{\mathrm{rms}} = \sqrt{\frac{1}{t_e}\int_0^{t_e} [\delta\phi(t)]^2\, dt}, \tag{5.11}$$

where t_e is the exposure time. Using the Parseval theorem we find that

$$\Delta\phi_{\mathrm{rms}} = \sqrt{\int_{2\pi t_e^{-1}}^{\infty} [P_{\mathrm{SSB}}(\omega)]^2\, d\omega} = \left(\frac{1}{4\pi}\sum_{\ell=\ell_e}^{\infty}\delta\phi_\ell^2\right)^{1/2} \tag{5.12}$$

such that we can extract $\Delta\phi_{\mathrm{rms}}$ from the data of Figure 5.12 and list it in Table 5.3 for every curve.

TABLE 5.3: $\Delta\phi_{\mathrm{rms}}$ calculated from the curves of Figure 5.12

	$\Delta\phi_{\mathrm{rms}}$ (°)
no fibers	1.01
with fibers	6.85
active feedback	0.08
AOM driver	0.02

If we now assume that phase noise is random and normally distributed with a standard deviation of $\Delta\phi_{\mathrm{rms}}$ we find numerically that the lattice sites in our 2D potential

are locally spread with a standard deviation of $\sigma_{\mathrm{pn}} \propto \Delta\phi_{\mathrm{rms}}$ for small values of $\Delta\phi_{\mathrm{rms}}$ and that $\sigma_{\mathrm{pn}} = 9.51(6)\,\mathrm{nm}$ if $\Delta\phi_{\mathrm{rms}} = 6.85^\circ$ like it is the case for our current lattice configuration. Comparing σ_{pn} with e.g. the oscillator length on each lattice site $a_{\mathrm{osc}} = \sqrt{\hbar/2m_{\mathrm{Li}}\omega_{\mathrm{ost}}} \approx 64\,\mathrm{nm}$, we find an indication that blurring by phase noise will not limit the imaging resolution.

5.3.4 Intensity control

For a loading of the atoms into a pinning lattice, we need to ramp the lattice depth and so the laser power on a range of three orders of magnitude from a few mW up to 8.5 W that is our maximum power per beam corresponding to a lattice depth of $\sim 1.6(1)\,\mathrm{mK} \,\widehat{\approx}\, 2.3(1) \times 10^3\, E_{\mathrm{rec}}$[27].
At first, we need to smoothly ramp up the lattice depth until tunneling between lattice sites is suppressed. This regime is usually reached at lattice depths of $\lesssim 50\, E_{\mathrm{rec}}$ (see e.g. [31, 80, 149]) and ramping times are on the order of $10 - 100\,\mathrm{ms}$.
Second, for pinning fluorescing atoms much deeper lattices are required as the atoms are randomly kicked by spontaneous emission photons. For that purpose, a ramp to the maximum in about $100\,\mu\mathrm{s}$ is used in [80].
Due to technical reasons an active feedback control is only designed for beam powers up to $\sim 600\,\mathrm{mW} \,\widehat{\approx}\, 160\, E_{\mathrm{rec}}$. For higher powers we switch off the active feedback and ramp in a feed forward fashion to the maximum available power.
Within the last days of working in the laboratory the author installed a first version of a feedback control for low lattice powers that is successfully used to load atoms into the lattice potential. The electronic setup (see Figure 5.13) consists basically on a voltage variable attenuator[28] (VVA) and a servo controller[29] and is developed in close collaboration with the Spinor Team of our research group. A detailed description of the design and of the lock properties will be found in future theses. As the amplitude noise of our lattice laser after all the amplification stages is an important measure [150, 151], it is shown in Figure D.1.

[27] E_{rec} is the recoil energy of a lattice photon
[28] Analog: HMC346AMS8GE
[29] New Focus: LB1005-S

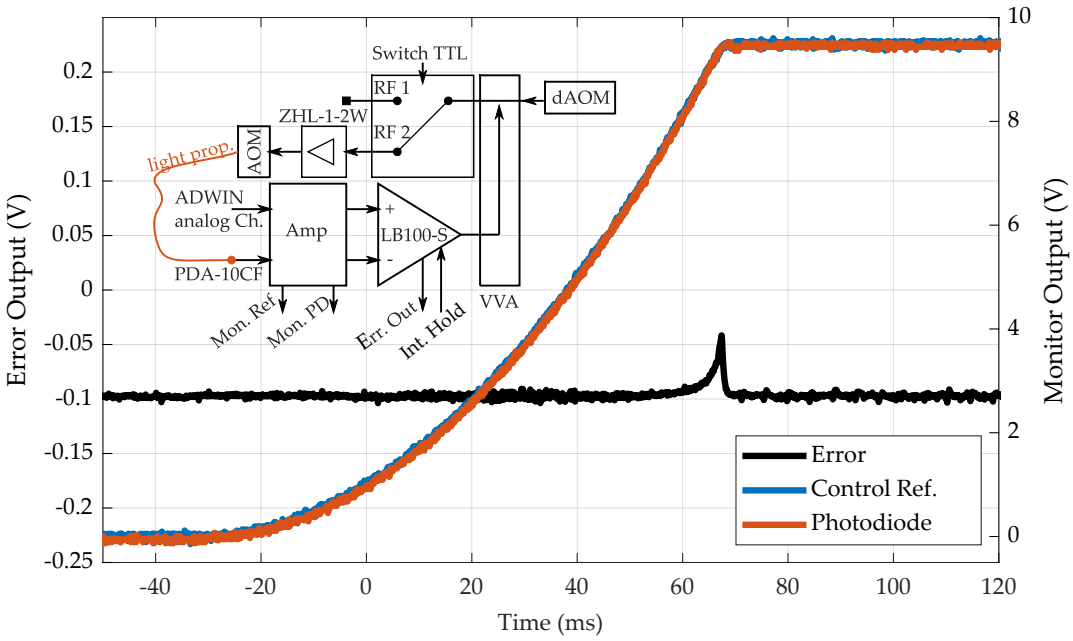

FIGURE 5.13: Ramping up the pinning lattice – As an example, an exponential ramp of 100 ms to 600 mW for the PUSH lattice beam is shown. The voltage on the photodiode that is placed behind a beam sampler of the telescope is plotted in red and the corresponding control voltage in blue. The difference error voltage is shown in black. It has an offset of −100 mV to assure the lowest possible power in the beam at the start of the ramp. A small kink in the signal indicates the turn to a constant value at the end of the ramp. – The inlet shows a sketch of the feedback control setup. First, a low noise amplifier board serves to match the photodiode voltage range to the control reference voltage from the ADwin experimental control and to monitor both. We then choose the LB100-S servo controller from NewFocus. Its error monitor serves for analysis purposes. Furthermore, the servo provides a voltage for the VVA. Here, the RF signal coming from our digital AOM driver board is attenuated by maximally −30 dB. If the "Int. Hold"-TTL at the servo is high a constant control voltage can be applied to the VVA. Its value can be adjusted via a potentiometer knob. In our case, we set this knob to minimum attenuation and hence, in a first approach our plan is to pin the atoms in a deep lattice via this TTL.

Chapter 6

Imaging

Nearly all information of an ultracold gas is obtained by taking and analyzing images. In a first section of this chapter the author reports on preparatory steps to realize single-site fluorescence imaging with a high-NA objective. For these steps, the author was mainly responsible. The second section of this chapter reports on auxiliary absorption imaging of lithium atoms that was primarily implemented by the author after consultations with B. S. Rem and Michael Hagemann.

6.1 Imaging with a high-NA objective

As stated in the previous chapters, we aim for quantum gas microscopy or, more precisely, single-site resolved fluorescence imaging of a 2D cloud in a triangular pinning lattice. Our high-NA objective[1] therefore ensures a beneficially large collection efficiency of fluorescence photons emitted uniformly into the 4π solid angle ($\sim 6.7\,\%$) and a resolution that allows to distinguish between full and empty lattice sites. Its characteristics are given in Table 6.1.

TABLE 6.1: Characteristic data of the objective that is corrected for a 5 mm window of borosilicate glass or fused silica.

Numerical aperture (NA)	0.5
Effective focal length	24.7 mm
Working distance	19 mm
Field of view	150 μm
Depth of focus at 671 nm	2.7 μm
Diffraction limited for	532 nm
	671 nm
	780 nm
	1064 nm
AR coating for 532-1064 nm	$< 0.5\,\%$
Achromatic focal shift	$< 80\,\mu$m
Aperture	25 mm

Since the objective is infinity corrected, we require an additional tube lens for imaging. If we approximately treat the objective as one lens, we can thus assume that our fluorescence imaging system consists of two lenses[2] where we call the lens that is

[1] custom product from Special Optics, item 1-21992

[2] like all the absorption imaging systems mentioned in Section 6.2

near to the atoms *objective* with a focal length f_1 and the lens close to the camera *tube lens* with a focal length f_2.
For our specific experimental parameters Jan-Mika Jacobsen finds in his Master's thesis [97] that an optimal magnification is in the range of $M_b = -65$ to $M_b = -95$. This explains our choice of tube lens that has a focal length of $f_2 = 2\,\mathrm{m}$. As a result we have $M_b \approx -80$.
Like described in the Bachelor's thesis of Tobias Petersen [152], we observe experimentally a reduction in the effective numerical aperture for the $1''$ lens provided by the objective designers. Therefore, we choose a tube lens[3] with a larger aperture of $2''$.

6.1.1 Adjustment of the imaging system

Already from geometrical optics [153] we may deduce that the distance between the tube lens and the clear image b is mainly effected by the distance between the ultracold sample and the objective $g = f_1 + \epsilon$. If $\epsilon \to 0$, we get

$$b\,(\epsilon, \zeta) = f_2 - \frac{f_2^2}{f_1^2} \cdot \epsilon - \frac{f_2^2}{f_1^4} \cdot \epsilon^2 \zeta - O(\epsilon^3 \zeta^2) \tag{6.1}$$

with $\zeta = d - (f_1 + f_2)$ and d being the distance between objective and tube lens.
From this equation we can conclude that the position of a clear image mainly depends on the adjustment of the objective to a distance $g = f_1$ whereas the distance d between the two lenses is less important. Hence, a correct adjustment of the objective with respect to the ultracold 2D sample is crucial for a diffraction limited imaging system. We therefore designed an adjustment tower (see Figure 6.1) that fixes the objective up to the following degrees of freedom with respect to our optical table:

- **Tilt.** We want the propagation axis of the collected light to be perpendicular to the ultracold 2D sample in order to minimize aberrations like astigmatism and coma. Thus, we install two tilting tables[4] for both tilting directions $\theta_{x,y}$. They are the base[5] of the arrangement in order to decouple the XYZ fine adjustment from a tilt.

- **XY.** We want the atoms to be within the field of view of the objective that is $\sim 150\,\mu\mathrm{m}$. We thus install an XY stage[6] in our arrangement.

- **Z.** Once we find the atoms lying within the field of view, we need a clear image on our camera[7] chip. Since the depth of focus in a diffraction limited setup is only $\Delta z = \lambda/\mathrm{NA}^2 \approx 2.7\,\mu\mathrm{m}$ we need to carefully align the translation of the objective in z direction. We thus install a piezoelectric objective scanner[8] that is e.g. used in [119]. It has a travel range of $100\,\mu\mathrm{m}$, a precision of 10 nm and a typical settle time of $\sim 6\,\mathrm{ms}$. The adjustment is electronically accessible and the scanner has capacitive sensors that can be activated to control dynamics.

Even if the positioning of the tube lens plays a minor role, we however recognized during during test measurements that a tilt adjustment of the tube lens and its positioning perpendicular to the light propagation axis is useful to minimize aberrations

[3] Melles Griot: PLCX-50.8-999.4-UV-633-1064
[4] Owis: NT 65x120-FGS
[5] The tilting tables are placed on a z lift table – Owis: HT 100-30 – providing a coarse z adjustment.
[6] Owis: KT 65-STA-UM
[7] Oxford Instruments: Andor iXon Ultra 897
[8] Physik Instrumente: P-726 PIFOC

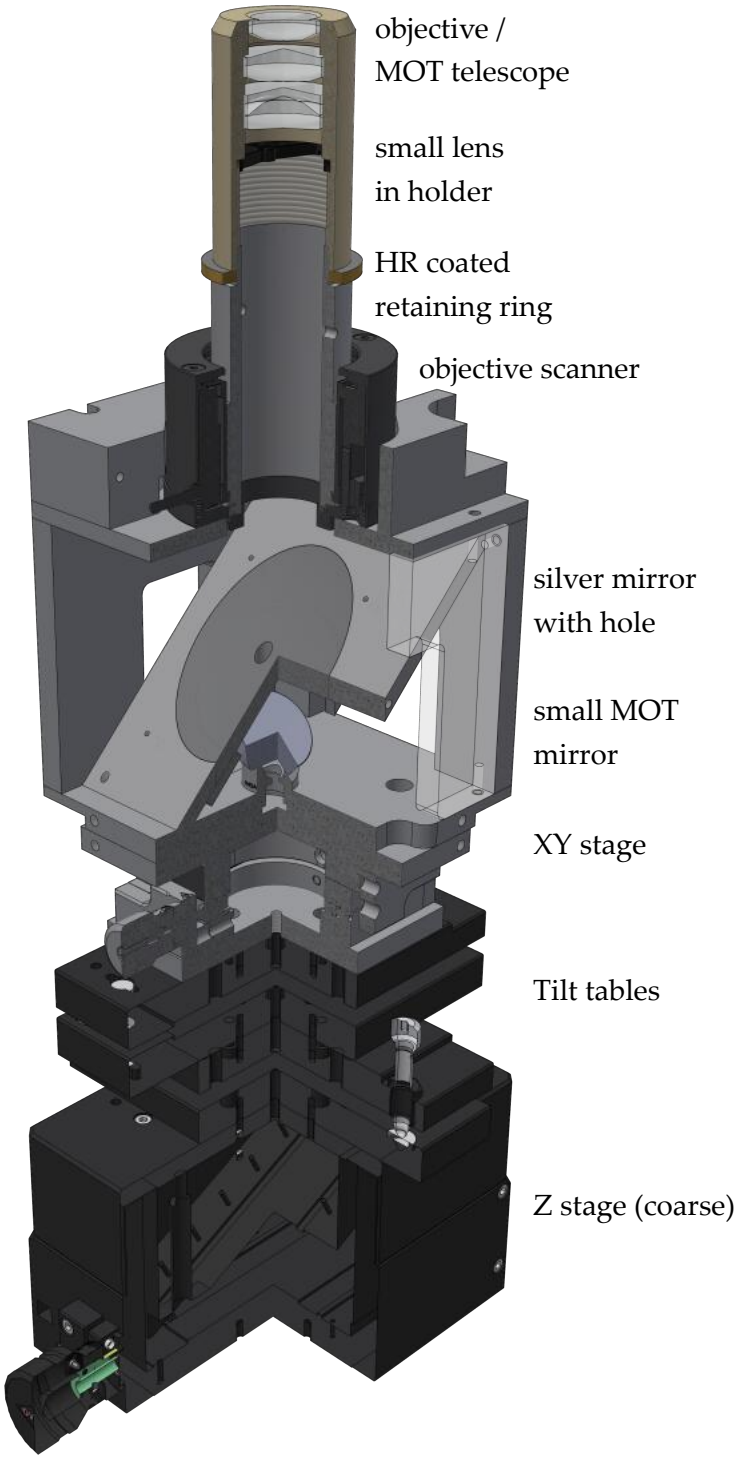

FIGURE 6.1: CAD sketch of the optomechanics for the objective adjustment – From the bottom of the optical table a Z stage lifts the objective coarsely to the right position. The tilt tables orient the objective lenses to the 2D plane of atoms. The XY stage moves the field of view. An objective scanner focuses the objective onto the fluorescing atoms. An HR coated retaining ring will be helpful for additional auxiliary laser beams for adjustment purposes. The small lens of the MOT telescope is located directly in the objective tube. The silver mirror with the hole is inside a cubic arrangement fabricated in the mechanical workshop. A small MOT mirror is placed below the hole.

as described in [152]. For this reason we also place the tube lens into a lens positioner[9].

6.1.2 MOT through objective

Since we do not transport the ultracold cloud (see Chapter 2), the MOT is centered at the focus position of the objective and one MOT beam has to travel through the objective. It needs to be collimated when propagating through the atoms and its waist should not reduce the intersection volume of all MOT beams. We thus need to built a telescope with the high-NA objective being the recollimation lens. This means that when using usual beam sizes, we need to place the other telescope lens close to the objective to get a waist that is large enough on the atoms.
In our case, we choose an $f = 4\,\mathrm{mm}$ lens[10] with a small diameter of 4 mm that is inserted into the tube holder of the objective by using a 3D printed holder (see Figure 6.2a) that is printed in our workshop. It holds the lens at 6 mm off-axis because we do not want to manipulate the low frequency parts of the collimated imaging information of the fluorescence image that will be important for cold clouds that fill the lattice homogeneously. On the other hand, the off-axis position of the first lens gives rise to an angled MOT beam. It is tilted within xz plane by $\sim 14^\circ$ with respect to the z axis (see Figure 6.2b). We obtain a waist of $\sim 0.6\,\mathrm{cm}$ as a MOT beam by shining a collimated beam with a waist of $960(20)\,\mu\mathrm{m}$ onto the small lens.
In order to separate the light paths for the MOT beam and for the fluorescence image, O. Hellmig kindly thrilled a hole with a diameter of 5 mm in a $2''$ elliptical silver mirror such that we can place it below the objective (see Figure 6.2a). The light for the MOT beam is then fully propagating through the hole whereas $\sim 96\,\%$ of the collected fluorescence photons get reflected by the silver mirror into the direction of the camera without hitting the small lens.
When implementing the objective into the experiment, we redistribute the power in the MOT beams in order to shape the MOT to a round ball again as it is described in the Master's thesis of Mathis Fischer [103]. Here, the angled beam that is slightly larger than the other beams needs as much power as the horizontal beams whereas the MOT beam that propagates completely vertically in $-z$ direction needs only $\sim 60\,\%$ relative power. Fortunately, the atom number and the phase space density after gray molasses did not reduce significantly due to the upgrade.
Another important advantage of our described approach will become relevant in a future stage of the experiment since in principle it allows the insertion of a second similar objective above the science cell without loosing the possibility for a MOT.

[9] Newport: LP-2A
[10] Edmund Optics: # 48-702

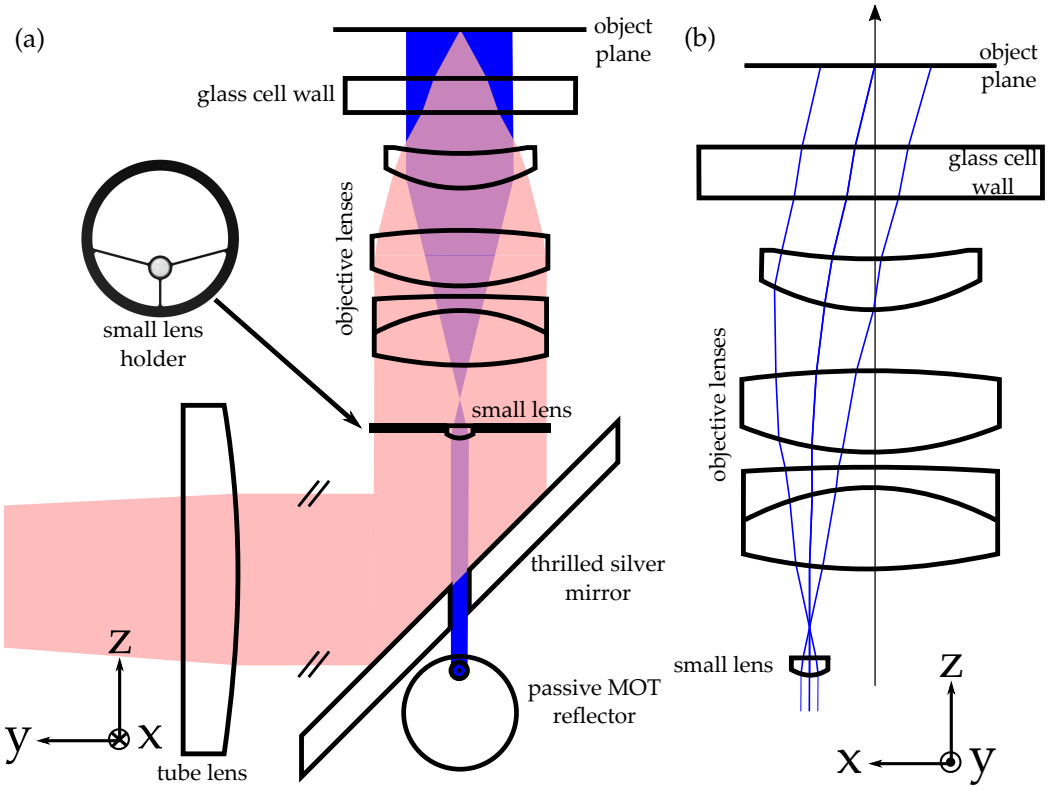

FIGURE 6.2: Beam paths through the objective – (a) A sketch of the light path of the collected fluorescence photons (red) and the MOT beam (blue) parallel to the yz plane. A small beam with adjusted polarization propagates from a passive reflective mirror through a hole in a silver mirror onto a small lens. The focussed beam is recollimated and magnified by the objective and suits for a MOT. The fluorescence photons are collected by the objective. $\sim 96\,\%$ pass by the lens holder without any manipulation and are reflected by the silver mirror before they are focused by the tube lens onto a camera chip. (b) Ray traces of the MOT beam in the xz plane calculated with ZEMAX OpticStudio. The small lens is decentered by 6 mm. This yields an angle of $14\,^{\circ}$.

6.1.3 Measuring the Point Spread Function

Before implementing the objective tower into the experiment, we characterize the objective properties separately for making sure that it is suitable for resolving fluorescing single atoms on the sites of our lattice geometry.
By taking into account that our setup is at least limited by diffraction caused by the finite apertures of the lenses, we can analyze the so-called point spread function (PSF) that characterizes our resolution. In the ideal case,

$$\mathrm{PSF}(\rho) \propto \left(2J_1(\rho)/\rho\right)^2, \tag{6.2}$$

with

$$\rho(x,y) = \mathrm{NA}\, k \sqrt{x^2+y^2} \tag{6.3}$$

being the radial optical coordinate for a beam propagating in z-direction, $k = 2\pi/\lambda$ with λ being the wavelength of the fluorescence photons and $J_1(\rho)$ being the first order Bessel function.
In our case, we numerically calculate the PSF of the objective and compare the result to a measured PSF from a test setup:

- For the calculation we insert the objective in an ideally collimated beam and look at its focus with a ray tracing software[11]. The small MOT lens and the 5 mm hole in the mirror is approximated by a circular obscuration.
- For the measurement, we first want to thank Joakim Reuteler from the ScopeM team of the ETH in Zurich for piercing small holes with a diameter $d \approx 200\,\mathrm{nm}$ into the coating of a glass side[12]. We use it to shine laser light through the small holes of the coating and observe the point-like structures ($d < \lambda$) with our objective and a setup that is further explained in [152].

Figure 6.3 shows an example image of a 200 nm hole that is imaged at $\lambda = 671\,\mathrm{nm}$. In order to test the effective NA of our imaging system, we compare our measurement to the width $\sigma = \lambda/\left(\pi \times \mathrm{NA}_{\mathrm{eff}}\right)$ that is given at $4J_1(\rho = 1)^2 \approx 0.775$. For the curves that we obtain from our simulations where the small lens is considered as an obstruction, we look at their first minimum $x_{\mathrm{min}} = 0.61\,\lambda/\mathrm{NA}_{\mathrm{eff}}$.
By overlapping the calculated data with a cut through the experimental image, we observe a good agreement in width. All data fit well to a $\mathrm{NA}_{\mathrm{eff}} \sim 0.5$ like it is summarized in Table 6.2. We can therefore state that the mirror hole as well as the small lens do not disturb the imaging performance significantly.

TABLE 6.2: $\mathrm{NA}_{\mathrm{eff}}$ for the data shown in Figure 6.3

	data name	**$\mathrm{NA}_{\mathrm{eff}}$**
measurement	Data along 1	0.50(1)
	Data along 2	0.53(1)
simulation	PSF $(x, 0)$	0.519(1)
	PSF $(0, y)$	0.503(1)

[11] Zemax: OpticStudio, lens data are provided by Special Optics
[12] He pierces a $\sim 250\,\mathrm{nm}$ PtPd coating with a focussed ion beam (FIB) and measures the coordinates of the holes via a scanning electron microscope (SEM).

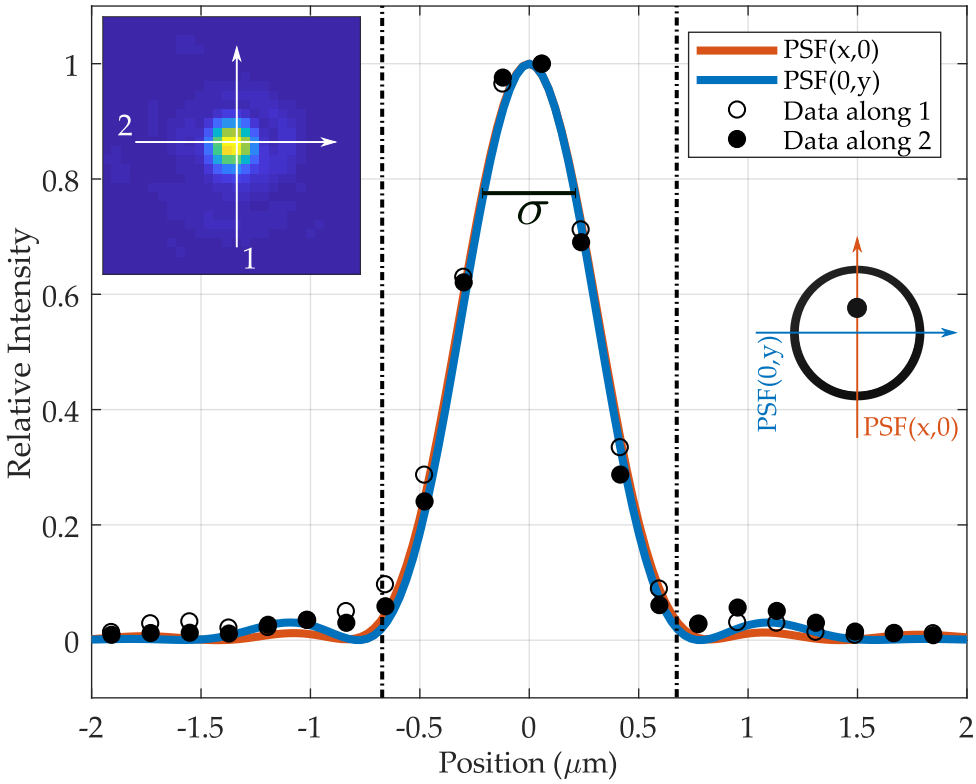

FIGURE 6.3: Testing the fluorescence imaging system – We cut through a 2D camera image that is shown in upper left corner and compare the pixel data (black dots and circles) with the theoretical 1D PSF calculated with our optical ray trace software along two orthogonal axes x (red) and y (blue). For the calculation an obscuration of 5 mm that is decentered by 6 mm along the x direction approximates the small MOT telescope lens and the hole in the silver mirror behind the objective. We observe that the curve is slightly broadened along x and that more light is transferred to the Airy rings along y. The widths of the pixel data are in good agreement with the numerical data. Their slight asymmetry may be induced by a small tilt of the objective relative to the glass side and due to the fact that the pixel direction may not completely coincide with the axis of the decentered lens. All curves show that we are within the range of a NA $= 0.5$ that is indicated by σ. The positions of the neighboring lattice sites are indicated by black dashed lines at $\pm$713nm.

6.2 Absorption imaging

For all adjustment and build up stages that are reported in this thesis absorption imaging is essential to obtain information about the gas. When performing absorption imaging, resonant light is shone onto the atoms such that they cast a shadow onto a CCD camera[13]. More precisely, we obtain an intensity distribution $I_{\text{abs}}(x,y)$ on our camera. By referencing this distribution to an image without atoms $I_{\text{ref}}(x,y)$, we can estimate the column density distribution of the atoms

$$\tilde{n}(x,y) = \sigma_{\text{eff}}^{-1} \ln\left(I_{\text{ref}}(x,y)/I_{\text{abs}}(x,y)\right) \tag{6.4}$$

that is integrated along the imaging axis z. Here, the value of the effecitve cross-section σ_{eff} can be calculated by applying the Beer-Lambert law[14] and by including

[13] PCO: Pixelfly QE or Pixelfly USB

[14] If the light beam intensity I is comparable or even larger than the saturation intensity I_{sat} of the atomic transition, the value of σ_{eff} will become intensity dependend as it is e.g. treated in [154, 155]. Moreover, in the case of weakly bound molecules σ_{eff} is slightly reduced as e.g. discussed in [156].

all relevant parameters of the imaging system.
In our case, the two images are taken each in 10 μs with intensities that depend on the density of the cloud and on the imaging direction (see Figure 6.6b). In between the images we have a data transfer and storage period of 200 ms. For stray light correction we further take dark images for which the laser light beam is switched off.

6.2.1 Imaging transitions in magnetic fields

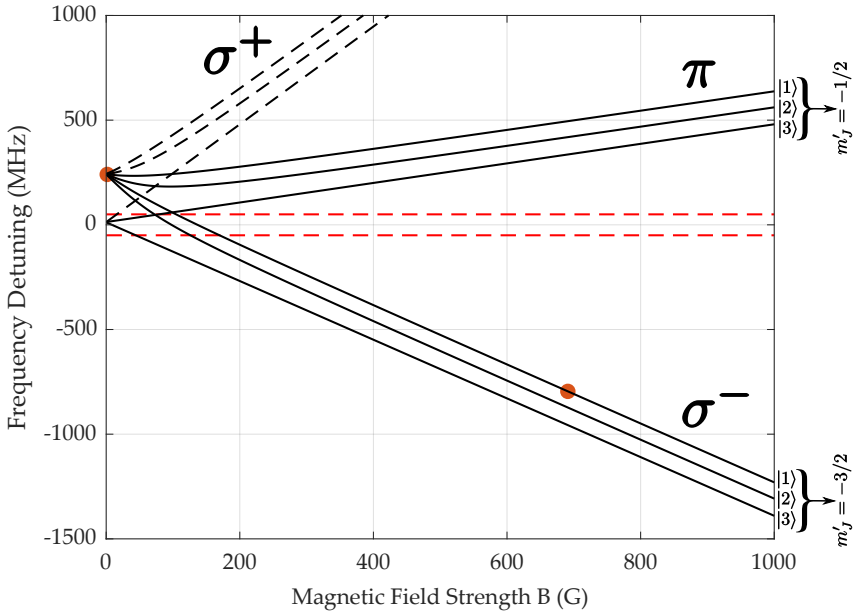

FIGURE 6.4: Imaging transitions between the three lowest states $|1,2,3\rangle$ in the $2^2S_{1/2}$ manifold and the states in $2^2P_{3/2}$ as a function of magnetic field strength – Note that the lines correspond to transitions rather than to atomic levels that can be found in Appendix B. The zero is chosen with respect to the frequency measured at the offset lock photodiode, meaning zero frequency difference to the D2 master laser. The red dashed lines indicate the frequency interval of the plot that is not accessible with the current offset lock. The σ^+ transitions are dashed because we never used them for imaging. The usual positions of the plot where we image our clouds are marked with a red circle each. For further explanation see e.g. [157–159].

When ultracold lithium is exposed to magnetic fields not only their interaction is changing because of Feshbach resonances [62] but also the intraatomic energy levels split up and shift (see Appendix B). Since lithium has relatively small hyperfine splittings compared to other alkalis, the Zeeman interaction can only be treated as a perturbation for very small magnetic field strengths [157]. Thus, the transition between intraatomic energy levels and so the correct laser frequency for resonant absorption imaging strongly depends on the present magnetic field strength B.
For our purposes, we restrict the imaging frequencies to drive σ^- and π transitions on the D2 line from the three lowest states $|1,2,3\rangle$ in the electronic ground state $2^2S_{1/2}$ of ^{6}Li (see Figure 6.4). At low fields the ground states $|1,2\rangle$ are projected into the $F = 1/2$ manifold whereas $|3\rangle$ can be identified as the stretched state $|F = 3/2, m_F = -3/2\rangle$ (see Appendix B). At high fields the ground states $|1,2,3\rangle$ can be excited to different spectroscopic triplets of the $m_{J'}$ manifolds in the excited state depending on the laser frequency and on the type of transition ($\sigma^\pm$ or π). Our computer code for calculating the respective transition frequency is based on [157].

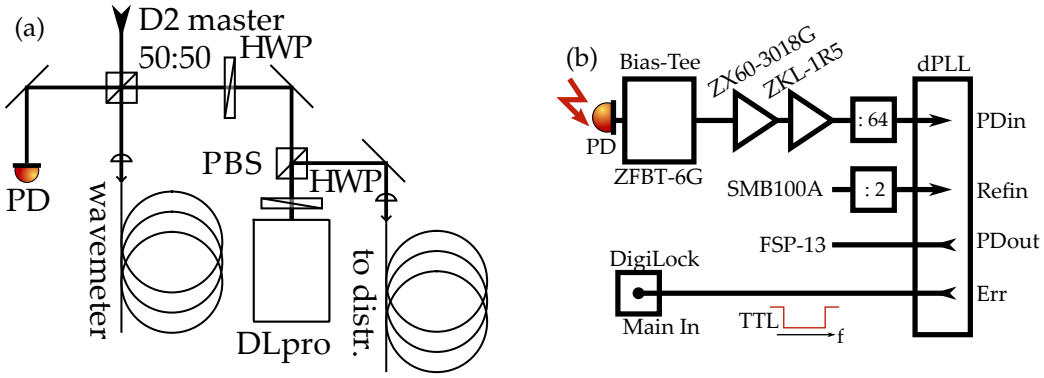

FIGURE 6.5: Sketch of the offset lock system – (a) At the laser part the light from a DL pro is coupled into two different fibers and overlapped with the D2 master laser for a frequency comparison. The comparison is done by first bringing the laser frequencies close together via a wavelength meter and then measuring the beat signal on a fast photodiode (PD). As a design library for drawing optics components the author used [85, 104]. (b) The signal is amplified and compared to a reference signal from a signal generator (SMB100A). As long as the beat frequency is smaller than the reference signal, including the division factors, the output of our dPLL (digital Phase-Locked Loop) box is a TTL low. The Digilock, belonging to the laser electronics, locks the laser to the frequency where the TTL is supposed to change from low to high. With our spectrum analyzer (FSP-13) we can have a look on the beat frequency during the lock. As a design library for drawing optics components the author used [104].

From an experimental point of view it might be useful to state that for $B \gtrsim 350\,\mathrm{G}$ the increase in frequency is mostly linear. For the σ^- transitions it is $\propto -\kappa$ and for π transition it is $\propto +\kappa/3$ with $\kappa \sim 1.4\,\mathrm{MHz/G}$.

6.2.2 Laser system for absorption imaging and its offset lock

The light that we need for imaging the gas is provided by another ECDL laser[15] at 671 nm. It is the source for the surrounding laser system (see Figure 6.5a) that basically consists of a locking part and a part where the light is distributed and switched. At the locking part of the laser system the light of the imaging laser is overlapped with light coming from the D2 master laser (see Figure 3.1) on a 50 : 50 beam splitter. At one of the splitter ports we can measure the absolute wavelength of the laser via a wavemeter[16], at the other port we place a photodiode[17]. It detects the beat signal between the two lasers and is connected to the electronic circuit that is sketched in Figure 6.5b. After two amplification stages the signal of the photodiode is compared to a reference signal coming from a signal generator[18] that is controlled by our experimental control software via VISA[19] commands. For the comparison we use a self-built digital PLL board (dPLL) that is based on the ADF4007 evaluation board[20] and inspired by [160]. The output is a TTL signal saying which frequency is higher. We use this signal as an error signal to lock our laser. At typical lock parameters we

[15] Toptica: DLpro
[16] Toptica: HF-Angstrom WS/6
[17] Hamamatsu: G4176-03
[18] Rhode & Schwarz: SMB100A
[19] Virtual Instrument Software Architecture
[20] Analog: UG-158

reach a long term[21] jitter of the photodiode frequency of $\pm 1.25\,\mathrm{MHz} \mathrel{\widehat{=}} \pm 0.21\,\Gamma$ with Γ being the transition linewidth.
By using a TTL signal with a clearly defined slope as an error signal, we can exploit that advantage and change the frequency difference between the lasers in the range of $\sim 50\,\mathrm{MHz}$ to $\sim 2.2\,\mathrm{GHz}$ during the lock[22]. The possible range is in our case limited by the photodiode electronics (Bias-Tee and the RF amplifiers).
In order to provide the possibility to image the atomic cloud from different directions (see Figure 6.6b), the light that is not needed for the offset lock is coupled into a fiber and propagates to an imaging distribution part on the laser table (see Figure 6.6a). Behind a DPAOM for a fine tuning and switching the light shares its path with light coming directly from the D2 master laser system (see Figure 3.1) that is used to image the atomic cloud on the MOT cooling transition (see Appendix B). By using half waveplates and PBSs, we distribute the light to a fiber that propagates the light to the science table for imaging the atoms along the wanted direction. All other fiber entries will be blocked by beam dumps during the run of the experiment.
The current magnifications for the different directions are given in Table 6.3.

TABLE 6.3: Magnification for the different imaging directions

name	**M**
MOTY	0.4
push	3.3
Towy	4.7
zimg	8.7

[21] 20 min

[22] If we want to flip the sign and go from a blue-detuned lock to a red-detuned lock, we need to invert the TTL signal. This is done in the DigiLock box.

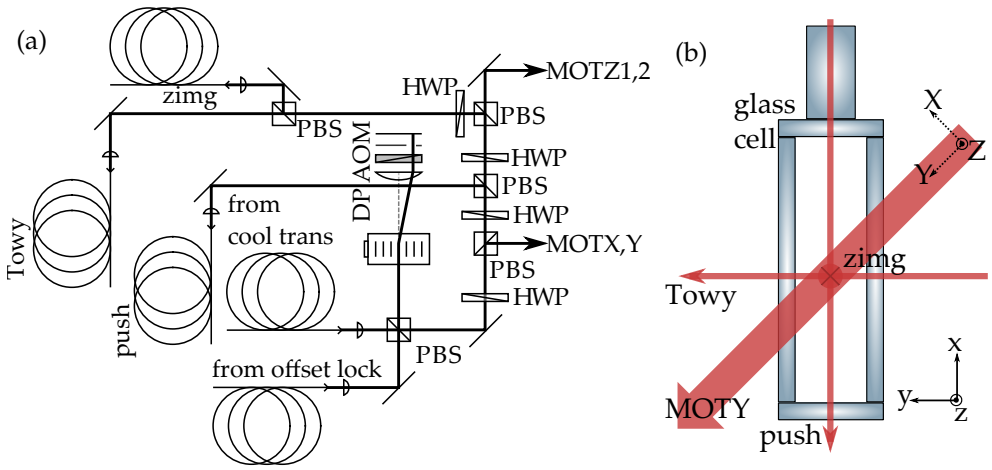

FIGURE 6.6: Sketch of the different imaging possibilities – (a) The laser system has two input fibers. One from the D2 master system (see Figure 3.1) called "cool trans" and one from the offset lock (see Figure 6.5a). The light from both fibers can be coupled into all four MOT fibers (*MOTZ1,2* and *MOTXY*) and into 3 auxiliary fibers (*Towy*, *zimg*, *push*). As a design library for drawing optics components the author used [85]. (b) The sketch shows different absorption imaging beams. In the experiment we use the beams *zimg*, *push* and *TowY* for the imaging of an ultracold gas. The *MOTY* beam is usually used for the imaging of laser cooled atomic clouds, e.g. for the ToF of an atomic cloud cooled in a gray molasses. The two coordinate systems show our general axes (xyz) and the MOT axes (XYZ). As a design library for drawing optics components the author used [104].

Chapter 7

Conclusion & Outlook

In this chapter, the author will first review the work of his thesis. Second, he identifies the main technical goals that need to be achieved on the way to future research topics. Third, some of these topics are discussed shortly.

7.1 Conclusion

During this PhD thesis, we built a modern and innovative machine that routinely allows the production of ultracold degenerate quantum gases of lithium and contains an objective with high numerical aperture that fulfills the requirements for quantum gas microscopy.
Starting from the construction, assembly and bake-out of a vacuum chamber, we decided for the unconventional but compact solution of a 2D-MOT as a suitable source for our 3D-MOT of lithium atoms that we tested successively to work for both stable isotopes. We further implemented a sub-Doppler laser-cooling mechanism, called gray molasses cooling, that allows significant loading of our far-detuned dipole trap. By exploiting the beneficial scattering properties of lithium atoms in high magnetic offset fields, we could evaporatively cool a cloud of fermionic lithium atoms, trapped all-optically by high power laser beams, to a Bose-Einstein condensate of molecules (mBEC). In order to prevent technical issues and for simplicity and compactness, we did not choose the common way of forcing the evaporation via an AOM but via a calibrated waveplate rotation.
In the following, we succesfully aligned a 1D optical accordion lattice onto the mBEC and manifested our control options for the dynamic control of the lattice spacing. We further showed that we can load the ultracold gas to a single slice of the lattice.
Moreover, we built the telescopes for the three laser beams of a 2D triangular lattice and aligned them onto the mBEC. We characterized the relative phase noise of the lattice beams and estimated its influence on a site resolved fluorescence image.
Via a decentered small lens at the backside of an objective with high numerical aperture, we found a way to operate our 3D-MOT and gray molasses cooling already at the focus of that objective. This idea supersedes any transport after the MOT and should be even applicable to the envisioned case where a second similar objective is inserted above the glass cell.
Moreover, we designed and characterized the imaging setup for a single site resolved fluorescence image of a 2D cloud of ultracold atoms pinned onto the lattice sites of our triangular lattice. Here, we simulated and measured the point spread function (PSF) that characterizes our imaging system. In this way, we can be sure that the small lens at the backside of the objective as well as a hole in a reflection mirror will not significantly change the expected image resolution.
In a nutshell, during this PhD thesis we developed a new ultracold quantum gas

machine that looks promising to become an agile quantum gas microscope that can be used for detailed simulations on quantum systems in the near future.

7.2 Outlook on future technical goals

Fluorescing atoms in the pinning lattice

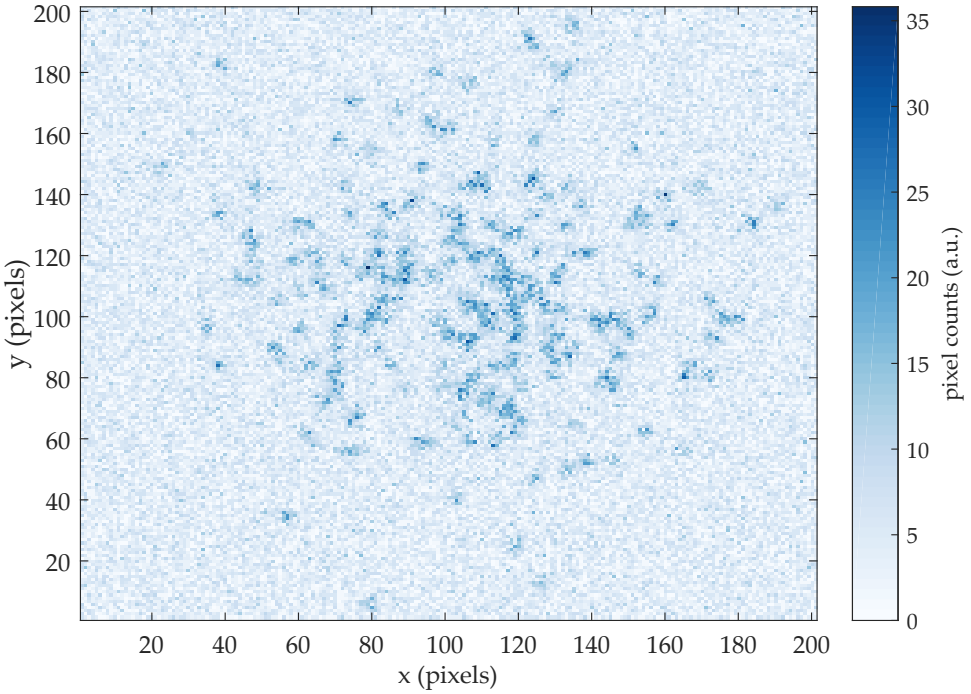

FIGURE 7.1: SIMULATED quantum gas microscope image of a dilute atomic cloud – For the image we fill a triangular lattice with our spacing of $a_{\mathrm{latt}} = 713\,\mathrm{nm}$. The atoms are randomly placed within a gaussian distribution that has a width of $12.8\,\mu\mathrm{m} \mathrel{\hat{=}} 64$ pixels and a centered maximum occupation probability of 40 %. The image has a magnification of $M = 80$ and a pixel size of $16\,\mu\mathrm{m}$. The number of fluorescence photons per atom is 150. For the point spread function, we consider a Rayleigh resolution of 820 nm and a gaussian distribution with a width of 100 nm as the position uncertainty of the atom on a lattice site. We allow 4 straylight photons per pixel and add shot noise. A detailed description and the MATLAB program for the simulation can be found in [161].

From the existing quantum gas microscopes [18–26] and from simulations [161] that we performed in our team (see Figure 7.1), we estimate the number of photons per atom that we need to collect on our camera chip is $\sim$ 150. Assuming a realistic collection efficiency of $\sim$ 5 % this implies that we want each atom to scatter $\sim 3\,000$ photons during our imaging process in $\lesssim 1\,\mathrm{s}$.
Up to now, the only proven way to obtain enough information for a single lattice site readout within our parameter range is to apply Raman sideband cooling (RSC) [20, 21, 47] that prevents the atoms from hopping to other lattice sites or from completely leaving the lattice. In order to improve the single site readout we will investigate the following topics:

- We will study alternative but promising ways of cooling ultracold lithium atoms in a deep pinning lattice. Here, we want to try out different gray molasses cooling scenarios that do not depend on resonances with the on-site trap frequency like it is the case for RSC and further try out RSC scenarios at high magnetic offset fields that could enhance the scattering rate due to anisotropic emission of fluorescence photons like in [158] and may be suited to a spin-selective cooling and imaging of the atoms.
- Advanced postprocessing of camera images may reduce the minimum number of photons per atom that is needed to declare a lattice site to be occupied or not. Here, modern deep learning readout techniques may help us to progress. They are currently studied in our team and elsewhere [162].
- When studying small quantum systems of ~ 10 atoms that have density structures that are on the scale of the lattice spacing, pinning will distort these density profiles. In a collaboration with the group of Peter Schmelcher and our principal investigator, Christof Weitenberg, a readout technique that reduces the distortion was prepared [163] and is ready to be implemented for future experiments.

Tailored potentials for small quantum systems

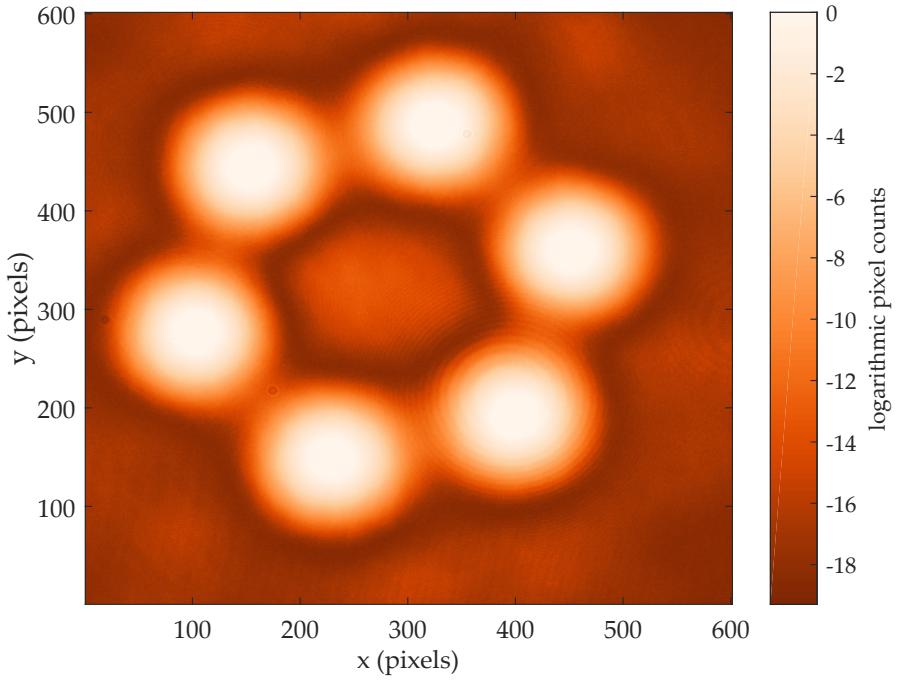

FIGURE 7.2: Holographic beam shapes – Intensity profile of a diffracted light beam at a Digital Mirror Device (DMD). For better visibility of experimental imperfections we chose a logarithmic color scale. The logarithmic pixel count is defined by $p_l = 10 \lg (p_c / p_{c,\max})$ where p_c is the number of counts and $p_{c,\max}$ is the maximum number of counts reached on a single pixel of the array. For a far red-detuned wavelength, the atoms can be loaded into the white maxima of the potential. Its geometry is similar to the molecular orbitals proposed for a quantum simulation in [164]. The data is taken from [165].

Since our goal is to study small quantum systems of $\sim 2-100$ atoms (see Chapter 7.3) the pancake shaped clouds in a slice of the accordion lattice (see Chapter 5.2) need to be further manipulated and loaded into well suited optically tailored micropotentials induced by light intensity profiles like e.g. shown in Figure 7.2.
In order to create such intensity profiles, we already implemented state-of-the-art holographic techniques[1] for spatial light modulation with a Digital Mirror Device (DMD, see Figure 7.3) in two Bachelor theses [165, 167] and have kind communications with the group of Henning Moritz at our institute who e.g. reported on a solution for the suppression of switching noise on DMDs [154].
As a next step, we will install the required laser system close to our atoms and use the high numerical aperture objective two focus the tailored dipole potentials onto the atoms.

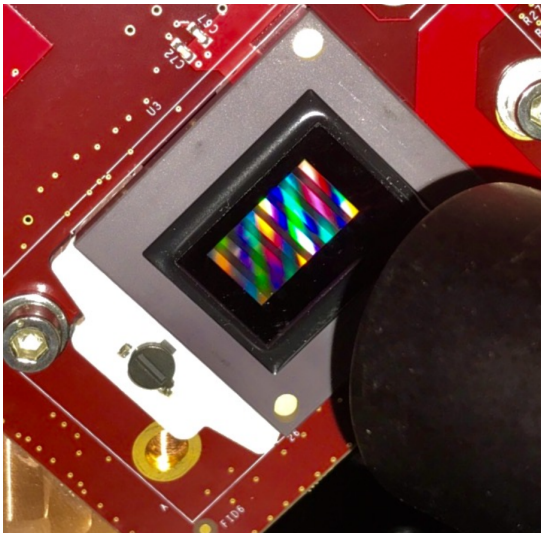

FIGURE 7.3: A smartphone image of the DMD and its surrounding – The actual DMD (Digital Mirror Device) with its small mirror pixels is shining multicolored like a grating. Its PCB (red) is in the background. A black tube (right edge of the image) surrounding the propagation direction of the diffracted laser light starts right behind the DMD. The image is taken from [165].

[1] A quick overview can e.g. found in [166].

7.3 Outlook on research topics

In the near future we mainly want to focus on the two following topics that both use mesoscopically sized systems with $\sim 2-100$ quantum particles in micro-potentials and that will extensively benefit from the technical possibilities of a quantum gas microscope.

Quantum simulation of attosecond science

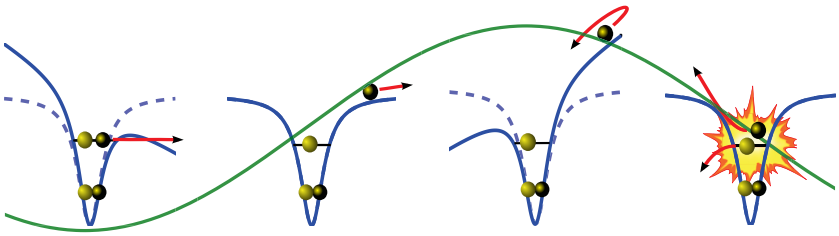

FIGURE 7.4: Illustration of a simulation for non-sequential double ionization (time evolves from left to right) – The total potential (blue) of a trap for 4 atoms in two different spin states (yellow, black) is realized by a dipole trap (dashed blue) and by an additional slowly oscillating magnetic gradient field (green). After tunneling through the potential barrier, the liberated atom is accelerated in the oscillating part of the potential and recollides with the left atoms such that finally two atoms leave the trap. Illustration taken from [79].

Electrons in atomic or molecular orbitals are trapped in potentials that are typically on the scale of the Bohr radius $a_o = 0.53$ Å and they move at the timescale of attoseconds. E.g. Bohr's orbital period of the electron in the hydrogen atom is

$$T_o = \frac{2\pi}{\hbar} m_e a_o^2 = 152\,\text{as}, \tag{7.1}$$

with m_e being the electron mass. In the field of attosecond science, people investigate the dynamics that happen on those scales by using atom-light interactions in the strong-field regime, i.e. the oscillating electric field of a short laser pulse deforms noticeably the static atomic potential for the electrons and induces additional dynamics [168].
Via a simulation with ultracold atoms, we can slow down and magnify selected effects and mechanisms that show up in attosecond science by orders of magnitude to the millisecond timescale and some microns for spatially tailored laser-induced dipole potentials (see Chapter 7.2).
Due to these advantages, the idea of building an "ultracold-atom quantum simulator for attosecond science" is recently proposed [79, 164] and a first experiment in that direction is performed [169] where a macroscopic ^{84}Sr BEC mimics the electron wave packet.
The quantum gas machine built during this PhD thesis allows to go beyond that wave packet analogy. We will simulate the effects of attosecond science based on a few-body ansatz. In our case, fermionic lithium atoms in a well-controlled optical potential will mimic the dynamics of electrons in an atomic or molecular orbital driven by an intense laser field. By additionally using quantum gas microscopy, this shall help us to gain experience and to benchmark theoretical concepts on interparticle correlations in those systems and how they behave in strong fields.

A first experiment that demonstrates our control options and the readout possibilities of a quantum gas microscope will be a simulation of a special case of non-sequential double ionization.
In attosecond science, this effect is often studied in a noble gas atom [170]. It is, in a first step singly ionized by a strong infrared laser field. The liberated electron then acts as an "atomic antenna" [171] that is accelerated in the laser field and absorbs its energy before recolliding with the mother ion such that finally two electrons are leaving the atomic potential.
In a simulation of this effect with ultracold but neutral lithium atoms (see Figure 7.4), we can freely tune the interactions of the colliding particles from repulsive to attractive by exploiting the broad Feshbach resonance [62]. Via spatial light modulation (see Chapter 7.2), we can tailor the underlying static potential for the colliding particles and the strong laser field can be mimicked either by an oscillating magnetic field or by another superposed dynamic light potential. In both cases, we can tune the oscillation frequency and so the pulse shape of the driving. Moreover, a dynamic movement of the superposed light potential in two dimensions would give rise to a simulation of an arbitrary time-dependent polarization of the strong laser field that of course includes the case of elliptic polarization like e.g. studied in [172] for the case of helium.
On top of all the degrees of freedom in quantum state engineering with ultracold atoms, quantum gas microscopy offers a extensive study of microscopic inter-particle correlations that appear when the liberated particle collides with the left particles in the mother potential.

Anyonic quantum particles

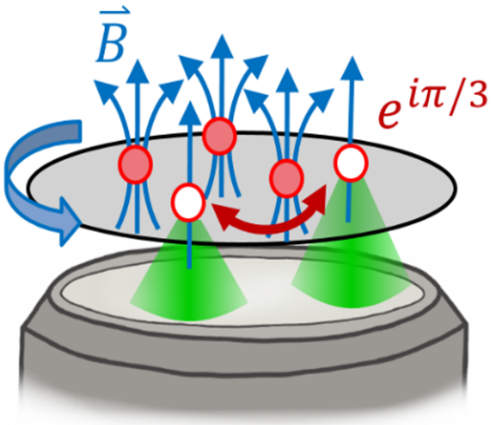

FIGURE 7.5: Illustration of anyonic quantum states above the microscope objective – An artificial magnetic field realized via rotation (light blue arrow) induces flux quanta (dark blue arrows) into the quantum system of a few particles (red circles). In the regime of fast rotation the number of flux quanta is comparable to the number of particles and the ground state of the system can be described with composites formed by particles and by a given number of flux quanta. Quasihole excitations (white circles with red frame) from such a ground state are believed to have anyonic properties, e.g. their statistic exchange phase may have a fraction of π, e.g. $\pi/3$. For our artificial systems the excitations can e.g. be induced by repulsive tweezers as indicated with green cones. The illustration is kindly provided by C. Weitenberg.

A quantum particle called "anyon" behaves statistically neither like a boson nor like a fermion that we know from textbook physics but like anything in between [173, 174]. By taking for simplicity the two-particle wave function of identical anyons

$$\Psi\left(\vec{r}_1, \vec{r}_2\right) \tag{7.2}$$

with $\vec{r}_i$ being the coordinate of the i^{th} particle, their interchange will multiply a phase factor to the wave function as

$$\Psi\left(\vec{r}_1, \vec{r}_2\right) = \Psi\left(\vec{r}_2, \vec{r}_1\right) \times \exp\left(i\theta\right) \tag{7.3}$$

with θ being the statistical phase lying in between the bosonic ($\theta = 0$) and the fermionic ($\theta = \pi$) limit.
The intriguing idea of anyons comes initially from a topological treatment of the configuration space with $d < 3$ dimensions for $N > 1$ identical quantum particles [173]. In condensed matter physics, anyons have established in a microscopic model for the fractional quantum Hall effect (FQHE) that is found in two-dimensional condensed matter systems [175]. Though, the understanding of the strongly-correlated states that come along with this model is still incomplete.
Unlike to charged electrons in solids our ultracold lithium atoms are neutral. Thus, we need to realize an artificial magnetic field for simulating fractional quantum Hall states. This will be done via trap rotation as e.g. reviewed in [176].
When mapping out the spatial correlations in a system with $N < 10$ atoms via quantum gas microscopy as illustrated in Figure 7.5, we expect to find vortices as flux quanta at rotation frequencies Ω that are moderate compared to the trap frequency, like it is e.g. observed in [177–180] for larger systems. At rotation frequencies close to the trap frequency, it is an interesting issue how the system evolves since especially for small atom numbers, the relative number of flux quanta per particle gets quickly close to 1, like e.g. reviewed in [181]. This situation is then strongly connected to the Chern-Simons gauge theories for anyons in the FQHE [182].
A first pioneering work in the direction of small atom numbers and fast rotation is performed in [183] where the trapping sites of a lattice are rotated and filled with a few bosonic atoms. However, a microscopic view as proposed in [184] on those systems with deterministic numbers of particles that may be bosonic or fermionic and that have tunable interaction will boost our experience on characterizing these exciting states of matter.

Appendix A

Digital AOM driver

Since there was need for an AOM driver that suits to the requirements of our novel apparatus, we revised the the soft- and hardware components that are used during the PhD thesis of D. Vogel [185] and developed a digital AOM driver. Here the author gives a short introduction into the use of the driver. He mainly focuses of using its lock program for a feedback control of the relative optical phase between two lattice beams.

A.1 Short introduction to DDS

What does digital mean?

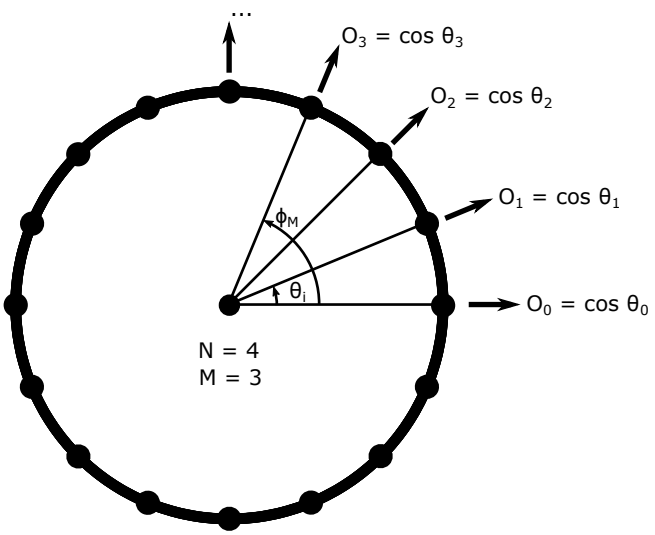

FIGURE A.1: The "phase wheel" picture of DDS – Here, we take the example for a look-up table of $2^N = 16$ data points, a jump size $M = 3$ and a cosine-form as the table output.

For our digital AOM driver (dAOM) we use Direct Digital Synthesis (DDS) for generating RF signals. As illustrated in Figure A.1 the essential working principle of DDS is described by a "phase wheel" that is a look-up table with periodic boundaries [186, 187]. It contains 2^N equiangular points placed on a circle at an angle θ_i and assigned to an output value O_i.
Along that wheel a DDS device performs phase jumps of

$$\phi_M = M \times \frac{2\pi}{2^N} \tag{A.1}$$

at every clock tick.
If now, the output value is defined to be $O_i \propto \cos(\theta_i)$, we get an output with a frequency

$$f_M = f_o \times \frac{M}{2^N} \tag{A.2}$$

with f_o being the clock frequency and M being the actual jump size that can be tuned by the user for changing the frequency f_M.
However, Equation A.2 only holds for at maximum to the so-called Nyquist limit of $M = 2^{N-1}$ where our cosine look-up table gives us a square wave output at a frequency $f_M = f_o/2$.
This is why at the output of our DDS device the signal passes through a low pass filter at $0.4\, f_o = 200\,\text{MHz}$. Such a filter smooths and hence cleans the Fourier transform of the signal. It additionally limits the given output power for a certain frequency (see Figure A.2).
To put it in a nutshell, digital means here that the underlying generation of the signal is digital because we use DDS[1] that works with a look-up table and discrete steps. But still, the output for $M \ll 2^N$ is a smooth cosine waveform.

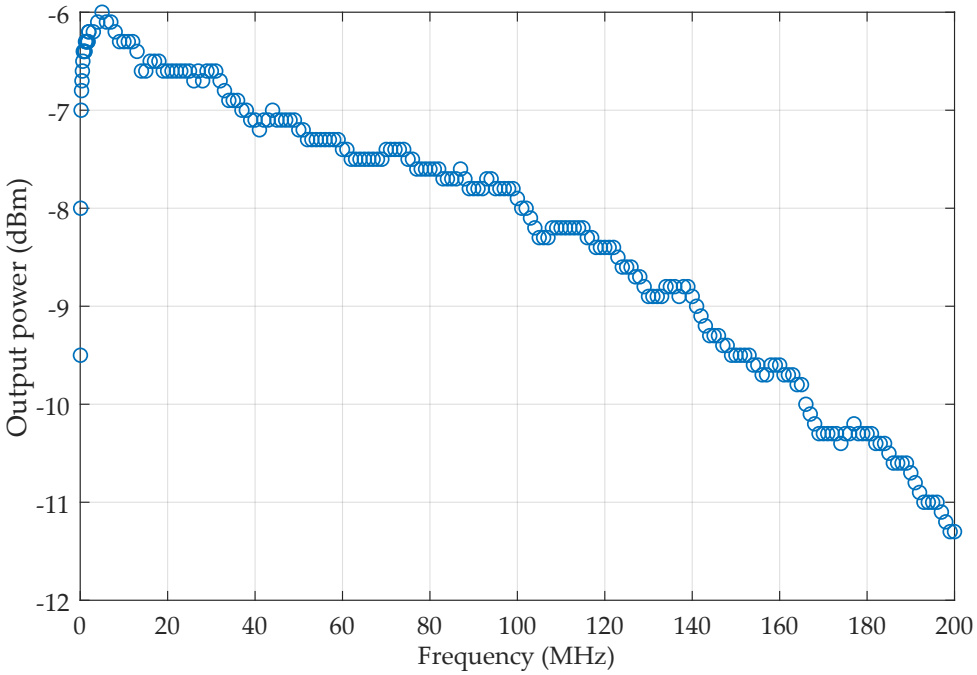

FIGURE A.2: Typical output power curve as a function of RF frequency for a dAOM channel.

Why digital?

Even if DDS based RF generation does not directly allow the usual signal control via an analog voltage and the bandwidth of the signal might be limited, there are many advantages, e.g.:

[1]Detailed information on DDS can e.g. be found online at the wikipage of Analog Devices: https://wiki.analog.com/university/courses/tutorials/index

- The stability of the RF on a DDS board is much less prone to unwanted drifts than e.g. on a voltage-controlled oscillator (VCO) since it only depends on the external clock.
- The dAOM has good phase noise characteristics by driving it with our external clock[2] (see Figure 5.12).
- The frequency calibration and synchronization of all dAOMs is automatically given when using the same external reference clock. This leads to a better handling of low frequency noise that arises when two RF signals are drifting at around the same frequency.
- The frequency of a dAOM is exactly programmable with a resolution of $f_o/2^N$ that is for our case $\sim$ 100 mHz. It takes much more effort to realize the same resolution with a VCO that we used before [69].
- There is no need for an external phase shifter. A phase change is easily programmed by an additional jump in the look-up table.
- We can switch off the RF signal completely with a command and thus there cannot be any leakage RF signal at the AOM like it is often the case when connecting a VCO with an external switch.

A.2 Short hardware overview

The hardware of the dAOM (see Figure A.3) mainly consists of a single-board computer, named BeagleBone[3], a DDS chip[4] and an analog-to-digital converter (ADC[5]) with the following main properties:

- Ethernet or USB connection for sending VISA commands from the experimental control
- 4 phase stable RF output channels with separately tunable frequency (32-bit)/ phase (14-bit)/ amplitude (10-bit)
- External clock input to minimize long term frequency drifts.
- Multipurpose analog input via a 14-bit analog-to-digital converter (ADC)
- Digital input/output (DI/O) for timing signals (trigger)
- Programmable arbitrary frequency/ amplitude/ phase ramps on two communicating programmable real-time units (PRUs[6]) that also can be used for lattice shaking in our group
- Possible analog modulation of frequency/ amplitude/ phase via the 14-bit ADC
- Available programs for a digital feedback control of frequency/ phase/ amplitude.

[2] SRS: FS725/3
[3] BeagleBoard.org: BeagleBone Black
[4] Analog Devices: AD9959, frequency/ phase/ amplitude at 32 bit/ 14 bit/ 10 bit.
[5] Analog Devices: LTC1419, 14 bit at $\pm$2.5V input voltage
[6] One program step takes usually 5 ns, only a few commands take slightly more time.

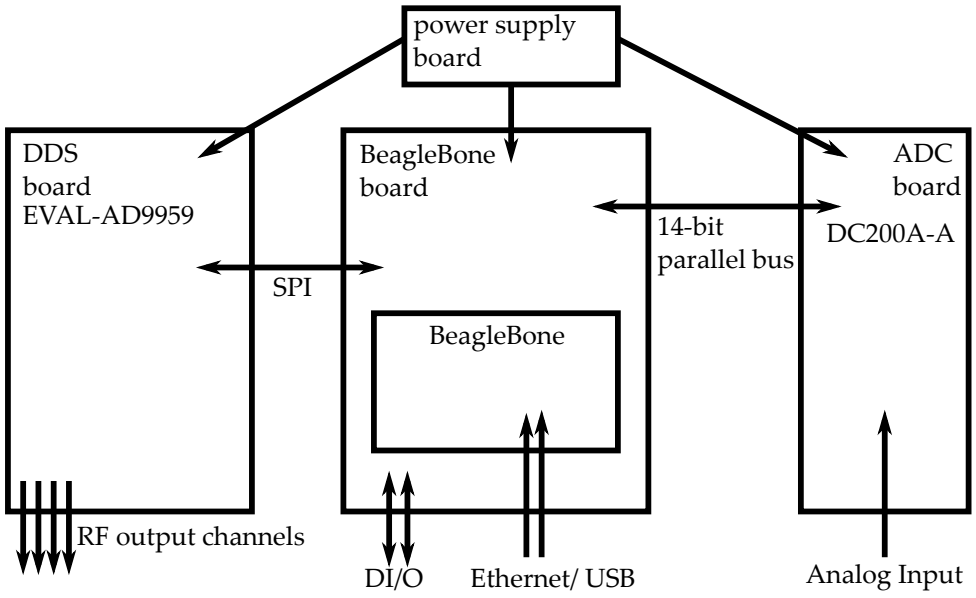

FIGURE A.3: A sketch of the dAOM hardware – The device has three main PCB boards supplied by a small power supply board that converts voltages and distributes the needed power. The control unit is a BeagleBone Black that is plugged on the BeagleBone board. Via Ethernet or USB, the BeagleBone is the interface for the user working on external software (MATLAB, Terminal, LabView, Cicero Word Generator, etc.). Additionally the user can get or send digital TTL signals for timing certain tasks in the experimental cycle (DI/O). The communication to the ADC board *DC200A-A* Analog Devices is provided by a 14-bit parallel bus. It has a $\pm 2.5\,\mathrm{V}$ analog input. The communication to the DDS evaluation board *EVAL-AD9959* from Analog Devices is provided via the SPI (Serial Peripheral Interface) pins. It has four phase stable RF output channels that can be separately tuned in phase, frequency and amplitude.

A.3 BeagleBone programming

The structure of the software environment is adopted from the basis work of Dominik Vogel [185]. Via an Ethernet or USB connection one can connect to the BeagleBone, i.e. it gets a local or a network IP address and we can access it via a TCP/IP socket.
The BeagleBone runs a standard Linux OS on its microprocessor (ARM) and we start the dAOM program from remote. On the ARM a C++ program manages the control and communication with the PRUs via a shared memory (see Figure A.4).
PRUs are needed for the transmission of execution commands for DDS in real-time but also for real-time processing of the ADC signal. Here, real-time means that a single command on a PRU is up to a few exceptions executed in exactly 1 PRU clock tick that takes 5 ns. The programming therefore needs to be very low-level assembler code (PASM [188]). The advantage of having two PRUs in the system gives us the possibility to parallelize certain jobs and to get shorter overall processing times. The communication of the two is realized via a scratchpad memory to which both have access (see Figure A.4).

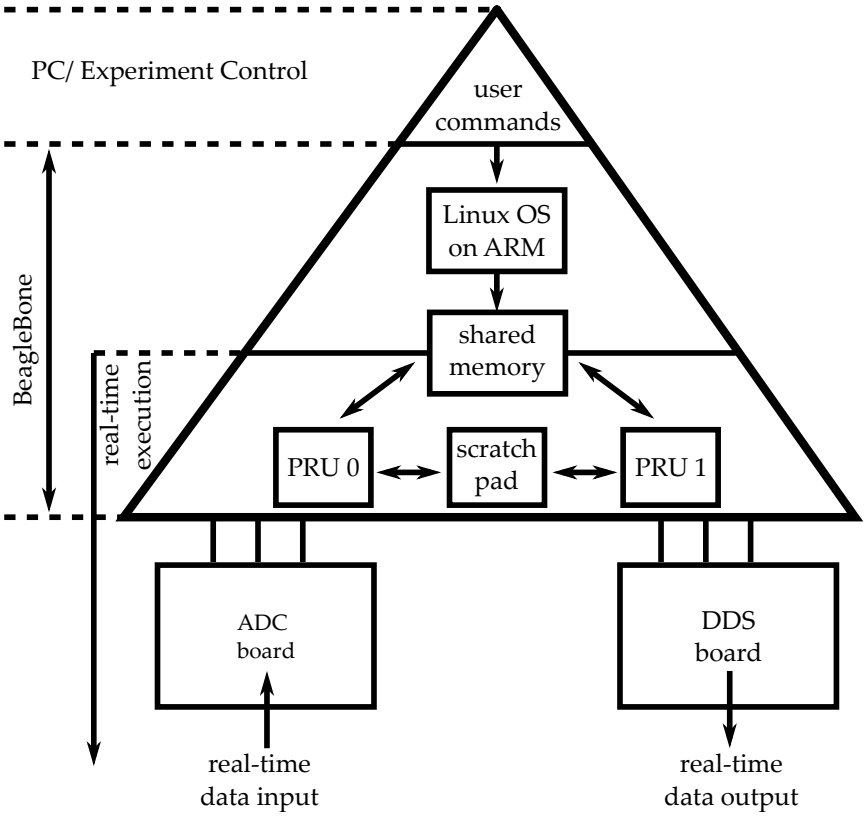

FIGURE A.4: A sketch of the constituents inside the BeagleBone – The BeagleBone works as a control interface that analyses and parses user commands into simple digital commands for the ADC/DDS board where the real-time data in-/output happens. The BeagleBone is easy accessible via a Linux OS on its ARM processor. Via a shared memory the ARM can store data for the two PRUs. For real-time synchronization the PRUs can communicate among each other via a scratch pad memory.

A.4 Example of a locking program

As soon as the main program is started on the ARM, it initiates the command interpretation for VISA commands from the user, it loads all modules where the commands are assigned to programs on the PRUs and it starts the communication management with the PRUs.
For the locking program the two PRUs, PRU 0 and PRU 1, synchronize their jobs via a predefined status register on the scratch pad (see Figure A.5). The idea is here that PRU 1 manages the ARM communication and the real-time calculation[7] of the error signal response whereas PRU 0 controls the ADC readout and the setting of new values on the DDS output.
All in all, the locking program is written in a general form that allows a locking of phase, frequency or amplitude. The only change is in the output command for the DDS and in the generation of the error signal at the input of the ADC.
For now, $\sim 70\,\%$ of the lock cycle time (see Figure A.6) is spent on the ADC readout that we set to 1.265 ms because of the ADC readout speed of 800 ks/s (status 1 in Figure A.5). Simultaneously, the user set PID parameters are loaded for every cycle. For the other $\sim 30\,\%$ of the lock cycle the error signal response is calculated, the DDS value is set and the program checks whether the user wants to exit the program. We

[7]The calculation is done by using a Z-transform for PID controlling with discrete time steps [189, 190].

can thus run through the lock cycle in a time of 1.810 ms which results in a frequency of $\sim$ 552 kHz that gives an upper bound for the bandwidth of the lock.

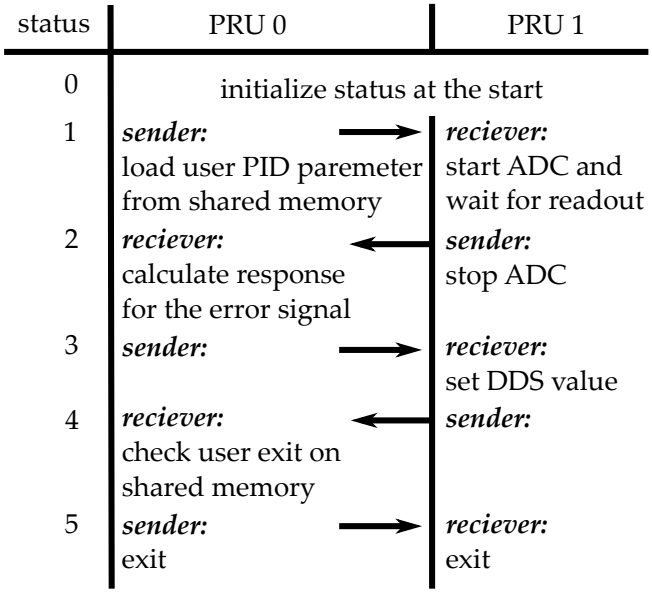

FIGURE A.5: Status of the locking program – The status of the lock program is stored in the scratch pad at any time of the execution. Within the lock the status is periodically changing between the numbers from 1 to 4 (lock cycle). In the status 1 and 2 both PRUs perform tasks. The status numbers 0/5 are the start and the exit information for the program.

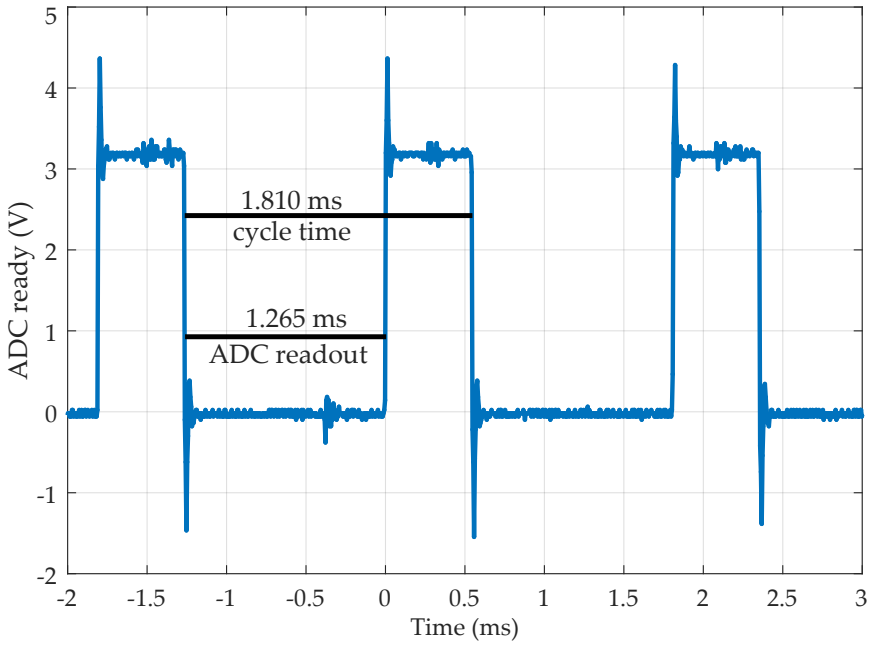

FIGURE A.6: Measuring the lock cycle time – For measuring the lock cycle time that we programmed, we put an oscilloscope at the ADC ready output pin that is low if the ADC is in readout mode and that is high if its idling. For well-defined PID parameter it is important that the cycle time is constant, meaning that the number of programmed commands is constant for all eventualities of e.g. an "if loop".

A.5 Error signal for phase locking

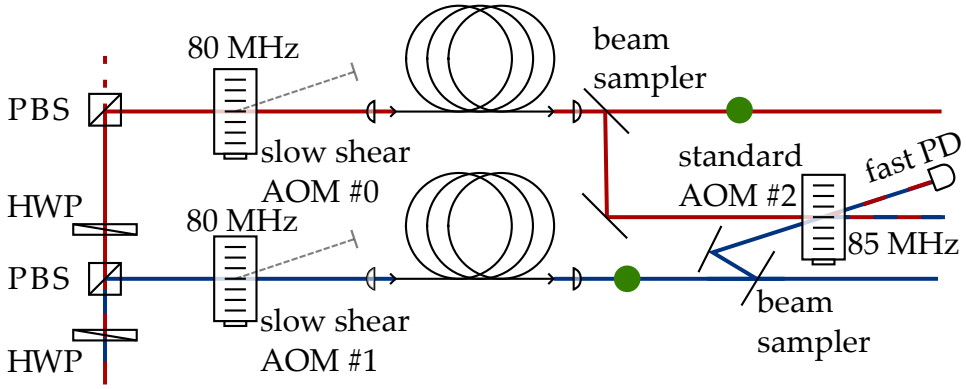

FIGURE A.7: A sketch of the setup for measuring the relative optical phase between two lattice beams – The beams are separated by a polarizing beam splitter and diffracted by slow shear AOMs where the 0^{th} order output goes under an angle of 6.45 ° with respect to the input beam and the 1^{st} order output goes parallel (±0.2 °). After propagating through separate fibers, a few percent of the laser beam power is picked up and coupled into a standard AOM. By coupling into the AOM at different input angles the laser beams can be overlapped again for the diffracted beams. In the direction for the 1^{st} diffraction order of the red beam and the 0^{th} order of the blue beam, we place a fast photodiode. The beat between the two beams is then at 85 MHz. Since all three AOMs are supplied from the same dAOM driver (see Figure A.8), the relative phase between the signals is constant and in good approximation the measured phase change of the beat corresponds to a relative phase change between the two light waves. The position for the atoms in both beams is indicated by a green dot. As a design library for drawing optics components the author used [85, 104].

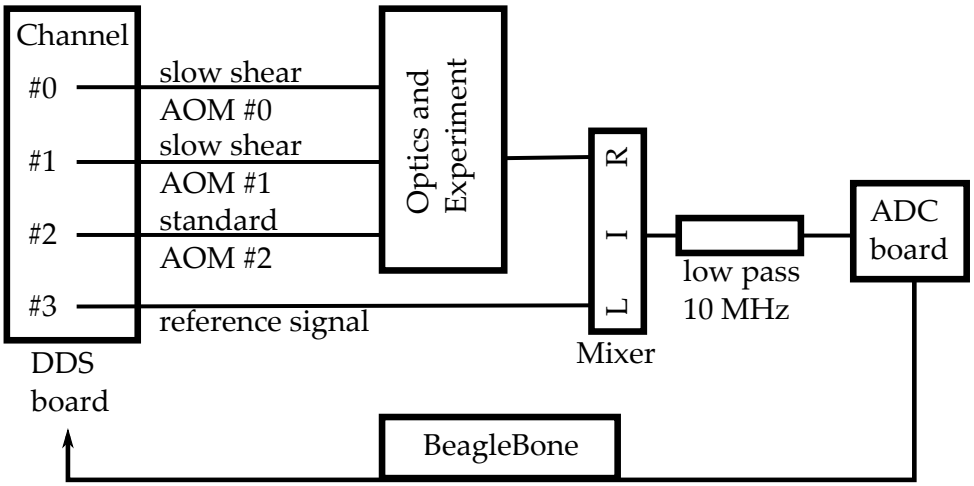

FIGURE A.8: A sketch of the electronics for the phase lock – All amplifying and attenuation stages are left out from the sketch. The first three channels of the DDS board are used for the AOMs from Figure A.7 and the fourth is used as a reference signal that is used for mixing the photodiode signal from 85 MHz down to DC. The DC phase signal is then fed into the ADC board that converts the signal for the BeagleBone. Here the PID response of the signal is calculated and a new command is send to the DDS board that changes the phase of channel #0.

For testing our phase lock program we built a test setup as sketched in Figure A.7.

Here, a light beam of our lattice laser system (see Chapter 5.1) is divided and coupled into two slow shear AOMs[8] at $\nu = 80\,\mathrm{MHz}$ for each of which the first diffraction order is coupled into a fiber. The output of the two fibers is then overlapped again by coupling both beams into a standard AOM[9] at $\nu_m = 85\,\mathrm{MHz}$. They are overlapped by shining one laser beam at the first order diffraction angle and the other at the zeroth order diffraction angle onto the AOM. Due to the frequency shift of the diffracted light, we observe a beat at ν_m on the photodiode[10] placed at one of the AOM outputs.
The beat at the photodiode changes phase when the relative phase between the two laser beams changes. This relative optical phase is the value we want to keep as constant as possible (see Chapter 5.3.3).
For the generation of an error signal (see Figure A.8), we mix down[11] our signal to DC via multiplying a reference signal at ν_m coming from the same DDS board as the driving signals for all three involved AOMs. In this way, all four RF signals are phase locked to each other. Finally after passing the signal from the mixer through a low pass filter[12], we insert our error signal into the ADC input of the dAOM. Here, finally the phase of the RF wave running through one of the slow shear AOMs is readjusted with respect to the relative optical phase.
The result of an active phase locking feedback is presented in Chapter 5 in Figure 5.12 and Table 5.3.

Short outlook

As stated in Chapter 5 there remains still the question of switching the lock. If we switch on the lock when the atoms are already loaded into the lattice there will be a short oscillation time where the lock controller needs to find the setpoint of the error signal. This oscillation significantly heats the sample. Even if we program the setpoint to the latest position of the phase we may run into trouble because the error signal of a mixer is $\propto \sin(\Delta\phi)$ and thus not an ideal bijective error function.
Instead of searching for a direct switching solution, the Spinor team in our group is currently working on a phase detector that outputs the same error signal for many orders of magnitude of lattice beam intensity. In this way, we can first lock the phase at an intensity that is out of relevance for atom trapping and then ramp up the lattice. Moreover, this solution will help to better separate the phase lock from a simultaneous intensity lock.

[8] Gooch and Housego: I-M080-32SG-3-LV11
[9] Gooch and Housego: AOMO-3080-197
[10] Hamamatsu: G7096-03
[11] minicircuits: ZRPD-1
[12] DC output of the ZFBT-6G from minicircuits

Appendix B

Relevant energy levels

hyperfine constants					
		value (MHz)			value (MHz)
^{6}Li	A_1	152.1	^{7}Li	A_4	401.7
	A_2	17.4		A_5	46.0
	A_3	-1.2		A_6	-3.1

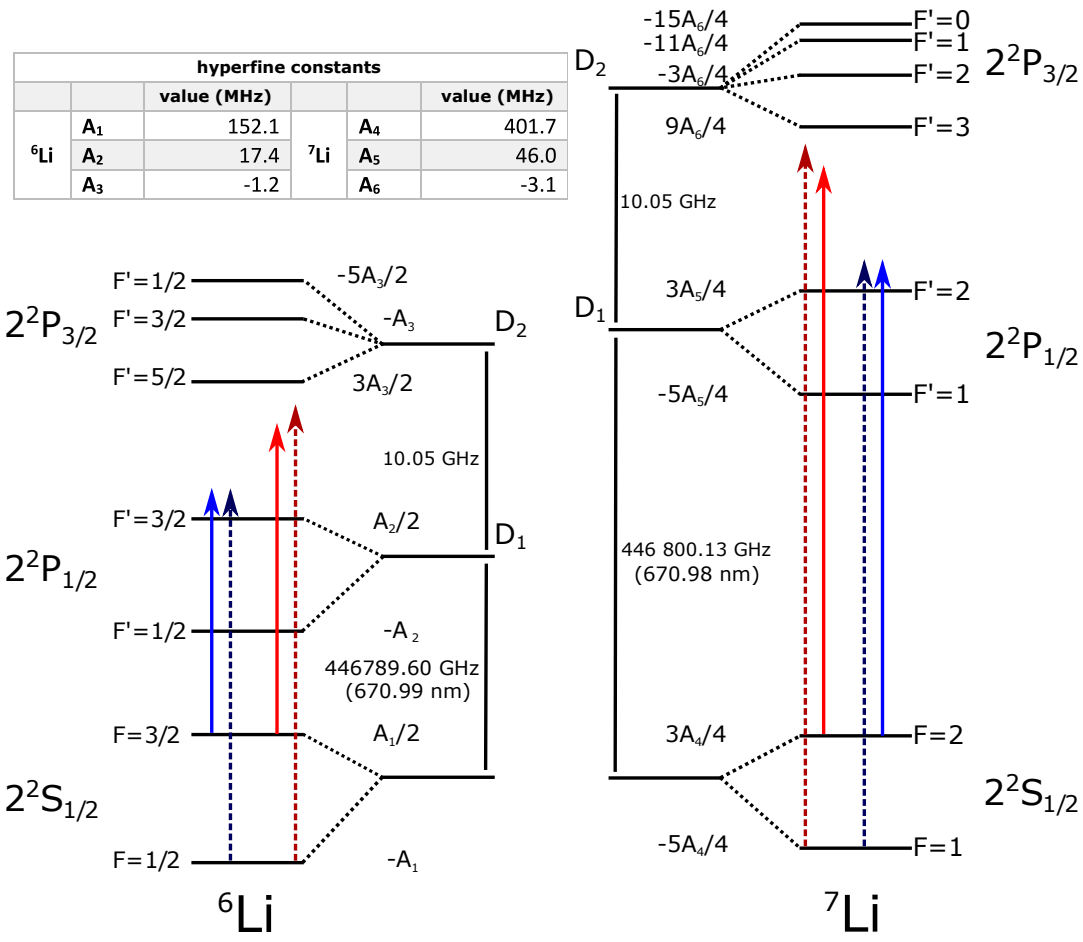

FIGURE B.1: Standard D-line level diagram of the two stable lithium isotopes ^{6,7}Li – The respective D2 line transitions (red arrows) are used in the red-detuned MOTs (2D-MOT, 3D-MOT). The respective D1 line transitions (blue arrows) are for a blue-detuned gray molasses cooling. The solid arrow lines corresponed to the respective cooling transitions whereas the dashed lines indicate the repumper transitions. The figure is taken from the author's Master's thesis [69].

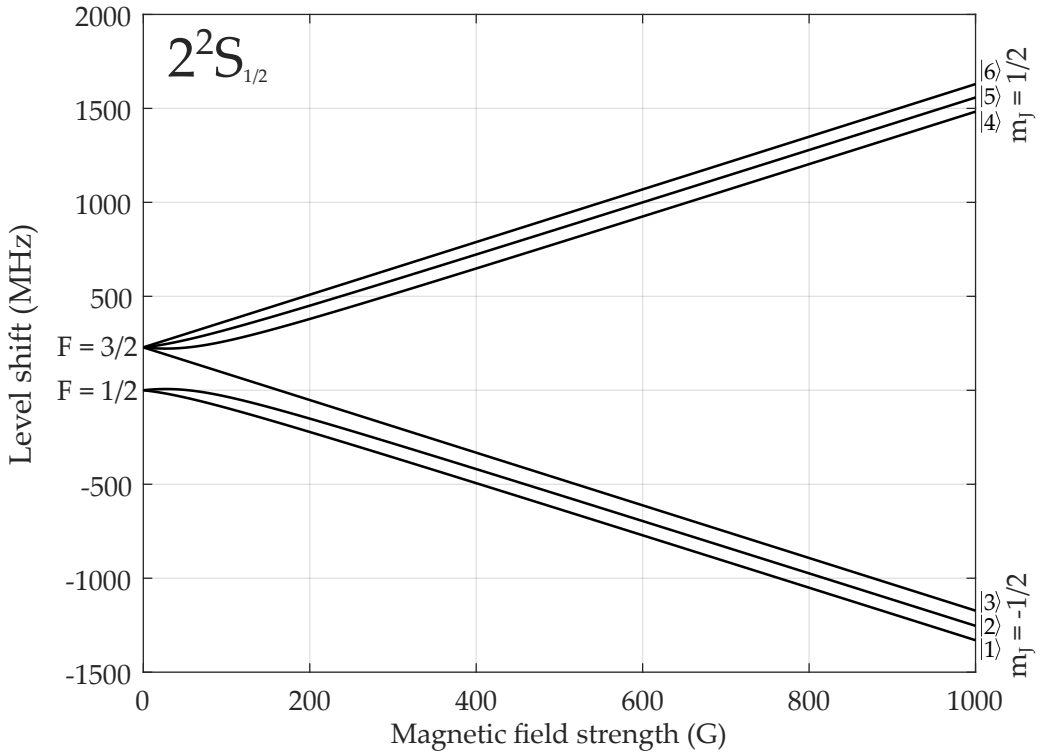

FIGURE B.2: Magnetic field dependence of the $2^2S_{1/2}$ ground state of ^{6}Li – Starting from the momentum basis with $F = 1/2, 3/2$ ^{6}Li enters the Paschen-Back regime at relatively low magnetic fields and the states regroup according to the m_J quantum number. They always regroup to subgroups of three lines because for ^{6}Li $I = 1$, i.e. $m_I = \pm 1, 0$. For the $2^2S_{1/2}$ ground state the energy difference within a subgroup is ~ 80 MHz. Typically all levels belonging to the $2^2S_{1/2}$ ground state are numbered in energetic order from $|1\rangle$ to $|6\rangle$. Data for the plot are taken from [157].

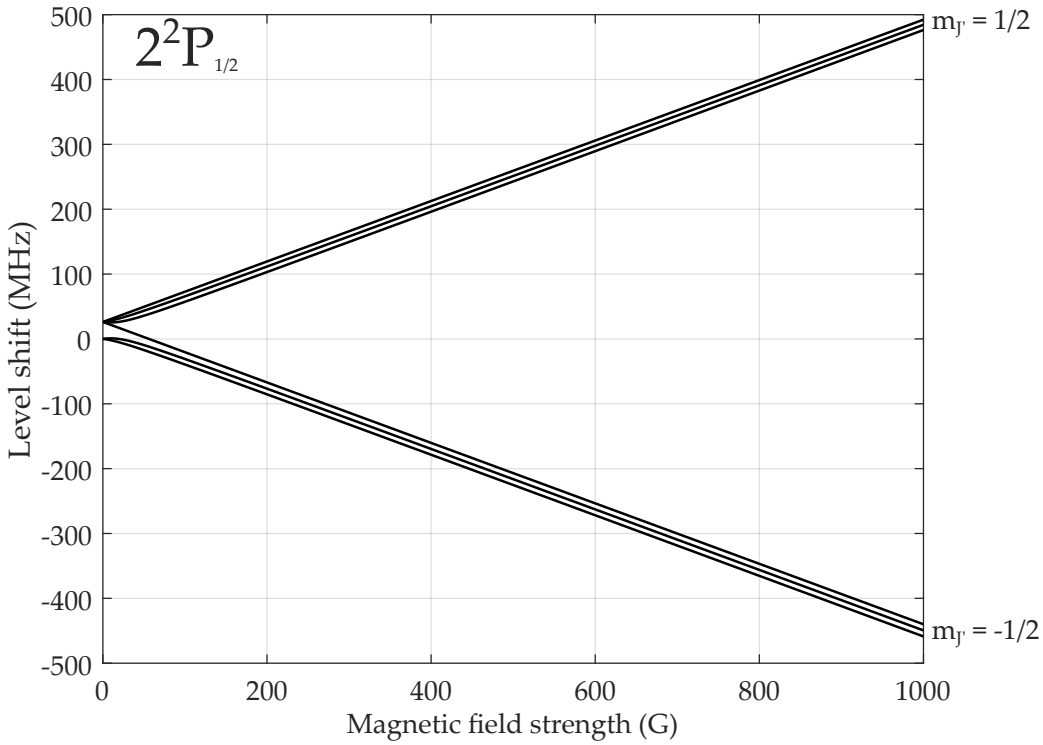

FIGURE B.3: Magnetic field dependence of the $2^2P_{1/2}$ excited state of ^{6}Li – In this excited state ^{6}Li enters the Paschen-Back regime at even lower magnetic fields than for the $2^2S_{1/2}$ ground state (see Figure B.2). The states regroup according to the $m_{J'}$ quantum number. They always regroup to subgroups of three lines because for ^{6}Li $I = 1$, i.e. $m_I = \pm 1, 0$. For the $2^2P_{1/2}$ ground state the energy difference within a m_I subgroup is on the order of ~ 10 MHz. Data for the plot are taken from [157].

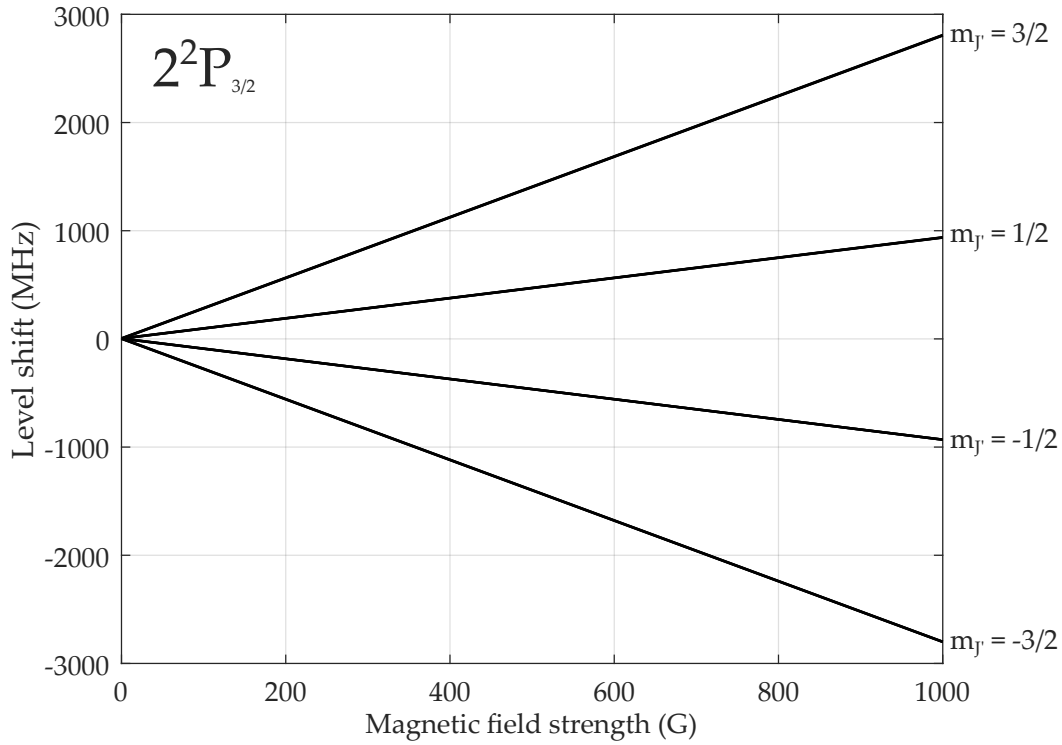

FIGURE B.4: Magnetic field dependence of the $2^2P_{3/2}$ excited state of ^{6}Li – In this excited state ^{6}Li enters the Paschen-Back regime at even lower magnetic fields than for the $2^2S_{1/2}$ ground state and the $2^2P_{1/2}$ excited state (see Figure B.2 and B.3). The states regroup according to the $m_{J'}$ quantum number. They always regroup to subgroups of three lines because for ^{6}Li $I = 1$, i.e. $m_I = \pm 1, 0$. For the $2^2P_{3/2}$ ground state the energy difference within a m_I subgroup is on the order of ~ 2 MHz. Data for the plot are taken from [157].

Appendix C

Interatomic scattering lengths

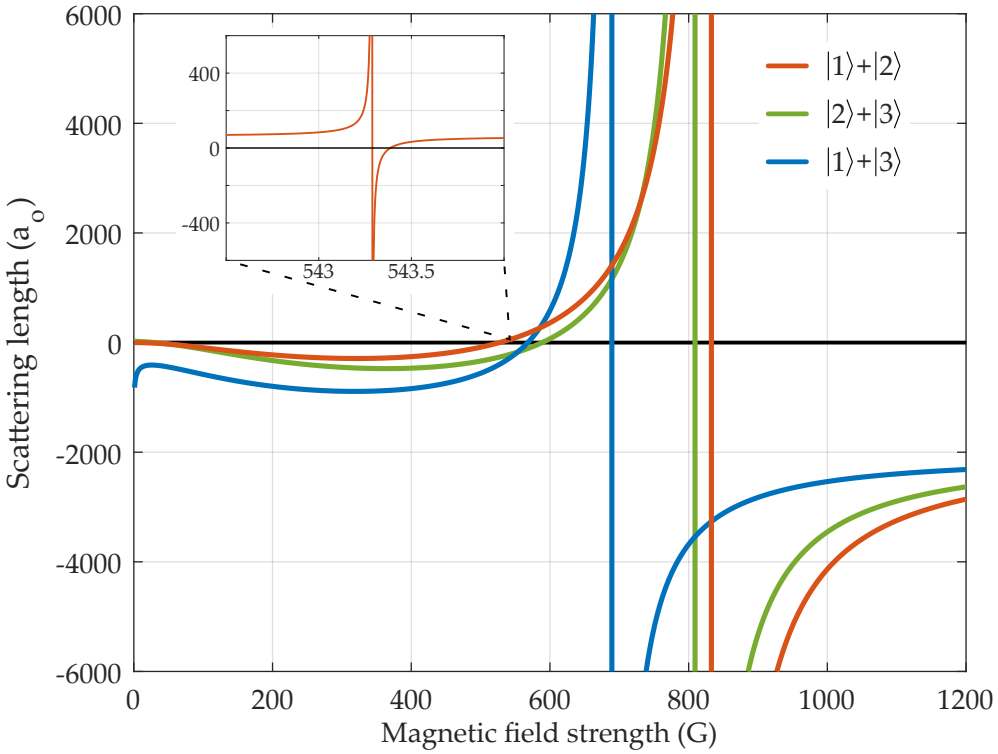

FIGURE C.1: Scattering length of the three lowest Paschen-Back states of ^{6}Li – The Feshbach resonances [62] between the states can be used to tune the interactions between ultracold atoms in the particular states (see Chapter 4.2). In the course of this thesis we especially use the broad resonance between $|1\rangle + |2\rangle$. For this combination of states – as shown in the inlet – there is a second tiny resonance at 543.286(3) G with a background scattering length of $\simeq 62\, a_o$ and a width of 0.10(1) G [191]. Further data for the curves are taken from the supplementary material of [192].

Appendix D

Intensity noise of the lattice laser

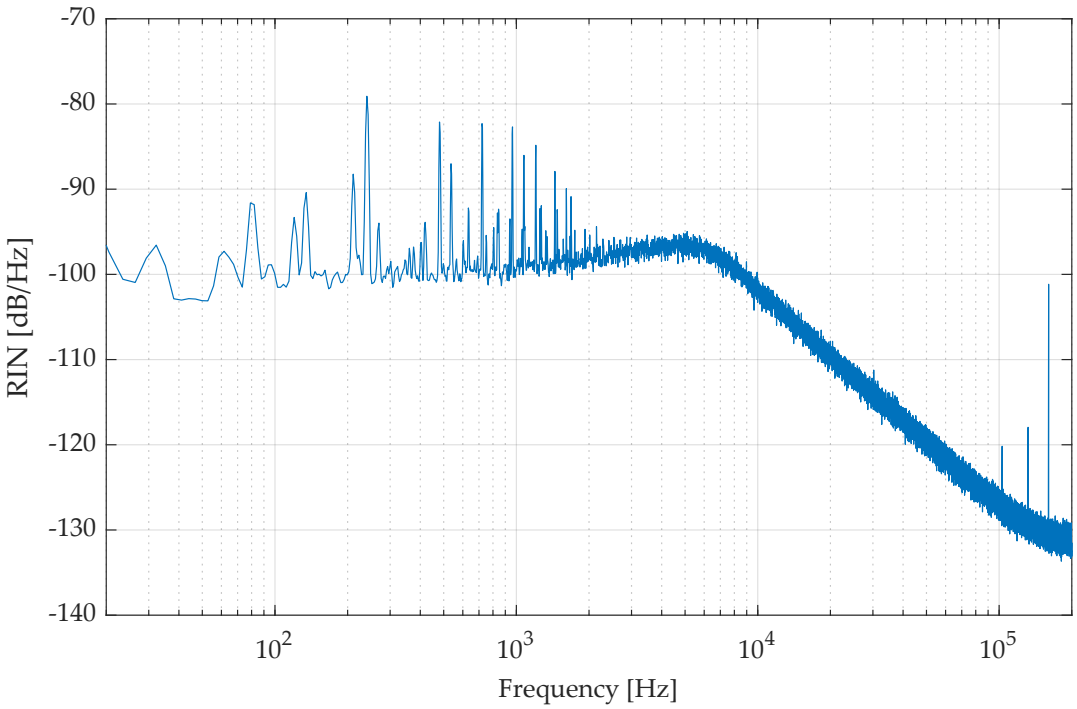

FIGURE D.1: Relative intensity noise of the lattice laser in dB/Hz behind all amplification stages measured at the photodiode shown in Figure 5.2. The measurement is performed by using an audio analyzer UPV from Rhode & Schwarz and is consistent with the data sheet but reveals higher resolution in frequency. During the measurement any external feedback control is switched off.

List of Abbreviations

1D	1-**D**imension(al)
2D	2-**D**imension(al)
3D	3-**D**imension(al)
AC	**A**lternating **C**urrent
ADC	**A**nalog-to-**D**igital **C**onverter
AI/O	**A**nalog **I**nput/**O**utput
AOM	**A**cousto-**O**ptic-**M**odulator
AR	**A**nti **R**eflective(-or)
ARM	**A**dvanced **R**ISC **M**achines (company)
BEC	**B**ose-**E**instein **C**ondensate
CAD	**C**omputer-**A**ided **D**esign
CCD	**C**harge-**C**oupled **D**evice
CF	**C**on**F**lat (brand name)
cMOT	**c**ompressed **M**agneto-**O**ptical **T**rap
D1	$2^2S_{1/2}$-$2^2P_{1/2}$ transition (see Appendix B)
D2	$2^2S_{1/2}$-$2^2P_{3/2}$ transition (see Appendix B)
DAC	**D**igital-to-**A**nalog **C**onverter
dAOM	**d**igital **A**cousto-**O**ptic-**M**odulator driver
DC	**D**irect **C**urrent
DDS	**D**irect **D**igital **S**ynthesis
DFB	**D**istributed **F**eed**B**ack
DI/O	**D**igital **I**nput/**O**utput
DMD	**D**igital **M**irror **D**evice
DN	**D**iametre **N**ormale (diameter)
DPAOM	**D**ouble-**P**ass **AOM**
dPLL	**d**igital **P**hase-**L**ocked **L**oop
DSUB	**D**-**S**ubminiature
ECDL	**E**xternal **C**avity **D**iode **L**aser
EOM	**E**lectro-**O**ptic **M**odulator
FPI	**F**abry-**P**érot-**I**nterferometer
FQHE	**F**ractional **Q**uantum **H**all **E**ffect
GUI	**G**raphical **U**ser **I**nterface
HR	**H**igh **R**eflective(-or)
HWP	**H**alf **W**ave**P**late
IGBT	**I**nsulated-**G**ate **B**ipolar **T**ransistor
IP	**I**nternet **P**rotocol
mBEC	**m**olecular **BEC**
MOT	**M**agneto-**O**ptical **T**rap
NA	**N**umerical **A**perture
OD	**O**ptical **D**ensity

OS	**O**perating **S**ystem
PBS	**P**olarizing **B**eam **S**plitter
PC	**P**ersonal **C**omputer
PD	**P**hoto**D**iode
PhD	**D**octor of **Ph**ilosophy
PID	**P**roportional **I**ntegral **D**erivative
PM	**P**olarization **M**aintaining
PRU	**P**rogrammable **R**ealtime **U**nit
PSF	**P**oint **S**pread **F**unction
PBS	**P**olarizing **B**eam **S**plitter
QWP	**Q**uarter **W**ave**P**late
RF	**R**adio **F**requency
RS-232	**R**ecommended **S**tandard **232**
RSC	**R**aman **S**ideband **C**ooling
SMA	**S**ub **M**iniature **A**
SPAOM	**S**ingle-**P**ass **AOM**
TCP	**T**ransmission **C**ontrol **P**rotocol
ToF	**T**ime-**o**f-**F**light
TTL	**T**ransistor-**T**ransistor **L**ogic
UHV	**U**ltra-**H**igh **V**acuum
UV	**U**ltra**V**iolet
VCO	**V**oltage-**C**ontrolled **O**scillator
VISA	**V**irtual **I**nstrument **S**oftware **A**rchitecture
VVA	**V**oltage-**V**ariable **A**ttenuator

Bibliography

[1] Richard P. Feynman. "Simulating physics with computers". In: *International Journal of Theoretical Physics* 21.6-7 (1982), pp. 467–488. DOI: 10.1007/bf02650179 (cit. on p. 1).

[2] Gordon E. Moore. "Cramming more components onto integrated circuits". In: *Electronics* 38.8 (1965), pp. 114–117 (cit. on p. 1).

[3] Jos Thijssen. *Computational Physics*. Cambridge University Press, 2007. ISBN: 0521833469 (cit. on p. 1).

[4] Yu. I. Manin. *Vychislimoe i nevychislimoe*. Kibernetika. "Sovet. Radio", Moscow, 1980, p. 128 (cit. on p. 1).

[5] Emily Grumbling and Mark Horowitz, eds. *Quantum Computing*. National Academies Press, 2019. DOI: 10.17226/25196 (cit. on p. 1).

[6] Michael A. Nielsen and Isaac L. Chuang. *Quantum Computation and Quantum Information: 10th Anniversary Edition*. Cambridge University Press, 2011. ISBN: 9781107002173 (cit. on p. 1).

[7] D. Deutsch and R. Jozsa. "Rapid Solution of Problems by Quantum Computation". In: *Proceedings of the Royal Society A: Mathematical, Physical and Engineering Sciences* 439.1907 (1992), pp. 553–558. DOI: 10.1098/rspa.1992.0167 (cit. on p. 1).

[8] Lov K. Grover. "A fast quantum mechanical algorithm for database search". In: *Proceedings of the twenty-eighth annual ACM symposium on Theory of computing - STOC 96*. ACM Press, 1996. DOI: 10.1145/237814.237866 (cit. on p. 1).

[9] Peter W. Shor. "Polynomial-Time Algorithms for Prime Factorization and Discrete Logarithms on a Quantum Computer". In: *SIAM Journal on Computing* 26.5 (1997), pp. 1484–1509. DOI: 10.1137/s0097539795293172 (cit. on p. 1).

[10] M. H. Anderson et al. "Observation of Bose-Einstein Condensation in a Dilute Atomic Vapor". In: *Science* 269.5221 (1995), pp. 198–201. DOI: 10.1126/science.269.5221.198 (cit. on p. 1).

[11] K. B. Davis et al. "Bose-Einstein Condensation in a Gas of Sodium Atoms". In: *Physical Review Letters* 75.22 (1995), pp. 3969–3973. DOI: 10.1103/physrevlett.75.3969 (cit. on p. 1).

[12] C. C. Bradley et al. "Evidence of Bose-Einstein Condensation in an Atomic Gas with Attractive Interactions". In: *Physical Review Letters* 75.9 (1995), pp. 1687–1690. DOI: 10.1103/physrevlett.75.1687 (cit. on p. 1).

[13] Maciej Lewenstein et al. "Ultracold atomic gases in optical lattices: mimicking condensed matter physics and beyond". In: *Advances in Physics* 56.2 (2007), pp. 243–379. DOI: 10.1080/00018730701223200 (cit. on p. 1).

[14] Immanuel Bloch, Jean Dalibard, and Wilhelm Zwerger. "Many-body physics with ultracold gases". In: *Reviews of Modern Physics* 80.3 (2008), pp. 885–964. DOI: 10.1103/revmodphys.80.885 (cit. on p. 1).

[15] Immanuel Bloch, Jean Dalibard, and Sylvain Nascimbène. "Quantum simulations with ultracold quantum gases". In: *Nature Physics* 8.4 (2012), pp. 267–276. DOI: 10.1038/nphys2259 (cit. on p. 1).

[16] Päivi Törmä and Klaus Sengstock. *Quantum Gas Experiments*. Imperial College Press, 2014. DOI: 10.1142/p945 (cit. on p. 1).

[17] Christian Gross and Immanuel Bloch. "Quantum simulations with ultracold atoms in optical lattices". In: *Science* 357.6355 (2017), pp. 995–1001. DOI: 10.1126/science.aal3837 (cit. on p. 1).

[18] Waseem S. Bakr et al. "A quantum gas microscope for detecting single atoms in a Hubbard-regime optical lattice". In: *Nature* 462 (2009), p. 74. DOI: 10.1038/nature08482 (cit. on pp. 2, 48, 70).

[19] Jacob F. Sherson et al. "Single-atom-resolved fluorescence imaging of an atomic Mott insulator". In: *Nature* 467 (2010), p. 68. DOI: 10.1038/nature09378 (cit. on pp. 2, 48, 70).

[20] Maxwell F. Parsons et al. "Site-Resolved Imaging of Fermionic ^{6}Li in an Optical Lattice". In: *Phys. Rev. Lett.* 114 (21 2015), p. 213002. DOI: 10.1103/PhysRevLett.114.213002 (cit. on pp. 2, 10, 39, 70).

[21] Ahmed Omran et al. "Microscopic Observation of Pauli Blocking in Degenerate Fermionic Lattice Gases". In: *Phys. Rev. Lett.* 115 (26 2015), p. 263001. DOI: 10.1103/PhysRevLett.115.263001 (cit. on pp. 2, 39, 70).

[22] Lawrence W. Cheuk et al. "Quantum-Gas Microscope for Fermionic Atoms". In: *Physical Review Letters* 114.19 (2015). DOI: 10.1103/physrevlett.114.193001 (cit. on pp. 2, 70).

[23] Elmar Haller et al. "Single-atom imaging of fermions in a quantum-gas microscope". In: *Nature Physics* 11.9 (2015), pp. 738–742. DOI: 10.1038/nphys3403 (cit. on pp. 2, 70).

[24] G. J. A. Edge et al. "Imaging and addressing of individual fermionic atoms in an optical lattice". In: *Physical Review A* 92.6 (2015). DOI: 10.1103/physreva.92.063406 (cit. on pp. 2, 70).

[25] Martin Miranda et al. "Site-resolved imaging of ytterbium atoms in a two-dimensional optical lattice". In: *Physical Review A* 91.6 (2015). DOI: 10.1103/physreva.91.063414 (cit. on pp. 2, 70).

[26] Ryuta Yamamoto et al. "An ytterbium quantum gas microscope with narrow-line laser cooling". In: *New Journal of Physics* 18.2 (2016), p. 023016. DOI: 10.1088/1367-2630/18/2/023016 (cit. on pp. 2, 70).

[27] J. Hubbard. "Electron correlations in narrow energy bands". In: *Proceedings of the Royal Society of London. Series A. Mathematical and Physical Sciences* 276.1365 (1963), pp. 238–257. DOI: 10.1098/rspa.1963.0204 (cit. on p. 2).

[28] H. A. Gersch and G. C. Knollman. "Quantum Cell Model for Bosons". In: *Physical Review* 129.2 (1963), pp. 959–967. DOI: 10.1103/physrev.129.959 (cit. on p. 2).

[29] W. S. Bakr et al. "Probing the Superfluid–to–Mott Insulator Transition at the Single-Atom Level". In: *Science* 329.5991 (2010), pp. 547–550. ISSN: 0036-8075. DOI: 10.1126/science.1192368 (cit. on pp. 2, 10).

[30] Martin Miranda et al. "Site-resolved imaging of a bosonic Mott insulator using ytterbium atoms". In: *Physical Review A* 96.4 (2017). DOI: 10.1103/physreva.96.043626 (cit. on p. 2).

[31] Daniel Greif et al. "Site-resolved imaging of a fermionic Mott insulator". In: *Science* 351.6276 (2016), pp. 953–957. ISSN: 0036-8075. DOI: 10.1126/science.aad9041 (cit. on pp. 2, 55).

[32] Lawrence W. Cheuk et al. "Observation of 2D Fermionic Mott Insulators ofK40with Single-Site Resolution". In: *Physical Review Letters* 116.23 (2016). DOI: 10.1103/physrevlett.116.235301 (cit. on p. 2).

[33] L. W. Cheuk et al. "Observation of spatial charge and spin correlations in the 2D Fermi-Hubbard model". In: *Science* 353.6305 (2016), pp. 1260–1264. DOI: 10.1126/science.aag3349 (cit. on p. 2).

[34] B Peaudecerf et al. "Microwave preparation of two-dimensional fermionic spin mixtures". In: *New Journal of Physics* 21.1 (2019), p. 013020. DOI: 10.1088/1367-2630/aafb89 (cit. on p. 2).

[35] M. Boll et al. "Spin- and density-resolved microscopy of antiferromagnetic correlations in Fermi-Hubbard chains". In: *Science* 353.6305 (2016), pp. 1257–1260. DOI: 10.1126/science.aag1635 (cit. on p. 2).

[36] Timon A. Hilker et al. "Revealing hidden antiferromagnetic correlations in doped Hubbard chains via string correlators". In: *Science* 357.6350 (2017), pp. 484–487. DOI: 10.1126/science.aam8990 (cit. on p. 2).

[37] Guillaume Salomon et al. "Direct observation of incommensurate magnetism in Hubbard chains". In: *Nature* 565.7737 (2018), pp. 56–60. DOI: 10.1038/s41586-018-0778-7 (cit. on p. 2).

[38] Christof Weitenberg et al. "Single-spin addressing in an atomic Mott insulator". In: *Nature* 471.7338 (2011), pp. 319–324. DOI: 10.1038/nature09827 (cit. on p. 2).

[39] Christof Weitenberg et al. "Coherent Light Scattering from a Two-Dimensional Mott Insulator". In: *Physical Review Letters* 106.21 (2011). DOI: 10.1103/physrevlett.106.215301 (cit. on p. 2).

[40] M. Endres et al. "Observation of Correlated Particle-Hole Pairs and String Order in Low-Dimensional Mott Insulators". In: *Science* 334.6053 (2011), pp. 200–203. DOI: 10.1126/science.1209284 (cit. on p. 2).

[41] Takeshi Fukuhara et al. "Microscopic observation of magnon bound states and their dynamics". In: *Nature* 502.7469 (2013), pp. 76–79. DOI: 10.1038/nature12541 (cit. on p. 2).

[42] Sebastian Hild et al. "Far-from-Equilibrium Spin Transport in Heisenberg Quantum Magnets". In: *Physical Review Letters* 113.14 (2014). DOI: 10.1103/physrevlett.113.147205 (cit. on p. 2).

[43] M. F. Parsons et al. "Site-resolved measurement of the spin-correlation function in the Fermi-Hubbard model". In: *Science* 353.6305 (2016), pp. 1253–1256. DOI: 10.1126/science.aag1430 (cit. on p. 2).

[44] Anton Mazurenko et al. "A cold-atom Fermi–Hubbard antiferromagnet". In: *Nature* 545.7655 (2017), pp. 462–466. DOI: 10.1038/nature22362 (cit. on p. 2).

[45] Jonathan Simon et al. "Quantum simulation of antiferromagnetic spin chains in an optical lattice". In: *Nature* 472.7343 (2011), pp. 307–312. DOI: 10.1038/nature09994 (cit. on p. 2).

[46] Ruichao Ma et al. "Photon-Assisted Tunneling in a Biased Strongly Correlated Bose Gas". In: *Physical Review Letters* 107.9 (2011). DOI: 10.1103/physrevlett.107.095301 (cit. on p. 2).

[47] Peter T. Brown et al. "Spin-imbalance in a 2D Fermi-Hubbard system". In: *Science* 357.6358 (2017), pp. 1385–1388. DOI: 10.1126/science.aam7838 (cit. on pp. 2, 70).

[48] P. M. Preiss et al. "Strongly correlated quantum walks in optical lattices". In: *Science* 347.6227 (2015), pp. 1229–1233. DOI: 10.1126/science.1260364 (cit. on p. 2).

[49] A. M. Kaufman et al. "Quantum thermalization through entanglement in an isolated many-body system". In: *Science* 353.6301 (2016), pp. 794–800. DOI: 10.1126/science.aaf6725 (cit. on p. 2).

[50] Alexander Lukin et al. "Probing entanglement in a many-body–localized system". In: *Science* 364.6437 (2019), pp. 256–260. ISSN: 0036-8075. DOI: 10.1126/science.aau0818 (cit. on p. 2).

[51] Matthew Rispoli et al. *Quantum critical behavior at the many-body-localization transition*. 2018. eprint: arXiv:1812.06959 (cit. on p. 2).

[52] Christie S. Chiu et al. "String patterns in the doped Hubbard model". In: *Science* 365.6450 (2019), pp. 251–256. DOI: 10.1126/science.aav3587 (cit. on p. 2).

[53] Johannes Zeiher et al. "Many-body interferometry of a Rydberg-dressed spin lattice". In: *Nature Physics* 12.12 (2016), pp. 1095–1099. DOI: 10.1038/nphys3835 (cit. on p. 2).

[54] Henrik P. Lüschen et al. "Single-Particle Mobility Edge in a One-Dimensional Quasiperiodic Optical Lattice". In: *Physical Review Letters* 120.16 (2018). DOI: 10.1103/physrevlett.120.160404 (cit. on p. 2).

[55] Matthew A. Nichols et al. "Spin transport in a Mott insulator of ultracold fermions". In: *Science* 363.6425 (2018), pp. 383–387. DOI: 10.1126/science.aat4387 (cit. on p. 2).

[56] C. Luciuk et al. "Observation of Quantum-Limited Spin Transport in Strongly Interacting Two-Dimensional Fermi Gases". In: *Physical Review Letters* 118.13 (2017). DOI: 10.1103/physrevlett.118.130405 (cit. on p. 2).

[57] Rhys Anderson et al. "Conductivity Spectrum of Ultracold Atoms in an Optical Lattice". In: *Physical Review Letters* 122.15 (2019). DOI: 10.1103/physrevlett.122.153602 (cit. on p. 2).

[58] Scott Smale et al. "Observation of a transition between dynamical phases in a quantum degenerate Fermi gas". In: *Science Advances* 5.8 (2019), eaax1568. DOI: 10.1126/sciadv.aax1568 (cit. on p. 2).

[59] Peter T. Brown et al. "Bad metallic transport in a cold atom Fermi-Hubbard system". In: *Science* 363.6425 (2018), pp. 379–382. DOI: 10.1126/science.aat4134 (cit. on p. 2).

[60] Elmer Guardado-Sanchez et al. *Subdiffusion and heat transport in a tilted 2D Fermi-Hubbard system*. 2019. eprint: arXiv:1909.05848 (cit. on p. 2).

[61] Herman Feshbach. "Unified theory of nuclear reactions". In: *Annals of Physics* 5.4 (1958), pp. 357–390. DOI: 10.1016/0003-4916(58)90007-1 (cit. on p. 2).

[62] Cheng Chin et al. "Feshbach resonances in ultracold gases". In: *Rev. Mod. Phys.* 82 (2 2010), pp. 1225–1286. DOI: 10.1103/RevModPhys.82.1225 (cit. on pp. 2, 14, 31, 35, 64, 74, 89).

[63] Debayan Mitra et al. "Quantum gas microscopy of an attractive Fermi-Hubbard system". In: *Nature Physics* 14 (2017). Article, p. 173 (cit. on pp. 2, 39, 48).

[64] Marcel Bankau. "Saturated Absorption Spectroscopy and Design of an Ultra-High-Vacuum Chamber for a Lithium Quantum Gas Experiment". Bachelor's thesis. Universität Hamburg, 2014 (cit. on pp. 6, 7).

[65] Claudiu Andrei Stan. "Experiments with Interacting Bose and Fermi Gases". PhD thesis. Massachusetts Institute of Technology, 2005 (cit. on pp. 6, 9).

[66] Tobias Tiecke et al. "High-flux two-dimensional magneto-optical-trap source for cold lithium atoms". In: *Physical Review A* 80 (2009), pp. 13409–. DOI: 10.1103/PhysRevA.80.013409 (cit. on p. 6).

[67] Silke Ospelkaus. "Quantum Degenerate Fermi-Bose Mixtures of ^{40}K and ^{87}Rb in 3D Optical Lattices". PhD thesis. Universität Hamburg, 2006 (cit. on p. 6).

[68] Malte Hagemann. "Aufbau und Charakterisierung einer Lithium-MOT". Bachelor's thesis. Universität Hamburg, 2017 (cit. on pp. 7, 25).

[69] Andreas Kerkmann. "Ein Lasersystem zum Fangen und Kühlen von bosonischem und fermionischem Lithium". Master's thesis. Universität Hamburg, 2015 (cit. on pp. 7, 10, 21, 23, 24, 29, 30, 79, 85).

[70] Kurt Kolasinski. *Surface science : foundations of catalysis and nanoscience*. Chichester, West Sussex, United Kingdom: Wiley, 2012. ISBN: 978-1-119-99036-9 (cit. on p. 7).

[71] Tobias G Tiecke. "Feshbach resonances in ultracold mixtures of the fermionic quantum gases ^{6}Li and ^{40}K". PhD thesis. University of Amsterdam, 2009 (cit. on p. 8).

[72] C. B. Alcock, V. P. Itkin, and M. K. Horrigan. "Vapour Pressure Equations for the Metallic Elements: 298–2500K". In: *Canadian Metallurgical Quarterly* 23.3 (1984), pp. 309–313. DOI: 10.1179/cmq.1984.23.3.309 (cit. on p. 8).

[73] Jeppson D.W. et al. *Lithium literature review: lithium's properties and interactions*. Tech. rep. Hanford Engineering Development Laboratory, 1978 (cit. on p. 8).

[74] Ahmed Omran. "A microscope for Fermi gases". PhD thesis. LMU München, 2016 (cit. on pp. 10, 39, 48, 51).

[75] Matthias Kohnen. "Ultracold Fermi Mixtures in an Optical Dipole Trap". Diploma's thesis. Universität Heidelberg, 2008 (cit. on p. 10).

[76] Michael Hagemann. "Magnetfeldspulen und ein Interferometer für ein Quantengasmikroskop mit Lithiumatomen". Master's thesis. Universität Hamburg, 2016 (cit. on pp. 10, 14, 15, 31).

[77] Maxwell F. Parsons. "Probing the Hubbard model with single-site resolution". PhD thesis. Harvard University, 2016 (cit. on pp. 14, 48, 51).

[78] F. Serwane et al. "Deterministic Preparation of a Tunable Few-Fermion System". In: *Science* 332.6027 (2011), pp. 336–338. ISSN: 0036-8075. DOI: 10.1126/science.1201351 (cit. on p. 14).

[79] Simon Sala, Johann Förster, and Alejandro Saenz. "Ultracold-atom quantum simulator for attosecond science". In: *Phys. Rev. A* 95 (1 2017), p. 011403. DOI: 10.1103/PhysRevA.95.011403 (cit. on pp. 14, 73).

[80] Debayan Mitra. "Exploring attractively interacting fermions in 2D using a quantum gas microscope". PhD thesis. Princeton University, 2018 (cit. on pp. 16, 48, 51, 55).

[81] J. L. Ville et al. "Loading and compression of a single two-dimensional Bose gas in an optical accordion". In: *Phys. Rev. A* 95 (1 2017), p. 013632. DOI: 10.1103/PhysRevA.95.013632 (cit. on pp. 17, 40, 42, 44).

[82] Debayan Mitra et al. "Phase Separation and Pair Condensation in a Spin-Imbalanced 2D Fermi Gas". In: *Phys. Rev. Lett.* 117 (9 2016), p. 093601. DOI: 10.1103/PhysRevLett.117.093601 (cit. on pp. 17, 40).

[83] Aviv Keshet and Wolfgang Ketterle. "A distributed, graphical user interface based, computer control system for atomic physics experiments". In: *Review of Scientific Instruments* 84.1 (2013), p. 015105. DOI: 10.1063/1.4773536 (cit. on p. 18).

[84] Niels-Ole Rohweder. "Developing a modular camera program for quantum gas experiments". Bachelor's thesis. Universität Hamburg, 2014 (cit. on p. 19).

[85] Florian G. Huber. "Site-Resolved Imaging with the Fermi Gas Microscope". PhD thesis. Harvard University, 2014 (cit. on pp. 22, 23, 49, 65, 67, 83).

[86] D. J. McCarron, S. A. King, and S. L. Cornish. "Modulation transfer spectroscopy in atomic rubidium". In: *Measurement Science and Technology* 19.10 (2008), p. 105601. DOI: 10.1088/0957-0233/19/10/105601 (cit. on p. 23).

[87] J. Grünert and A. Hemmerich. "Optimizing the production of metastable calcium atoms in a magneto-optical trap". In: *Applied Physics B* 73.8 (2001), pp. 815–818. ISSN: 1432-0649. DOI: 10.1007/s003400100768 (cit. on p. 25).

[88] M. S. Shahriar et al. "Continuous polarization-gradient precooling-assisted velocity-selective coherent population trapping". In: *Physical Review A* 48.6 (1993), R4035–R4038. DOI: 10.1103/physreva.48.r4035 (cit. on p. 26).

[89] M. Weidemüller et al. "A Novel Scheme for Efficient Cooling below the Photon Recoil Limit". In: *Europhysics Letters (EPL)* 27.2 (1994), pp. 109–114. DOI: 10.1209/0295-5075/27/2/006 (cit. on p. 26).

[90] D. Boiron et al. "Three-dimensional cooling of cesium atoms in four-beam gray optical molasses". In: *Physical Review A* 52.5 (1995), R3425–R3428. DOI: 10.1103/physreva.52.r3425 (cit. on p. 26).

[91] D. Boiron et al. "Laser cooling of cesium atoms in gray optical molasses down to 1.1 μK". In: *Physical Review A* 53.6 (1996), R3734–R3737. DOI: 10.1103/physreva.53.r3734 (cit. on p. 26).

[92] D. Rio Fernandes et al. "Sub-Doppler laser cooling of fermionic40K atoms in three-dimensional gray optical molasses". In: *EPL (Europhysics Letters)* 100.6 (2012), p. 63001. DOI: 10.1209/0295-5075/100/63001 (cit. on p. 26).

[93] Andrew T. Grier et al. "Λ-enhanced sub-Doppler cooling of lithium atoms in D_1 gray molasses". In: *Phys. Rev. A* 87 (6 2013), p. 063411. DOI: 10.1103/PhysRevA.87.063411 (cit. on pp. 26, 27, 29).

[94] Franz Sievers et al. "Simultaneous sub-Doppler laser cooling of fermionic ^{6}Li and ^{40}K on the D_1 line: Theory and experiment". In: *Phys. Rev. A* 91 (2 2015), p. 023426. DOI: 10.1103/PhysRevA.91.023426 (cit. on p. 26).

[95] E. Arimondo. "V Coherent Population Trapping in Laser Spectroscopy". In: *Progress in Optics*. Elsevier, 1996, pp. 257–354. DOI: 10.1016/s0079-6638(08)70531-6 (cit. on p. 27).

[96] Manuel Gerken. "Gray Molasses Cooling of Lithium-6 Towards a Degenerate Fermi Gas". Master's thesis. Universität Heidelberg, 2016 (cit. on p. 27).

[97] Jan Mika Jacobsen. "Setup of a Laser Spectroscopy of Lithium and Characterization of Electro-Optic Modulators". Bachelor's thesis. Universität Hamburg, 2015 (cit. on pp. 29, 58).

[98] Marlan O. Scully and M. Suhail Zubairy. *Quantum Optics*. 6th ed. Cambridge: Cambridge University Press, 1997. ISBN: 978-0-521-43595-6 (cit. on p. 29).

[99] A. Burchianti et al. "Efficient all-optical production of large ^{6}Li quantum gases using D_1 gray-molasses cooling". In: *Phys. Rev. A* 90 (4 2014), p. 043408. DOI: 10.1103/PhysRevA.90.043408 (cit. on p. 29).

[100] S. Jochim. "Bose-Einstein Condensation of Molecules". In: *Science* 302.5653 (2003), pp. 2101–2103. DOI: 10.1126/science.1093280 (cit. on pp. 31, 34, 35).

[101] M. W. Zwierlein et al. "Observation of Bose-Einstein Condensation of Molecules". In: *Physical Review Letters* 91.25 (2003). DOI: 10.1103/physrevlett.91.250401 (cit. on pp. 31, 34, 35).

[102] T. Bourdel et al. "Experimental Study of the BEC-BCS Crossover Region in Lithium 6". In: *Physical Review Letters* 93.5 (2004). DOI: 10.1103/physrevlett.93.050401 (cit. on pp. 31, 34, 35).

[103] Mathis Samuel Fischer. "An Optical Dipole Trap and an Accordion Lattice for a Quantum Gas Microscope". Master's thesis. Universität Hamburg, 2018 (cit. on pp. 31, 33, 34, 36, 37, 39, 41, 42, 45, 60).

[104] Alexander Franzen. "ComponentLibrary". In: gwoptics.org (cit. on pp. 32, 65, 67, 83).

[105] Hauke Schmidt. "Dynamic Control of the Geometry of optical Lattices". Bachelor's thesis. Universität Hamburg, 2015 (cit. on p. 33).

[106] Yann Hendrick Kiefer. "Aufbau und Planung einer Intsitätskontrolle für eine Dipolfalle zur evaporativen Kühlung von Lithiumatomen". Bachelor's thesis. Universität Hamburg, 2016 (cit. on p. 33).

[107] M. S. Safronova, U. I. Safronova, and Charles W. Clark. "Magic wavelengths for optical cooling and trapping of lithium". In: *Phys. Rev. A* 86 (4 2012), p. 042505. DOI: 10.1103/PhysRevA.86.042505 (cit. on pp. 34, 37, 39).

[108] Cheng Chin et al. "Feshbach resonances in ultracold gases". In: *Rev. Mod. Phys.* 82 (2 2010), pp. 1225–1286. DOI: 10.1103/RevModPhys.82.1225 (cit. on p. 35).

[109] G. Zürn et al. "Precise Characterization of ^{6}Li Feshbach Resonances Using Trap-Sideband-Resolved RF Spectroscopy of Weakly Bound Molecules". In: *Phys. Rev. Lett.* 110 (13 2013), p. 135301. DOI: 10.1103/PhysRevLett.110.135301 (cit. on p. 35).

[110] Wilhelm Zwerger. *The BCS-BEC Crossover and the Unitary Fermi Gas*. Berlin Heidelberg: Springer Science & Business Media, 2011. ISBN: 978-3-642-21977-1 (cit. on p. 35).

[111] Cheng Chin and Rudolf Grimm. "Thermal equilibrium and efficient evaporation of an ultracold atom-molecule mixture". In: *Phys. Rev. A* 69 (3 2004), p. 033612. DOI: 10.1103/PhysRevA.69.033612 (cit. on p. 35).

[112] W. Ketterle, D. S. Durfee, and D. M. Stamper-Kurn. "Making, probing and understanding Bose-Einstein condensates". In: *Proc. of the International School of Physics 'Enrico Fermi'* 140 (1999), pp. 67–176. DOI: 10.3254/978-1-61499-225-7-67 (cit. on p. 35).

[113] G. E. Astrakharchik et al. "Momentum Distribution and Condensate Fraction of a Fermion Gas in the BCS-BEC Crossover". In: *Phys. Rev. Lett.* 95 (23 2005), p. 230405. DOI: 10.1103/PhysRevLett.95.230405 (cit. on p. 36).

[114] W. Ketterle and M. W. Zwierlein. "Making, probing and understanding ultracold fermi gases". In: *Proc. of the International School of Physics 'Enrico Fermi'* CLXIV (2008). DOI: 10.1393/ncr/i2008-10033-1 (cit. on p. 36).

[115] Thomas Lompe. "An apparatus for the production of molecular Bose-Einstein condensates". Diploma's thesis. Universität Heidelberg, 2008 (cit. on p. 37).

[116] P. M. Duarte et al. "All-optical production of a lithium quantum gas using narrow-line laser cooling". In: *Phys. Rev. A* 84 (6 2011), p. 061406. DOI: 10.1103/PhysRevA.84.061406 (cit. on p. 39).

[117] Eleonora Lippi. "Realization of a large-spacing optical lattice for trapping fermionic lithium gases in two dimensions". Master's thesis. Universita degli studi Firenze, 2017 (cit. on p. 40).

[118] Matthias Neidig. "A realization of a two-dimensional Fermi gas in a standingwave trap". Master's thesis. Universität Heidelberg, 2013 (cit. on pp. 44, 51).

[119] Christof Weitenberg. "Single-Atom Resolved Imaging and Manipulation in an Atomic Mott Insulator". PhD thesis. LMU München, 2011 (cit. on pp. 47, 58).

[120] C. Becker et al. "Ultracold quantum gases in triangular optical lattices". In: *New Journal of Physics* 12.6 (2010), p. 065025. DOI: 10.1088/1367-2630/12/6/065025 (cit. on p. 47).

[121] J. Struck et al. "Quantum Simulation of Frustrated Classical Magnetism in Triangular Optical Lattices". In: *Science* 333.6045 (2011), pp. 996–999. DOI: 10.1126/science.1207239 (cit. on p. 47).

[122] J. Struck et al. "Engineering Ising-XY spin-models in a triangular lattice using tunable artificial gauge fields". In: *Nature Physics* 9.11 (2013), pp. 738–743. DOI: 10.1038/nphys2750 (cit. on p. 47).

[123] D. Greif et al. "Short-Range Quantum Magnetism of Ultracold Fermions in an Optical Lattice". In: *Science* 340.6138 (2013), pp. 1307–1310. DOI: 10.1126/science.1236362 (cit. on p. 47).

[124] J. Struck et al. "Tunable Gauge Potential for Neutral and Spinless Particles in Driven Optical Lattices". In: *Phys. Rev. Lett.* 108 (22 2012), p. 225304. DOI: 10.1103/PhysRevLett.108.225304 (cit. on p. 47).

[125] K. Jiménez-García et al. "Peierls Substitution in an Engineered Lattice Potential". In: *Phys. Rev. Lett.* 108 (22 2012), p. 225303. DOI: 10.1103/PhysRevLett.108.225303 (cit. on p. 47).

[126] P. Soltan-Panahi et al. "Multi-component quantum gases in spin-dependent hexagonal lattices". In: *Nature Physics* 7.5 (2011), pp. 434–440. DOI: 10.1038/nphys1916 (cit. on p. 47).

[127] M. Weinberg et al. "Breaking inversion symmetry in a state-dependent honeycomb lattice: artificial graphene with tunable band gap". In: *2D Materials* 3.2 (2016), p. 024005. DOI: 10.1088/2053-1583/3/2/024005 (cit. on p. 47).

[128] Gregor Jotzu et al. "Experimental realization of the topological Haldane model with ultracold fermions". In: *Nature* 515.7526 (2014), pp. 237–240. DOI: 10.1038/nature13915 (cit. on pp. 47, 48).

[129] N. Fläschner et al. "Experimental reconstruction of the Berry curvature in a Floquet Bloch band". In: *Science* 352.6289 (2016), pp. 1091–1094. DOI: 10.1126/science.aad4568 (cit. on pp. 47, 48).

[130] Thomas Uehlinger et al. "Artificial Graphene with Tunable Interactions". In: *Physical Review Letters* 111.18 (2013). DOI: 10.1103/physrevlett.111.185307 (cit. on p. 48).

[131] Nick Fläschner et al. "High-precision multiband spectroscopy of ultracold fermions in a nonseparable optical lattice". In: *Phys. Rev. A* 97 (5 2018), p. 051601. DOI: 10.1103/PhysRevA.97.051601 (cit. on p. 48).

[132] L. Duca et al. "An Aharonov-Bohm interferometer for determining Bloch band topology". In: *Science* 347.6219 (2014), pp. 288–292. DOI: 10.1126/science.1259052 (cit. on p. 48).

[133] Michael Messer et al. "Exploring Competing Density Order in the Ionic Hubbard Model with Ultracold Fermions". In: *Physical Review Letters* 115.11 (2015). DOI: 10.1103/physrevlett.115.115303 (cit. on p. 48).

[134] N. Goldman et al. "Creating topological interfaces and detecting chiral edge modes in a two-dimensional optical lattice". In: *Physical Review A* 94.4 (2016). DOI: 10.1103/physreva.94.043611 (cit. on p. 48).

[135] Rémi Desbuquois et al. "Controlling the Floquet state population and observing micromotion in a periodically driven two-body quantum system". In: *Physical Review A* 96.5 (2017). DOI: 10.1103/physreva.96.053602 (cit. on p. 48).

[136] Frederik Görg et al. "Enhancement and sign change of magnetic correlations in a driven quantum many-body system". In: *Nature* 553.7689 (2018), pp. 481–485. DOI: 10.1038/nature25135 (cit. on p. 48).

[137] N. Fläschner et al. "Observation of dynamical vortices after quenches in a system with topology". In: *Nature Physics* 14.3 (2017), pp. 265–268. DOI: 10.1038/s41567-017-0013-8 (cit. on p. 48).

[138] Matthias Tarnowski et al. "Observation of Topological Bloch-State Defects and Their Merging Transition". In: *Physical Review Letters* 118.24 (2017). DOI: 10.1103/physrevlett.118.240403 (cit. on p. 48).

[139] Matthias Tarnowski et al. "Measuring topology from dynamics by obtaining the Chern number from a linking number". In: *Nature Communications* 10.1 (2019). DOI: 10.1038/s41467-019-09668-y (cit. on p. 48).

[140] Luca Asteria et al. "Measuring quantized circular dichroism in ultracold topological matter". In: *Nature Physics* 15.5 (2019), pp. 449–454. DOI: 10.1038/s41567-019-0417-8 (cit. on p. 48).

[141] A. Eckardt et al. "Frustrated quantum antiferromagnetism with ultracold bosons in a triangular lattice". In: *EPL (Europhysics Letters)* 89.1 (2010), p. 10010. DOI: 10.1209/0295-5075/89/10010 (cit. on p. 48).

[142] Timon Alexander Hilker. "Spin-Resolved Microscopy of Strongly Correlated Fermionic Many-Body States". PhD thesis. LMU München, 2017 (cit. on p. 48).

[143] Julian Struck. "Artificial Gauge Fields in Driven Optical Lattices". PhD thesis. Universität Hamburg, 2013 (cit. on pp. 48, 51).

[144] Toru Yoshizawa. *Handbook of Optical Metrology - Principles and Applications, Second Edition*. Revised. Justus-Liebig-Universität Gießen: Taylor & Francis, 2015. ISBN: 978-1-466-57359-8 (cit. on p. 49).

[145] S. Altshuler, L. M. Frantz, and R. Braunstein. "Reflection of Atoms from Standing Light Waves". In: *Phys. Rev. Lett.* 17 (5 1966), pp. 231–232. DOI: 10.1103/PhysRevLett.17.231 (cit. on p. 51).

[146] Bryce Gadway et al. "Analysis of Kapitza-Dirac diffraction patterns beyond the Raman-Nath regime". In: *Opt. Express* 17.21 (2009), pp. 19173–19180. DOI: 10.1364/OE.17.019173 (cit. on p. 51).

[147] Nick Fläschner. "Ultracold Fermions in Tunable Hexagonal Lattices: From High-Precision Spectroscopy to the Measurement of Berry Curvature". PhD thesis. Universität Hamburg, 2016 (cit. on p. 51).

[148] Klaus Hueck. "Erzeugung und Untersuchung von ultrakalten, zweidimensionalen Fermi-Gasen". Master's thesis. Universität Hamburg, 2013 (cit. on p. 51).

[149] Martin Boll. "Spin and Density Resolved Microscopy of Hubbard Chains". PhD thesis. LMU München, 2016 (cit. on p. 55).

[150] S. Blatt et al. "Low-noise optical lattices for ultracold ^{6}Li". In: *Phys. Rev. A* 92 (2 2015), p. 021402. DOI: 10.1103/PhysRevA.92.021402 (cit. on p. 55).

[151] A. Mazurenko et al. "Implementation of a stable, high-power optical lattice for quantum gas microscopy". In: *Review of Scientific Instruments* 90.3 (2019), p. 033101. DOI: 10.1063/1.5066623 (cit. on p. 55).

[152] Tobias Petersen. "Charakterisierung eines hochauflösenden Abbildungssystems". Bachelor's thesis. Universität Hamburg, 2018 (cit. on pp. 58, 60, 62).

[153] Eugene Hecht. *Optik*. Germany: Oldenbourg, 2009. ISBN: 978-3-486-58861-3 (cit. on p. 58).

[154] Klaus Hueck et al. "Calibrating high intensity absorption imaging of ultracold atoms". In: *Optics Express* 25.8 (2017), p. 8670. DOI: 10.1364/oe.25.008670 (cit. on pp. 63, 72).

[155] G. Reinaudi et al. "Strong saturation absorption imaging of dense clouds of ultracold atoms". In: *Optics Letters* 32.21 (2007), p. 3143. DOI: 10.1364/ol.32.003143 (cit. on p. 63).

[156] Martin Gerhard Ries. "A Two-Dimensional Fermi Gas in the BEC-BCS Crossover". PhD thesis. Universität Heidelberg, 2015 (cit. on p. 63).

[157] Michael Eric Gehm. "Preparation of an optically-trapped Degenerate Fermi Gas of ^{6}Li: Finding the route to degeneracy". PhD thesis. Duke University, 2003 (cit. on pp. 64, 86–88).

[158] Andrea Bergschneider. "Strong correlations in few-fermion systems". PhD thesis. Universität Heidelberg, 2017 (cit. on pp. 64, 71).

[159] Zoran Hadzibabic. "Studies of a Quantum Degenerate Fermionic Lithium Gas". PhD thesis. Massachusetts Institute of Technology, 2003 (cit. on p. 64).

[160] J. Appel, A. MacRae, and A. I. Lvovsky. "A versatile digital GHz phase lock for external cavity diode lasers". In: *Measurement Science and Technology* 20.5 (2009), p. 055302. DOI: 10.1088/0957-0233/20/5/055302 (cit. on p. 65).

[161] Jan Mika Jacobsen. "A Reconstruction Algorithm for Fluorescence Images of Lithium Atoms in a Triangular Optical Lattice". Masters's thesis. Universität Hamburg, 2017 (cit. on p. 70).

[162] Lewis R. B. Picard et al. *Deep Learning-Assisted Classification of Site-Resolved Quantum Gas Microscope Images*. 2019. eprint: arXiv:1904.08074 (cit. on p. 71).

[163] Sven Krönke et al. "Quantum point spread function for imaging trapped few-body systems with a quantum gas microscope". In: (2018). DOI: 10.1088/1367-2630/ab1ae7 (cit. on p. 71).

[164] Dirk-Sören Lühmann, Christof Weitenberg, and Klaus Sengstock. "Emulating Molecular Orbitals and Electronic Dynamics with Ultracold Atoms". In: *Physical Review X* 5.3 (2015). DOI: 10.1103/physrevx.5.031016 (cit. on pp. 71, 73).

[165] Justus Christopher Brüggenjürgen. "Maßgeschneiderte optische Fallen mit Hilfe örtlicher Lichtmodulatoren". Bachelor's thesis. Universität Hamburg, 2017 (cit. on pp. 71, 72).

[166] Philip Zupancic et al. "Ultra-precise holographic beam shaping for microscopic quantum control". In: *Optics Express* 24.13 (2016), p. 13881. DOI: 10.1364/oe.24.013881 (cit. on p. 72).

[167] Katinka Horn. "Örtlicher Lichtmodulatoren zum Einsatz in Quantengasexperimenten". Bachelor's thesis. Universität Hamburg, 2018 (cit. on p. 72).

[168] Ferenc Krausz and Misha Ivanov. "Attosecond physics". In: *Reviews of Modern Physics* 81.1 (2009), pp. 163–234. DOI: 10.1103/revmodphys.81.163 (cit. on p. 73).

[169] Ruwan Senaratne et al. "Quantum simulation of ultrafast dynamics using trapped ultracold atoms". In: *Nature Communications* 9.1 (2018). DOI: 10.1038/s41467-018-04556-3 (cit. on p. 73).

[170] P. B. Corkum. "Plasma perspective on strong field multiphoton ionization". In: *Physical Review Letters* 71.13 (1993), pp. 1994–1997. DOI: 10.1103/physrevlett.71.1994 (cit. on p. 74).

[171] M. Yu. Kuchiev. "Atomic antenna". In: *Soviet Journal of Experimental and Theoretical Physics Letters* 45 (1987), p. 404 (cit. on p. 74).

[172] Jan L. Chaloupka and Daniel D. Hickstein. "Dynamics of Strong-Field Double Ionization in Two-Color Counterrotating Fields". In: *Physical Review Letters* 116.14 (2016). DOI: 10.1103/physrevlett.116.143005 (cit. on p. 74).

[173] J. M. Leinaas and J. Myrheim. "On the theory of identical particles". In: *Il Nuovo Cimento B Series 11* 37.1 (1977), pp. 1–23. DOI: 10.1007/bf02727953 (cit. on p. 75).

[174] Frank Wilczek. "Magnetic Flux, Angular Momentum, and Statistics". In: *Physical Review Letters* 48.17 (1982), pp. 1144–1146. DOI: 10.1103/physrevlett.48.1144 (cit. on p. 75).

[175] Ady Stern. "Anyons and the quantum Hall effect—A pedagogical review". In: *Annals of Physics* 323.1 (2008), pp. 204–249. DOI: 10.1016/j.aop.2007.10.008 (cit. on p. 75).

[176] N.R. Cooper. "Rapidly rotating atomic gases". In: *Advances in Physics* 57.6 (2008), pp. 539–616. DOI: 10.1080/00018730802564122 (cit. on p. 75).

[177] M. R. Matthews et al. "Vortices in a Bose-Einstein Condensate". In: *Physical Review Letters* 83.13 (1999), pp. 2498–2501. DOI: 10.1103/physrevlett.83.2498 (cit. on p. 75).

[178] K. W. Madison et al. "Vortex Formation in a Stirred Bose-Einstein Condensate". In: *Physical Review Letters* 84.5 (2000), pp. 806–809. DOI: 10.1103/physrevlett.84.806 (cit. on p. 75).

[179] J. R. Abo-Shaeer et al. "Observation of Vortex Lattices in Bose-Einstein Condensates". In: *Science* 292.5516 (2001), pp. 476–479. DOI: 10.1126/science.1060182 (cit. on p. 75).

[180] M W Zwierlein et al. "Vortices and superfluidity in a strongly interacting Fermi gas". In: *Nature* 435 (2005), pp. 1047–1051. published (cit. on p. 75).

[181] H. Saarikoski et al. "Vortices in quantum droplets: Analogies between boson and fermion systems". In: *Reviews of Modern Physics* 82.3 (2010), pp. 2785–2834. DOI: 10.1103/revmodphys.82.2785 (cit. on p. 75).

[182] Ana Lopez and Eduardo Fradkin. "Fractional quantum Hall effect and Chern-Simons gauge theories". In: *Physical Review B* 44.10 (1991), pp. 5246–5262. DOI: 10.1103/physrevb.44.5246 (cit. on p. 75).

[183] Nathan Gemelke, Edina Sarajlic, and Steven Chu. *Rotating Few-body Atomic Systems in the Fractional Quantum Hall Regime*. 2010. eprint: arXiv:1007.2677 (cit. on p. 75).

[184] N. Barberán et al. "Ordered structures in rotating ultracold Bose gases". In: *Physical Review A* 73.6 (2006). DOI: 10.1103/physreva.73.063623 (cit. on p. 75).

[185] Dominik Vogel. "Measuring Geometry and Topology of Floquet-Bloch States in and out of Equilibrium with ultracold Fermions". PhD thesis. Universität Hamburg, 2018 (cit. on pp. 77, 80).

[186] *MT-085: Fundamentals of Direct Digital Synthesis*. One Technology Way P. O. Box 9106 Norwood, MA 02062-9106: Analog Devices, 2009 (cit. on p. 77).

[187] Walt Kester. *Analog-Digital Conversion*. Analog Devices, 2004. ISBN: 0916550273 (cit. on p. 77).

[188] R. Duncan. "FORTH 8086 Assembler". In: *Dr. Dobb's Journal of Software Tools* 7.2 (1982) (cit. on p. 80).

[189] Bushra Soltani Farani. *Double-Buffering Program and Amplitude/Frequency/Phase Lock-Loop*. Tech. rep. Universität Hamburg, 2018 (cit. on p. 81).

[190] Alan V. Oppenheim, Alan S. Willsky, and S. Hamid. *Signals and Systems (2nd Edition)*. Pearson, 1996. ISBN: 0138147574 (cit. on p. 81).

[191] E. L. Hazlett et al. "Realization of a Resonant Fermi Gas with a Large Effective Range". In: *Physical Review Letters* 108.4 (2012). DOI: 10.1103/physrevlett.108.045304 (cit. on p. 89).

[192] G. Zürn et al. "Precise Characterization ofLi6Feshbach Resonances Using Trap-Sideband-Resolved RF Spectroscopy of Weakly Bound Molecules". In: *Physical Review Letters* 110.13 (2013). DOI: 10.1103/physrevlett.110.135301 (cit. on p. 89).

Danksagung

Zuallererst möchte ich an dieser Stelle meinen Doktorvater Klaus Sengstock nennen. Vielen Dank für anregende Diskussionen, wichtige Ratschläge und dein großes Vertrauen in mich und meine Arbeit. Ebenso möchte ich mich bei Henning Moritz bedanken, der die Zweitbegutachtung dieser Arbeit übernommen hat.
Ferner möchte ich Christof Weitenberg, dem PI und Post-Doc des Lithium-Teams für sein unermüdliches Engagement danken und dass ihn jederzeit überall auf der Welt meine Sorgen erreicht haben.
Auch Benno Rem, der lange als Post-Doc an unserem Experiment tätig war, möchte ich an dieser Stelle danken. Deine Euphorie und Motivation waren mir stets ein passender Begleiter.
Ein besonderer Dank gilt an dieser Stelle selbstverständlich meinem Mitdoktoranden Michael Hagemann, der mich mit Einsatz unterstützt und mir darüber hinaus einiges an organisatorischer Arbeit abgenommen hat. Du bist mir auch neben der Arbeit ein Freund geworden, auf den ich mich verlassen kann.
Danken möchte ich außerdem unserem Junior-Doktoranden und früheren Masterstudenten Mathis Fischer für seine Beiträge zum Gelingen dieser Arbeit, sowie einer freudigen Zahl an Studenten, die mir mit ihren Abschlussarbeiten oder HiWi-Tätigkeiten helfend zur Seite standen. Dazu gehören Jan Mika Jacobsen, Niels Rohweder, Cora Braun, Tobias Petersen, Bojan Hansen, Yann Kiefer, Justus Brüggenjürgen, Katinka Horn, Malte Hagemann, Jonathan Schwardt, Vivien Sleziona, Corinna Menz, Nora Bidzinski, Silvan Heinrich und Niklas Käming.
Furthermore, I would like to thank our internship student Jinggang Xiang who I supervised with his work on building an iodine spectroscopy at 671 nm. It was a pleasure to work with you and thank you again for organizing a lab tour for me at MIT on week-end!
Herzlichst bedanken möchte ich mich auch bei allen anderen Teams unserer Forschungsgruppe, dem BFM-Team, dem Spinor-Team, dem Yb-Team, dem Femto-Team, dem Nano-Team und im ganz speziellen bei Ortwin Hellmig, der mit viel Sachverstand, Engagement und Kreativität seinen Anteil am Gelingen dieser Arbeit hat.
An dieser Stelle möchte ich ebenfalls das Personal für Technik und Verwaltung der Universität erwähnen. Im speziellen natürlich diejenigen Mitarbeiter vor Ort am Institut und in der Werkstatt. Vielen Dank für die tatkräftige Unterstützung!
Ganz persönlich möchte ich meiner Familie und meinen Freunden für ihr Interesse aber auch für viel Ablenkung danken, und natürlich ganz besonders meiner Ehefrau und langjährigen Freundin Abhilasha: Ich danke dir für ganz viel Rücksicht, Ermutigung und Liebe, die du mir in den letzten Jahren entgegengebracht hast!

Eidesstattliche Erklärung

Hiermit versichere ich an Eides statt, die vorliegende Dissertationsschrift selbst verfasst und keine anderen als die angegebenen Hilfsmittel und Quellen benutzt zu haben. Die eingereichte schriftliche Fassung entspricht der auf dem elektronischen Speichermedium. Die Dissertation wurde in der vorgelegten oder einer ähnlichen Form nicht schon einmal in einem früheren Promotionsverfahren angenommen oder als ungenügend beurteilt. Es sind keine Vorveröffentlichungen aus dieser Dissertation hervorgegangen.

Unterschrift: _____

Datum: _____